Weak Lensing Techniques on the Curved Sky

Zoe M. Vallis

Supervisors: Prof Tom Kitching, Dr Jason McEwen, Prof Mark Cropper

A dissertation submitted in partial fulfillment

of the requirements for the degree of

Doctor of Philosophy

of

University College London.

Mullard Space Science Laboratory

University College London

October 3, 2019

I, Zoe M. Vallis, confirm that the work presented in this thesis is my own. Where information has been derived from other sources, I confirm that this has been indicated in the work.

Abstract

Future weak lensing surveys will cover larger areas of the sky that necessitate analysis on the curved sky geometry instead of projections to the plane. This thesis focuses on reconstructing convergence maps from cosmic shear on the curved sky geometry. These convergence maps are useful tools for cosmological analysis, including probing non-Gaussian properties. The first chapter focuses on evaluating the performance of different methods of projecting simulated shear data from the curved sky to the plane, to subsequently undergo Kaiser-Squires reconstruction and analysis, and drawing comparisons to reconstruction and analysis directly on the sphere, using peak counts and Minkowski Functionals as the statistics selected for comparison. It is found that projections to the plane are only effective for small areas and it is preferable to perform analysis directly on the sphere when possible. Under ideal circumstances, peak counts derived from data projected using the sine and orthographic projections are most accurate to the spherical case. For the Minkowski Functionals there are significant differences that persist even when attempting to mitigate the projection effects. While certain projections allow reasonable approximations of the spherical sky geometry, it is impractical to use such projections on data covering large areas of the sky and performing analysis on the spherical setting is preferable. The second and third chapters focus on the separation of E-modes and B-modes through wavelet pure mode estimators on the sphere, which cancel mode mixing caused by masking of the shear data. The aim is to remove ambiguous

modes to produce pure E-B modes, providing greater accuracy for studying cosmology from them. An evaluation of the accuracy of this method is performed using simulated data to compare the Kaiser-Squires, harmonic pure estimator and wavelet pure estimator methods. This finds a significant improvement in the accuracy of recovering simulated E-modes and B-modes when using the wavelet pure estimator, over the Kaiser-Squires method and harmonic pure estimator. This wavelet pure estimator method is applied to DES Y1 data and statistics, including the Minkowski Functionals, are derived and discussed. The wavelet pure estimator successfully reconstructs the E-mode and B-mode maps accurate to previous studies of the data. The Minkowski Functionals of the E-modes and B-modes display distinct differences to the analytic form for a 2D Gaussian random field. A new problem is discovered in the apodisation of the data near the mask boundary, and a potential solution is attempted through identifying and removing apodised pixels with a new mask.

Impact Statement

The primary impact of the research performed in this thesis is the potential improvements over previous techniques in the field of cosmological analysis, which will be useful in the field of cosmology. The two main focuses of this thesis are the reconstruction on the sphere and comparison of this to commonly used reconstruction on the projected plane, and the wavelet pure mode estimator as an extension of existing pure mode estimator methods.

The importance of performing analysis on the sphere is stressed due to future surveys covering significantly large areas of the sky such that flat sky approximations and projections are no longer accurate. This is demonstrated through comparison of selected statistics (the peak statistic and Minkowski Functionals) on five projected cases and on the spherical case, hence this research also serves as an illustration on how these statistics are affected by these different methods of projection from the sphere to the plane in comparison to the spherical case. The technique of E-B mode separation will be useful for creating cleaner mass maps and therefore more accurate cosmological results derived from them.

These techniques are discussed as applied to cosmic shear, but are applicable to other sources of cosmological data, such as the cosmic microwave background, on the curved sky geometry. The thesis discusses the challenges involved in analysing the spin-2 shear fields, such as projection from the sphere to the plane, which could

potentially be extended to work with spin fields in contexts other than cosmology. This research is significant in the context future astronomical surveys (eg Euclid, LSST) that have significant sky coverage and seek to probe dark energy through weak lensing, hence it is desirable to have highly accurate results free from contamination such as E-B mode mixing. Discoveries made about performing analysis in the curved sky setting compared to projected data may prove useful for fields outside astronomy that are also concerned with the geometry of the data, such as medical imaging or geography. In addition, improving techniques for creating mass maps are useful for creating better mass maps for outreach and raising public understanding about cosmological research and the purpose of these surveys.

Acknowledgements

I would like to thank my supervisors, Tom Kitching, Jason McEwen and Mark Cropper, for their guidance and encouragement during my PhD. I am incredibly grateful to have had such supportive and approachable supervisors who were always ready to answer any questions and provide advice.

I am grafetul to Chris Wallis and Boris Leistedt for discussion and help with various code used, Paniez Paykari and Peter Taylor for allowing me to use their data for my work on this thesis, and Daisuke Kawata for support and advice with the process of undertaking a PhD.

I would also like to thank to everyone in the MSSL astronomy group, who made me feel welcomed and supported during my time there. I will always have fond memories of MSSL and the people there. Additionally, I thank Georgina Graham, Denis Gonzales and Monica Tress for being friendly and reliable housemates during my time in Guildford.

Special thanks to my family for their continued support and encouragement throughout my life and during my PhD.

Finally, I thank Robin Thomas his endless patience and support throughout everything and being a constant source of inspiration.

Contents

List of Figures

Introduction

The study of cosmology seeks to understand the universe on the largest scales, including its origin, evolution, its physical properties on scales significantly greater than the galactic scale, and the structures that have emerged as a result of these properties and its evolution. This thesis focuses on techniques and analysis methods used for probing dark energy and other cosmological parameters through studying cosmic shear, the gravitational lensing signal caused by the Large-Scale Structure (LSS), specifically with regards to the curved sky geometry and the problem of E-B mode separation. The LSS describes the structure of matter in the universe on the largest observable scales, where its growth has been influenced by the expansion of the universe and the effect of dark energy, as it originated from small perturbations in the early universe. On scales of more than 10 Mpc, the universe is inhomogeneous and made up of superclusters, walls and filaments, as well as voids of low matter density separating them. The evolution of the LSS over time is influenced by various cosmological parameters, so studying cosmic shear, and by extension the LSS, is a useful way to probe the cosmology of the universe.

Weak lensing and cosmology

The properties and evolution of the universe leave their influence on various observables, with different observables being more sensitive to different cosmological parameters. Among the avenues for cosmological research are observations of

the Cosmic Microwave Background (CMB), the use of supernovae as cosmological probes, redshift surveys to map the large-scale distribution of matter, detection of gravitational waves, and gravitational lensing. This thesis focuses specifically on weak lensing, a specific type of gravitational lensing that is analysed in the form of a weak statistical signal, and is a rapidly growing field of research with upcoming surveys (such as Euclid [Laureijs et al., 2011] and the LSST [LSST Science Collaboration et al., 2009]) promising a wealth of new data in the coming years.

Gravitational lensing is a lensing effect bending the trajectory of light rays induced by variations in the gravitational field caused by the presence of matter. Due to the weakness of the gravitational force, only on the largest scales with significant masses does this effect become observable. The observed distortion effects are categorised into strong lensing, displaying noticeable shape distortion such as the light source becoming an arc, and weak lensing, displaying very slight shape distortions such that studying it requires analysis of a large number of light sources on a statistical scale.

Weak lensing provides a useful tool for tracing distributions of matter in the universe, including dark matter which cannot be observed through direct detection of electromagnetic waves. In order to accurately study the large-scale distribution of matter in the universe and its evolution, it is necessary to account for dark matter, which comprises the majority of matter in the universe. Among the many methods of indirect observation of dark matter, weak lensing proves extremely useful for studying dark matter on the largest scales.

Information from weak lensing

Cosmic shear is the weak lensing signal caused by light propagating through the LSS of the universe and is sensitive to various parameters that govern the evolution of the universe. Statistics can be derived from the cosmic shear and compared with those derived from models of the universe to constrain cosmological parameters, and to provide measurements of the errors on these constraints. The primary parameters (see Section 1.1.14) constrained by weak lensing are σ_8, which defines the amplitude of the matter power spectrum on 8Mpc scales, and Ω_M, the present-day value of the dimensionless matter over-density parameter. Dark energy influences the growth

of structure in the universe, and as such cosmic shear can be used to probe the nature of dark energy [Heavens et al., 2006]. Dark energy is defined by its equation of state, given as $w(z) = \frac{\rho}{p}$ where ρ is the energy density, p is the vacuum pressure and the dimensionless factor $w(z)$ is a function of redshift, and by extension, time. By constraining this parameter, it will be possible to distinguish between various models for dark energy, such as whether dark energy is the cosmological constant or an effect of a modified theory of gravity [Amendola et al., 2013]. Overall models of the universe include these specific models for dark energy, so probing the dark energy equation of state parameter w, along with other cosmological parameters, allows us to examine which model most closely matches observations and therefore is mostly likely to describe the universe.

One major focus of cosmology is to construct and evaluate a model to describe the universe, including cosmological parameters of the model, using observations to evaluate the validity of each potential model and to increase precision on values for the cosmological parameters. This is achieved through a variety of methods observing different astronomical objects or physical effects that are significantly influenced by the cosmological properties and evolution of the universe.

Simulations play a significant role in cosmology, as it is not possible to obtain data on other potential iterations of the universe through observation. Instead, data from simulations generated through a model and specific parameters are tested against data from observations, evaluating the likelihood that the model is a fitting description of the data.

One frequent use of weak lensing data for probing cosmology is the derivation of various statistical measures, such as the commonly-used power spectrum (see Section 1.3.2), and comparing them to the statistics calculated from simulations of the equivalent weak lensing field. Other such statistics include the peak count statistic (see Section 1.3.4) and Minkowski Functionals (see Section 1.3.5), which are used in this thesis.

Challenges in weak lensing analysis

The field of weak lensing analysis requires high precision to compensate for the inherent weakness of the weak lensing signal, and involves many observational

considerations that influence results. Straightfoward ones such as smearing from the point-spread function (PSF) can be dealt with through calibration, while effects such as data masking from incomplete data provide more complicated challenges to deal with. One of the effects of masking is mode-mixing that results in inaccuracies in E-modes and B-modes (see Section 1.2.6) recovered from the shear data. An approach to solve this issue is to use pure mode estimators, which, combined with wavelets, is the focus of chapter 3 and chapter 4.

Most current studies of cosmic shear are limited to small areas of a few hundred square degrees (154 deg^2 for CFHTLenS [Erben et al., 2013a]), but more recent surveys will extend this to significantly larger areas, such as Euclid's planned 15,000 deg^2 survey [Amendola et al., 2013] and the currently underway Dark Energy Survey (DES) with sky coverage of 5000 deg^2 [Abbott et al., 2005]. Ground-based telescopes such as the Large Synoptic Survey Telescope (LSST) [Abate et al., 2012] have increasingly wide fields of view, 9.6 deg^2 in the case of the LSST. These surveys will gather high quality image data with wider wavelength coverage to allow for more precise galaxy redshift measurements and will be able to measure to higher redshifts than previously possible. Existing surveys such as the 1,500 deg^2 Kilo-Degree Survey (KiDS) [de Jong et al., 2013] also provide a significant amount of data useful for cosmic shear studies. These surveys are designed to gather data suitable for weak lensing analysis of dark energy as either their primary goal (DES, Euclid) or as part of a number of their scientific goals (KiDS, LSST), and will produce larger amounts of high quality data than previous surveys. This makes the development of weak lensing analysis new techniques an important focus for the cosmological research in the coming years. The current analysis methods used make several assumptions that will not be valid for larger scales, necessitating the development of new methods to fully account for the geometry of the environment the data exists in, which is why we opt to perform reconstruction and analysis on the sphere over flat sky approximations or projections to the plane.

Research goals

The two challenges to weak lensing analysis that are the primary focus of this thesis are the issue of accommodating the curved sky geometry for greater sky

coverage, and mode-mixing resulting from masked data. We seek to take methods used to reconstruct the convergence map on the curved sky and compare them with reconstruction performed on the plane, after the weak lensing data is subject to projection from the spherical setting to the plane. This project focuses on the peak count statistic and Minkowsi Functionals as statistics to evaluate the performance of each method, as these two statistics rely upon the morphology of the data map and hence are susceptible to influence by geometry used in reconstruction. This also serves a secondary purpose of evaluating under which conditions projecting the data to the plane is appropriate and at which point it becomes preferable to work in the curved sky setting.

The mode-mixing problem is tackled through using wavelet pure mode estimators to perform E-B separation, with the aim of evaluating whether this method shows an improvement in accuracy of reconstructions. To test this, simulated convergence maps are created and compared with their reconstructions using different methods. We also apply this wavelet pure estimator E-B separation to the DES Y1 data in order to demonstrate the value of this method for use on real data.

Thesis Outline

In order to fully explain the research done in this thesis, Chapter 1 will summarise the relevant cosmological background. This will cover the terminology, notation and cosmological concepts and statistical methods that will be used. Relevant details on the notation and mathematics that are not covered in this chapter will instead be in the Appendix. Other relevant concepts such as wavelets will also be introduced here.

Chapter 2 will detail the research performed on the subject 'Investigating the effect of projections on the peak count and Minkowsi Functionals of convergence maps', using simulated data as the shear from which the convergence maps are reconstructed. This research has been published as a paper under the same title. The cosmic shear data is observed on the spherical surface and is typically projected onto the 2D plane, with methods of mapping the geometry from the spherical surface to the plane. After the projection, the planar shear map is used to reconstruct a convergence map tracing the mass distribution in the observed sky. It is expected that this

mapping of the data to the plane will have a noticeable impact on statistics derived from the topology of the data map, with the projection effects persisting through the reconstruction process. The peak count statistic and Minkowsi Functionals (MFs), described in this chapter, are selected due to their sensitivity to non-Gaussianities in the convergence map and because they are expected to be influenced by projection. This research finds that when examining the peak count statistic and the MFs, projections approximating the spherical sky case hold only under certain small-area circumstances and it is preferable to perform such analysis on the full sky instead. Of these the examined projections sine and orthographic projections best approximate the curved sky for examining the peak count statistic.

Chapter 3 will discuss the separation of E-modes and B-modes from shear data, and how ambiguous modes introduced by data masking present a problem. We detail how wavelets can be used in the wavelet pure mode estimator to cancel ambiguous modes and apply this to simulated weak lensing data. The E-modes and B-modes are also recovered using the Kaiser-Squires pseudo estimator and the harmonic pure estimator for the purpose of comparison. As with chapter 2, this analysis is performed on the curved sky geometry. It is found that the wavelet pure estimator shows a significant improvement when recovering simulated E-modes and B-modes, compared to the Kaiser-Squires and harmonic pure estimator methods. The research and findings of this project have been used to write a paper that is currently under review.

Chapter 4 will cover the third and final section of research, focused on the application of methods used in chapter 3 to DES Year 1 data. We discuss the recovered convergence maps and calculate the Minkowsi Functionals and other statistics from them, and seek to find ways to mitigate the problematic effects that arise when using pure mode estimators. The recovered E-mode and B-mode maps match previous reconstructions, and an apodisation effect is noted. In order to account for the apodisation, a new mask is used that additionally masks the apodised pixels. The MFs of the E-modes and B-modes are compared with the analytic form of the MFs a 2D Gaussian random field and show a distinct difference, even accounting for the apodisation. A paper based on this chapter is currently in prep and is expected to be submitted for review soon.

CHAPTER 1

Background

1.1 Cosmology

This overview of the field of cosmology will first give a qualitative description of the currently held consensus of the cosmology of the Universe, followed by further detail on the mathematics and commonly used formulae and definitions. Where relevant, further detail will be elaborated upon, and in cases where concepts are introduced before explanation, the section of the thesis with the full explanation will be referenced.

1.1.1 The Cosmological Principle

Underpinning the understanding and study of the cosmology of the Universe is the cosmological principle, which states that the Universe is, on the largest scales, isotropic and homogeneous. This principle allows the assumption that the properties of the universe on sufficiently large scales will appear the same to an observer no matter their location. Isotropy states that the universe looks the same regardless of the direction observed, and homogeneity states that the universe will look the same regardless of location observed, in effect stating that the observed universe is invariant under the observer's rotation or translation respectively. The cosmological principle allows the assumption that any understanding of the universe derived from observations on Earth will also hold anywhere else in the universe.

1.1.2 The Standard Model of Cosmology

The standard model of cosmology currently accepted for the universe is the ΛCDM model, positing that the universe is comprised of radiation, non-relativistic matter, which includes baryonic matter, cold dark matter, and dark energy (also referred to as the cosmological constant in particular circumstances, see 1.1.12).

Observable baryonic matter comprises only ∼15% of the total matter content and ∼4% of the total energy content of the universe [Aghanim et al., 2018]. 'Dark matter', comprising ∼ 27% of the energy content of the universe and ∼ 85% of the matter in the universe, is the term used to refer to the portion of matter in the universe that interacts only gravitationally (and possibly via the weak interaction) and does not couple with electromagnetic radiation. In comparison to baryonic matter, which has dimensionless density parameter (see Section 1.1.13) $\Omega_b \sim 0.045$

[Aghanim et al., 2018], this invisible dark matter has the significantly larger density parameter of Ω_{cdm} ~0.259 [Aghanim et al., 2018] and so plays a significant role in the evolution of the universe. Dark matter does interact via gravity, and as such it influences light and baryonic matter gravitationally such as through gravitational lensing, as detailed in Section 1.2. Evidence for dark matter can be found in observations that cannot be explained by only the visible matter in the system, such as observations of galactic velocity dispersion as early as 1933 [Zwicky, 1933], observations of the relationship between galactic mass and radius [Ostriker et al., 1974], studies of the stability of the galactic disk [Ostriker and Peebles, 1973] and studies of rotation curves of galaxies [Persic et al., 1996]. The exact nature of dark matter is not yet known, but several candidates have been proposed, including 'weakly interacting massive particles' (WIMPs) [Roszkowski et al., 2018] and 'massive astrophysical compact halo objects' (MACHOs) [Bennett et al., 1996]. However, recent research casts doubt on the standard WIMP and MACHO models and favours alternatives such as axions [Bergstrom, 2009] and sterile neutrinos [Boyarsky et al., 2019] among others [Bertone and Tait, 2018]. Models of the universe including dark matter also leave an impact on the Large-Scale Structure (LSS) and Cosmic Microwave Background (CMB), which allows comparison between prediction and observation.

The LSS of the universe is comprised of both dark matter and visible matter and is distributed throughout the universe in a web of filaments around which baryonic matter coalesces to form stars and galaxies, and understanding its structure and evolution provides useful insights into the nature of the universe. The term 'cold' is used to indicate that the dark matter possesses relatively low thermal energy and its movement is at velocities far slower than the speed of light, due to greater hypothesised particle mass than alternative 'hot' dark matter candidates. Cold dark matter has density parameter (see Section 1.1.13) $\Omega_{cdm} = \Omega_m - \Omega_b$, where Ω_m is density parameter for the total matter in the universe and Ω_b is the density parameter for the baryonic matter.

The other main component of the ΛCDM model is the inclusion of the 'cosmological constant' Λ as a theory for dark energy (see Section 1.1.12), to explain the accelerating expansion of the universe as found by observations of Type 1a supernovae in 1998 [Perlmutter et al., 1999; Riess et al., 1998]. The ΛCDM model

has significant observational support in its predictions of the CMB fluctuation being confirmed by the CMB anisotropies observed by COBE [Smoot et al., 1992], WMAP [Komatsu et al., 2011] and Planck [Ade et al., 2016a], along with constraints on the cosmological parameters matching predictions from the model [Ade et al., 2016b], leading to ΛCDM to be accepted as the standard model of cosmology.

1.1.3 History of the Universe

Most models of the universe extend the expansion of the universe as observed by cosmological redshift (see Section 1.1.10) to posit that the universe expanded from a singularity, the 'Big Bang'. The ΛCDM model is often extended to include a period of rapid exponential expansion $\sim 10^{-34}$ seconds shortly after the Big Bang called 'inflation' [Baumann, 2011; Tsujikawa, 2003]. Inflation is believed to be responsible for many observed properties of the current universe, including its isotropy and homogeneity. Inflation is also responsible for the observed fluctuations in the CMB temperature map and LSS, as quantum density fluctuations are amplified during inflation to macroscopic scales and then seed subsequent evolution of the universe.

Following this period of inflation comes a period of reheating. The temperature drops due to the expansion during inflation, and after inflation the temperature returns to the temperature it was before inflation. This occurs by the inflaton field's potential energy converting into matter and radiation once inflation has ceased. The high temperatures during this reheating allow baryogenesis as an asymmetry emerges between baryons and antibaryons, which leads to the observed predominance of matter over antimatter in the universe [Canetti et al., 2012].

As the universe further cools, symmetry breaking occurs and the properties of the fundamental particles and forces of the universe come to behave as observed in the present day. With the thermal energy of baryons decreasing to the point where the strong force can predominate, Big Bang nucleosynthesis can now take place as protons and neutrons combine to form light elements, supported by the observation of light elements in abundances predicted by models [Alpher et al., 1948]. Then, the photons and baryons fall out of thermal equilibrium and decouple. Prior to decoupling, the photons and baryons exist as if a high-pressure fluid propagating sound waves as a result of density fluctuations. After decoupling, the photons and

baryons no longer oscillate together and the acoustic waves are 'frozen out' and preserved in the form of 'baryon acoustic oscillations' (BAO) that may be observed in the CMB and LSS. Closely associated with the photon-baryon decoupling is recombination, where the free electrons are captured by the free nuclei to form atoms. Before this recombination, it was not possible for light to propagate beyond short distances due to the scattering from free electrons, and after recombination the universe became transparent to photons, allowing them to propagate and giving rise to the CMB. The period of recombination gives rise to the observed CMB, as temperatures cool sufficiently to allow the universe to become transparent to photons (see Section 1.1.4).

After recombination, the universe became neutral and opaque to short wavelength radiation, hence this period is known as the 'Dark Ages'. During this era, dark matter interacts gravitationally, with overdense regions collapsing to form structure. These regions of high mass density in the form of dark matter filaments attract baryonic matter, leading to the emergence of stars and galaxies, which tend to trace dark matter distributions. The universe begins to undergo reionisation as the first stars emit high-energy radiation, which propagates as short wavelength photons and ionises the intergalactic medium of the neutral universe.

Over time, the universe comes to resemble its state as observed in the present day, with galaxies and galaxy clusters forming and evolving alongside the LSS and the expansion of the universe accelerating as the universe enters the era of dark energy expansion. Prior to the discovery of the acceleration of expansion of the universe, it was believed that, according to Einstein's theory of General Relativity, the universe containing only matter and radiation should eventually stop expanding and collapse in on itself. However, observations in 1998 of Type 1a supernovae found evidence that the rate of expansion of the universe was increasing [Perlmutter et al., 1999; Riess et al., 1998]. This expansion demands the existence of a new quantity in the universe, dubbed 'dark energy', with negative pressure. This dark energy quantity causes the observed acceleration of the rate of expansion and opposes the influence of gravity, explaining why the expansion of the universe does not slow or reverse due to the collective gravitational pull of the matter within the universe. This dark energy governs the acceleration of the rate of expansion of the universe,

and therefore influences the formation of the physical structure of matter and its evolution over time. As with fluctuations in the early universe such as the BAO, the imprint of dark energy should be observable in the modern day structure of matter in the universe and therefore in weak lensing observations such as the cosmic shear.

1.1.4 The Cosmic Microwave Background

While the main focus of this work is on weak lensing, observations of the cosmic microwave background (CMB) share some similarities to weak lensing observables. Many techniques used can be applied to both CMB and weak lensing data, including many used in this thesis, hence a very short summary of the CMB is included for context. The CMB is the earliest observable thermal radiation in the universe, produced during recombination when the universe cooled to the point where the electrons and protons combined to form hydrogen atoms. Before recombination, the universe was opaque to radiation since all electrons existed as free electrons that scattered photons, causing it to be impossible for photons to propagate over long distances. After recombination, the universe became transparent to radiation, allowing radiation to propagate without being scattered. The thermal radiation from this period immediately after recombination is the CMB we observe today. The CMB power spectrum is influenced by the early evolution of the universe and is affected by the same parameters that govern the evolution of the LSS, and provide complementary approaches to cosmological analysis. The CMB temperature map has a spin of 0, while the CMB polarisation map has a spin of 2 and can be decomposed into E and B modes (see Section 1.2.6) much like weak lensing maps. The spin of these fields describes the rotational symmetry of the observed signal, with shear possessing a rotational symmetry of order 2, hence a spin of 2.

1.1.5 The Metric Tensor

The universe can be understood on a fundamental level to be comprised of three spatial dimensions and one temporal dimension. We may represent a spacetime by the notation $x^i = (x^0, x^1, x^2, x^3)$, where x^0 denotes the time component and x^1,x^2,x^3 denote spatial components. A point on this spacetime is an instantaneous event that possesses a distinct position in space (x^1, x^2, x^3) at time x_0, and the distance between two events in this spacetime is an interval with a temporal component.

The metric tensor $g_{\mu\nu}$ describes the properties of the spacetime it is associated with and is used to evaluate the distance between two points in a given space. Using Einstein's summation convention (see Appendix A), we write this as

$$\mathrm{d}s^2 = g_{\mu\nu}\mathrm{d}x^\mu \mathrm{d}x^\nu. \tag{1.1.1}$$

Focusing on the use of the metric tensor in general relativity, we use the metric tensor of the interval ds between two events in spacetime. For the same two events, this interval remains constant and is independent of the coordinate system used, hence the metric tensor is linked to the coordinate system.

As an example, the flat Minkowski space with coordinates $x^i = (t, x, y, z)$ has the Minkowski metric, where c denotes the speed of light,

$$g_{\mu\nu} = \eta_{\mu\nu} = \begin{pmatrix} -c^2 & 0 & 0 & 0 \\ 0 & 1 & 0 & 0 \\ 0 & 0 & 1 & 0 \\ 0 & 0 & 0 & 1 \end{pmatrix}, \tag{1.1.2}$$

which allows for the calculation of the spacetime interval as

$$\mathrm{d}s^2 = -c^2\mathrm{d}t^2 + \mathrm{d}x^2 + \mathrm{d}y^2 + \mathrm{d}z^2. \tag{1.1.3}$$

One can then use the definition of a spacetime interval to define a geodesic. A geodesic is the minimised distance between two points in a given space, such that d$s = 0$ for massless particles. In flat space, this is a straight line. In spacetime, this is the shortest path between two events in a spacetime, such that the interval ds is minimised. Particles unaffected by external forces will travel along a geodesic, hence massless, chargeless photons always travel along geodesics. Curvature of spacetime induced by massive objects changes the geodesics in the local spacetime, giving rise to gravitational lensing, which will be discussed in greater detail in Section 1.2.

1.1.6 The Einstein Field Equation

Empty space is not an empty vacuum, but rather contains energy in the form of matter, radiation and dark energy (see Section 1.1.12). It is the interaction between

spacetime and the energy content of the universe that gives rise to effects such as gravitational lensing.

The stress-energy tensor $T_{\mu\nu}$ conveys the information about the energy present in a given spacetime, including the density and flux of energy, density and flux of momentum, and pressure. Gravitational fields arise from the matter and energy, expressed by this stress-energy tensor, hence massive objects produce a gravitational field. Assuming spacetime behaves as a perfect fluid, the non-diagonal elements of the tensor are zero, leaving only the energy density ρ and pressure P, hence the stress-energy tensor can be written as

$$T_{\mu\nu} = \begin{pmatrix} \rho & 0 & 0 & 0 \\ 0 & P & 0 & 0 \\ 0 & 0 & P & 0 \\ 0 & 0 & 0 & P \end{pmatrix}, \tag{1.1.4}$$

The Einstein Field Equation relates the curvature of spacetime, with metric tensor g_{ab}, to the energy and momentum content in the local volume of this spacetime through their respective tensors, the Einstein tensor G_{ab} and the stress-energy tensor T_{ab}, as such

$$G_{ab} = R_{ab} + \frac{1}{2}Rg_{ab} + \Lambda g_{ab} = \frac{8\pi G}{c^4}T_{ab} \tag{1.1.5}$$

where R_{ab} is the Ricci curvature tensor and R is the curvature tensor, which is the trace of the Ricci curvature tensor. The constants in this equation are Newton's gravitational constant G, the speed of light c in a vacuum and the cosmological constant Λ, which will be elaborated upon in Section 1.1.12. The Einstein tensor G_{ab} describes the curvature of spacetime, while the stress-energy tensor contains the energy density and flux, momentum density and flux, and the pressure. Assuming spacetime to behave like a perfect fluid, the non-diagonal elements of the tensor are zero, leaving only the energy density ρ and pressure P. In this case, the stress-energy tensor can be simplified to $T_{ab} = \text{diag}(\rho, P_x, P_y, P_z)$. Due to the equivalence of energy and mass, when discussing the energy density the matter density is also included.

1.1.7 The Friedmann-Lemaître-Robertson-Walker Metric

The exact solution of the Einstein Field Equations in an isotropic and homogeneous universe is given by the Friedmann-Lemaître-Robertson-Walker (FLRW) metric, shown below for polar coordinates

$$ds^2 = -c^2dt^2 + a(t)^2(d\chi^2 + f_K(\chi)d\Omega^2) \tag{1.1.6}$$

where χ is the radial coordinate, $d\Omega = d\theta^2 + \sin(\theta)d\varphi^2$, k is the curvature parameter of the universe and $a(t)$ is the dimensionless scale factor which will be elaborated upon later. The curvature k determines parameter $f_K(\chi)$ as follows

$$f_K(\chi) = \begin{cases} k^{-\frac{1}{2}}\sin(k^{\frac{1}{2}}\chi) & k > 0 \\ \chi & k = 0 \\ (-k)^{-\frac{1}{2}}\sinh((-k)^{\frac{1}{2}}\chi) & k < 0. \end{cases} \tag{1.1.7}$$

Curvature k also defines the shape of the universe. Positive curvature ($k > 0$) defines the geometry of the universe as closed, negative curvature ($k < 0$) defines the geometry of the universe to be hyperbolic and expanding, and $k = 0$ defines the universe as flat. If we define $\Sigma(\chi) = r$, the metric can be written as

$$ds^2 = -c^2dt^2 + a(t)^2\left(\frac{dr^2}{1-kr^2} + r^2d\Omega^2\right). \tag{1.1.8}$$

1.1.8 The Friedmann Equations

Applying the FLRW metric in Equation 1.1.6 to the Einstein Field Equation in Equation 1.1.5 gives the Friedmann Equations

$$\left(\frac{\dot{a}}{a}\right)^2 = \frac{8\pi\rho}{3} + \Lambda - \frac{k}{a^2} \tag{1.1.9a}$$

$$\frac{\ddot{a}}{a} = -\frac{4\pi}{3}(\rho + 3P) + \frac{\Lambda}{3}, \tag{1.1.9b}$$

where $a = a(t)$ is the scale factor (see Section 1.1.9) and the derivatives with respect to time are denoted as $\dot{a} = \frac{da}{dt}$ and $\ddot{a} = \frac{d^2a}{dt^2}$.

From this, one can insert Eq. 1.1.9a into Eq. 1.1.9b to obtain the continuity equation denoting the conservation of mass and energy as

$$\dot{\rho} + 3\frac{\dot{a}}{a}(\rho + P) = 0, \tag{1.1.10}$$

which can also be stated in the form of the stress-energy tensor as

$$\nabla_\mu T_{\mu\nu} = 0, \tag{1.1.11}$$

where ∇_μ denotes the divergence of the tensor.

There are numerous solutions to the Friedmann Equations depending on the cosmological parameters for the specific hypothetical universe in question. In order to solve the Friedmann Equations, the energy content of the universe can be treated as if an ideal fluid, with equation of state

$$P = w\rho, \tag{1.1.12}$$

where w is referred to as the equation of state parameter. The energy content of the universe can be differentiated by type, such that it is comprised of radiation, with pressure P_r and density ρ_r, and matter, with pressure P_m and density ρ_m. The matter in the universe is made up of non-relativistic particles, which have negligible pressure compared to their density, hence effectively $w_m = 0$ and therefore $P_m = 0$. For ultra-relativistic particles, including radiation, the equation of state parameter is $w_r = \frac{1}{3}$, relating the radiation pressure to the radiation density as $P_r = \frac{1}{3}\rho$. Dark energy can be defined by this equation of state, as described in Section 1.1.12, and is defined to have a negative value for w to explain the accelerating expansion of the universe.

1.1.9 The Scale Factor and Hubble parameter

The scale factor $a(t)$ governs the relative expansion of the universe and describes the proper distance, denoted here as x, through expression

$$x(t) = a(t)x_0, \tag{1.1.13}$$

where x_0 is the proper distance at time t_0. At t_0=0, which is defined as the present time, we define $a_0 = a(t_0) = 1$. The proper distance x is defined as the distance between two positions at a specific time t, which will vary with time due to the expansion of the universe, while the comoving distance (see Section 1.1.11) is constant. From the scale factor, the time-dependent Hubble parameter H can be defined as

$$H = \frac{\dot{a}}{a}. \tag{1.1.14}$$

The Hubble constant H_0 is defined as the Hubble parameter H measured today, when $a = a_0$. The Hubble constant has been measured to be 67.4 ± 0.5 km s^{-1} Mpc^{-1} by the 2018 Planck results [Aghanim et al., 2018]. The dimensionless Hubble parameter h is defined by

$$H_0 = 100\, h \text{ km s}^{-1}\text{Mpc}^{-1}, \tag{1.1.15}$$

and current observations place $h \sim 0.674$ [Aghanim et al., 2018].

1.1.10 Cosmological Redshift

Redshift is the name given to the effect that occurs when radiation increases in wavelength due to the distance between the source and the observer increasing while the light is in transit from the source to the observer. The redshift z can be defined through the relation of the emitted wavelength λ_e and the observed wavelength λ_o, or alternately the corresponding emitted and observed frequencies f_e and f_o respectively, as

$$1 + z = \frac{\lambda_o}{\lambda_e} = \frac{f_e}{f_o} \tag{1.1.16}$$

Cosmological redshift z is caused by the expansion of the universe and is defined as

$$1 + z = \frac{a_0}{a(t)} \tag{1.1.17}$$

where a_0 is the value of the scale factor at the present time and $a(t)$ is the scale factor at the time the radiation was emitted. Since $a_0 = 1$, the relation becomes

$$a(t)^{-1} = 1 + z. \tag{1.1.18}$$

Radiation takes time to travel from its source to an observer, and the further this light has travelled, the longer the time elapsed since it was emitted from its source. While the light is traversing the path from source to observer, the universe is undergoing expansion and so the light is affected by redshift. Hence, even if the light source and observer remain in fixed comoving position relative to each other, there is still a change in the distance between them due to the expansion of the universe. The longer light takes to travel, the greater the degree of this redshift. This means that cosmological redshift can be used as a measure of the distance of an object from the observer, and by proxy as a measure of how long ago the radiation was emitted. Astronomical objects with higher redshift are at further distance from the observer, and consequently being observed at an earlier time. In effect, redshifted light observed in the present day on Earth views the source at a time in the past. Studying various cosmological statistics as a function of redshift can be used to probe the change of the universe's statistics over time. Through sorting the light sources into redshift bins, and therefore by length of time ago the light was emitted, and performing analyses on these redshift bins, it is possible to study the changing properties of the universe over time.

Redshift occurs as both the Doppler effect caused by the expansion of the universe and the Doppler effect of the observer and emitter moving at relativistic speeds or in sufficiently large gravitational fields, so in cases where these effects contribute significantly to an object's redshift, they will need to be considered when evaluating the distance of an object. However, for the purposes of this thesis, we do not evaluate objects subject to redshift effects not caused by the expansion of the universe, hence their inclusion is for completeness only. Unless otherwise specified, the term redshift and the notation z refers to the cosmological redshift caused by the recession velocity of galaxies caused by the expansion of the universe, as opposed to the redshift caused by the peculiar velocities of the observer and emitter.

1.1.11 Distance measures

The Hubble time t_H and Hubble distance D_H are constants defined as

$$t_H = \frac{1}{H_0}, \quad D_H = \frac{c}{H_0}. \tag{1.1.19}$$

The comoving distance of an object r is a measure of distance that accounts for the expansion of the universe and as such is always constant, and can be defined as

$$r = \int_t^{t_0} c \frac{1}{a(t')} \mathrm{d}t', \tag{1.1.20}$$

where t_0 is the present day time and t is the time at which light from the object that is being observed at present day was emitted from the object. The comoving distance along the line-of-sight from the object to the observer can be rewritten to be a function of redshift as

$$r = D_h \int_0^z \frac{1}{E(z)} \mathrm{d}z, \tag{1.1.21}$$

where $E(z)$ is a parameter given by the equation

$$E(z) = \sqrt{\Omega_m (1+z)^3 + \Omega_k (1+z)^2 + \Omega_\Lambda}, \tag{1.1.22}$$

[Peebles, 1993]

where $\Omega_m, \Omega_k and \Omega_\Lambda$ denote the density parameters of the matter content of the universe, of the curvature, and the cosmological constant (see Section 1.1.13).

The angular diameter distance D_A of an object is defined as the ratio of the object's physical size R to its angular size θ viewed by the observer. It can be written as below and related to the comoving distance as

$$D_A = \frac{R}{\theta} = \frac{r}{1+z} \tag{1.1.23}$$

The apparent magnitude of an astronomical object is the relative brightness as viewed by the observer. The absolute magnitude M is a method of quantifying the luminosity of an astronomical object, and is defined as equal to the apparent magnitude of said object viewed as if positioned at 10 parsecs away.

Hence, the luminosity distance D_L of an astronomical object related to the absolute magnitude M and apparent magnitude m of the object through the following equation

$$M = m - 5(\log_{10}(D_L) - 1), \tag{1.1.24}$$

so therefore

$$D_L = 10^{(\frac{(m-M)}{5} - 1)}. \tag{1.1.25}$$

The luminosity distance can also be defined by the bolometric flux F and bolometric luminosity L, where bolometric denotes they are integrated over all frequencies, as

$$D_L = \sqrt{\frac{L}{4\pi F}}. \tag{1.1.26}$$

1.1.12 Dark Energy and the Cosmological Constant

The early universe underwent a period when energy in the form of radiation dominated over other forms of energy, followed by a period of matter-dominance. During this era of matter-dominance, the gravitational pull slowed the rate of expansion of the universe. However, this did not continue until a gravitational collapse, but rather the rate of expansion stopped decelerating and instead began to accelerate against the influence of gravity. In order to explain the acceleration of the rate of expansion of the universe, the existence of a quantity called 'dark energy' was posited.

There are a number of proposed models for dark energy, such as the cosmological constant [Carroll, 2001] in ΛCDM cosmology, quintessence [Tsujikawa, 2013] and modified gravity scenarios [Clifton et al., 2012]. The quintessence model proposes a dynamic scalar field to be the cause of the universe's expansion, with dark energy changing over time, in comparison to the cosmological constant which remains constant over time. Dark energy is defined as having a negative equation of state parameter w_{de}, producing negative pressure which acts against the attractive force of gravity and drives further expansion of the universe. One method to determine the

most accurate model is to measure w from observations and evaluate which model it most closely matches. Ideally, one would want to measure how $w_{de}(z)$ varies over time, where redshift z serves as a proxy for the length of time before the present day, as this is necessary when considering models where dark energy varies over time. Its equation of state can be expanded into a Taylor expansion $w(z) = w_0 + w_z \frac{z}{1+z}$, giving another method of evaluating w as a function of time.

The cosmological constant is one proposed model behind dark energy and a possible cause of the acceleration of the rate of expansion of the universe. The ΛCDM model (see Section 1.1.2) accounts for dark energy through the cosmological constant Λ, which is closely linked to the energy density of the vacuum. Similar to matter and radiation, the vacuum energy has an associated pressure and density, and therefore an equation of state constant. The cosmological constant is favoured due to neatly accounting for the observed flatness of the universe and discrepancy between the too young extrapolated age of the universe when compared with the age of stars and abundance of galaxies.

The cosmological constant is defined to have pressure $P = -\rho$ and equation of state parameter $w_\Lambda = -1$, making it a possible cause of the expansion of the universe. Should observations find the dark energy equation of state parameter w sufficiently close to -1, it would provide evidence for the validity of the cosmological constant theory of dark energy over the competing theories.

If we remind ourselves of the continuity equation shown in Equation 1.1.10 and the equation of state for a fluid as shown in equation 1.1.12 and assume that the dark energy equation of state parameter is a function of a such that $w_{de} = w_{de}(a)$, we can replace $P_{de} = w_{de}(a)\rho$. Recalling that $\frac{dx}{x} = d(ln(x))$ and integrating from ρ_{de} to $\rho_{de,0}$, the modern-day value of ρ_{de}, we can integrate Equation 1.1.10 to obtain

$$\begin{aligned} \rho_{de} &= \rho_{de,0} e^{-3\int_a^1 [1+w_{de}(a')] d(ln(a'))} \\ &= \rho_{de,0} e^{3\int_0^z \frac{[1+w_{de}(z')]}{1+z'} dz'}, \end{aligned} \tag{1.1.27}$$

allowing the derivation of ρ_{de} from observations of $\rho_{de,0}$ in the present day.

1.1.13 The Density Parameter

It is often more convenient to use the dimensionless density parameters Ω for matter, radiation, the cosmological constant and curvature. The density parameters are defined as the ratio of the density to a defined critical density $\Omega = \frac{\rho}{\rho_c}$, where the critical density $\rho_c = \frac{3H^2}{8\pi G}$. We denote the density parameters corresponding to matter, radiation, the cosmological constant and curvature as Ω_m, Ω_r, Ω_Λ and Ω_k. For matter energy density ρ_m and radiation energy density ρ_r, these can be written as

$$\begin{aligned} \Omega_m &= \frac{8\pi G}{3H^2}\rho_m, \\ \Omega_r &= \frac{8\pi G}{3H^2}\rho_r. \end{aligned} \tag{1.1.28}$$

Dimensionless density parameters also exist for the cosmological constant and the curvature, and are given as:

$$\begin{aligned} \Omega_\Lambda &= \frac{\Lambda}{3H^2}, \\ \Omega_k &= \frac{k}{a^2H^2}. \end{aligned} \tag{1.1.29}$$

The 1st Friedmann Equation from Equation 1.1.9 can be written as

$$H(a)^2 = H_0^2(a^{-4}\Omega_{r,0} + a^{-3}\Omega_{m,0} + a^{-2}\Omega_{k,0} + \Omega_{\Lambda,0}) \tag{1.1.30}$$

where the 0 subscript indicates the values of the density parameters at the present day when $t_0 = 0$ and a_0=1. If we use $a(t) = (1+z)^{-1}$ and use Equation 1.1.27 to represent the uncertainty in the equation of state parameter for the dark energy w_{de}, we can rewrite it as

$$H(a)^2 = H_0^2((1+z)^4\Omega_{r,0} + (1+z)^3\Omega_{m,0} + (1+z)^2\Omega_{k,0} + \Omega_{de,0}e^{3\int_0^z \frac{[1+w(z')]}{1+z'}dz'} \tag{1.1.31}$$

From this, it can be seen that the evolution of the universe is governed by these density parameters, so one would expect that observations of the universe over time

could be used to study how the density parameters vary over time. We use these density parameters Ω over the density ρ because they are dimensionless and scaled by ρ_c.

1.1.14 Cosmological Parameters

From the various cosmological equations explained in the previous sections, it is clear that the cosmology of the universe is determined by the values of the cosmological parameters. A cosmological model makes predictions of observations based on these parameters, making it possible to evaluate the model by attempting to constrain these parameters and comparing to predictions. The cosmological model leaves its influence on the modern day observed universe, so it should be possible to probe the model through observations of effects that are most clearly influenced by these parameters.

There are a number of ways to use observation to probe the cosmology of the universe, but this project focuses on calculating statistics that relate correlation between pairs of objects to the scale. These correlation statistics are functions of real space distance or harmonic modes between each possible pair of objects in the studied dataset. These statistics have distinct shapes that indicate how much power or correlation is contained at each scale. Specifically, the real space two-point correlation function and the power spectrum are the most commonly used and will be detailed in Section 1.3.1.

The Hubble parameter H, the equation of state parameter w and the matter density parameter Ω_m, which is comprised of Ω_{cdm} and Ω_b for cold dark matter and baryonic matter respectively, have been proven to play a role in influencing the shape of the correlation function and the power spectrum. The derivative of the equation of state parameter w with respect to scale factor a is frequently written as $w_a = -\frac{\mathrm{d}w}{\mathrm{d}a}$, and in standard ΛCDM cosmology $w = -1$ and $w_a = 0$.

Another important cosmological parameter that influences weak lensing is σ_8, the amplitude of mass density fluctuation in the universe on spheres of radius $8h^{-1}$MPc at $z = 0$, which is used as a measure of an unbiased normalisation of the observed matter power spectrum. Consequently, σ_8 influences the CMB and weak lensing power spectra and is another parameter that we seek to constrain in order

to evaluate cosmological models.

Related to σ_8 is A_s, the amplitude of the mass fluctuations in the primordial power spectrum. It is defined as $P_{primordial} = A_s k^{-n_s}$, where n_s is the spectral index. The modern day power spectrum is related to the primordial power spectrum through considering the growth and modulation of the k modes (the Fourier coefficients of the physical scale) from structure formation, and this relation is approximate due to the non-linear regime. We obtain

$$P(k,z) \sim D(z)T(k)P_{primordial} = D(z)T(k)A_s k^{-n_s} \tag{1.1.32}$$

where $T(k)$ is the transfer function which modulates the k modes through the structure formation up until the modern day, and $D(z)$ is the growth factor which describes the growth of the k modes. As this is another parameter influencing the observed power spectrum, we can seek to constrain it with weak lensing.

The final relevant cosmological parameter is the reionisation optical depth, τ, which measures the opacity of the CMB radiation to a free electron and the distance travelled before electron scattering.

1.2 Gravitational Lensing

Evaluating techniques of studying cosmology from weak lensing data is the core focus of this thesis. This section will outline the concepts and equations key to the field of weak lensing, which is a type of gravitational lensing, and the related topics. These related topics will include the basic method underpinning the process of obtaining the convergence (see Section 1.2.4) map from shear data (see Section 1.2.5). However, more specific reconstruction techniques using wavelets, such as the wavelet pure mode estimator, will be discussed in chapter 3.

Gravitational lensing occurs when the gravitational force of a mass deflects the path of a light ray from the path it would have taken in the absence of this gravitational force. In the interest of being concise, the intermediate steps of derivations will not be shown, and full reviews that cover the skipped steps can be found in Bartelmann and Schneider [2001] and Kilbinger [2015].

1.2.1 Gravitational lensing formalism

In an inhomogeneous universe, varying matter densities cause gravitational tidal fields that deflect the travel path of light rays. This light deflection also causes the observed shape of source objects to appear distorted and correlated, which is the observable effect of cosmic shear.

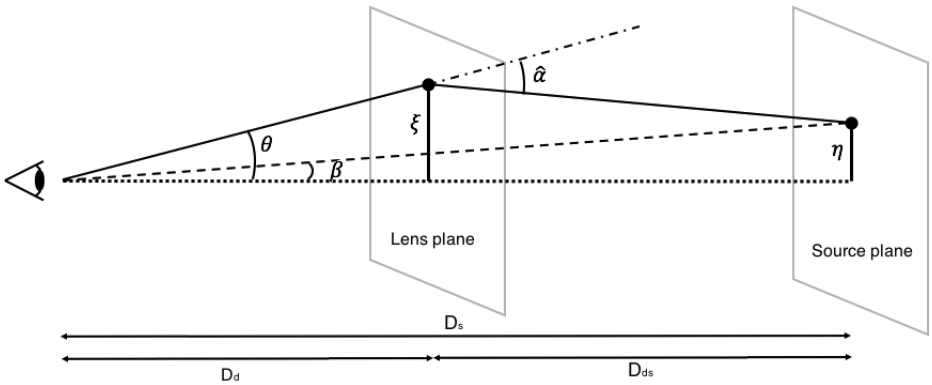

Figure 1.1: Figure illustrating a simple single lens system. The source galaxy is at position η on the source plane and has angular position β. The lensed image appears at ξ on the lens plane and has angular position θ. The deflection angle is represented by $\hat{\alpha}$. This diagram was created by Z. M. Vallis for use in this thesis.

A simple single-lens gravitational lensing system is comprised of the back-

ground source image on the source plane, an intervening lensing object on the lens plane and the observer who detects the lensed image. Fig. 1.1 displays such a system as an example. D_s represents the distance from the observer to the source, D_d the distance from the observer to the deflecting lens and D_{ds} the distance from the lens to the source. The position of the source on the source plane is denoted by η and the impact parameter on the lensing plane is denoted by ξ. Angle β describes the position of the source, angle θ the position of the apparent image and angle $\hat{\alpha}$ is the deflection angle.

This type of lensing system is common when the lensing is caused by a galaxy or galaxy cluster, which have small radial extent compared to the distances involved, so a thin lens approximation can be applied. For cosmic shear the lensing is the cumulative effect of the infinitesimally small thin lenses comprised of the LSS along the path of the photon, and the thin lens approximation holds since the volume of the matter is small compared to the large distances involved. Additionally, the overall lensing caused by the LSS is small enough that assumption that the deflection angle is small holds when considering an observer viewing the lensed galaxy.

The deflection angle can further be related to the positions of the source and image on their respective planes as such

$$\eta = \frac{D_s}{D_d}\xi - D_{\mathrm{ds}}\hat{\alpha}(\xi). \tag{1.2.1}$$

Using the definitions $\eta = D_s\beta$ and $\xi = D_s\theta$, and defining the scaled deflection angle $\alpha(\theta) = \frac{D_{ds}}{D_s}\hat{\alpha}(D_d\theta)$, this can be rewritten as the lens equation

$$\beta = \theta - \alpha(\theta). \tag{1.2.2}$$

Applying Fermat's principle to the space-time metric and integrating along the light path allows the deflection angle to be defined as

$$\hat{\alpha} = -\frac{2}{c^2}\int \nabla_{\perp}^{p}\phi \mathrm{d}x \tag{1.2.3}$$

where c is the speed of light in a vacuum, x is the proper spatial coordinate from the metric and $\nabla_{\perp}^{p}$ is the gradient of the gravitational potential ϕ (not to be confused with azimuthal angular coordinate φ) with respect to proper coordinates, taken perpendicular to the path the light is travelling along. We use ϕ to denote the

gravitational potential of the field causing the lensing, which can be related to the underlying matter density δ through Poisson's equation as

$$\nabla^2\phi(r,\theta,\varphi) = \frac{3\Omega_m H_0^2}{2a(r)}\delta(r,\theta), \tag{1.2.4}$$

where r is the comoving radial distance from the observer, (θ,φ) denotes the angular position on the sky, Ω_m is the matter density parameter, $H_0 = H(t = t_0)$ is the present-day value of the Hubble parameter, and $a(r)$ is the cosmological scale factor parameter.

1.2.2 The 2D Lensing Potential

The 2D lensing potential ψ is defined such that $\alpha = \nabla\psi$ and relates to the Newtonian gravitational potential ϕ as

$$\psi(\theta,r) = \frac{2}{c^2}\int_0^r \mathrm{d}r' \frac{f_K(r-r')}{f_K(r)}\phi(f_K(r')\theta,r'). \tag{1.2.5}$$

The parameter f_K is defined depending on curvature K as

$$f_K(r) = \begin{cases} K^{-\frac{1}{2}}\sin(K^{\frac{1}{2}}r), & \text{for } K > 0 \text{ (spherical)} \\ r, & \text{for } K = 0 \text{ (flat)} \\ (-K)^{-\frac{1}{2}}\sinh((-K)^{\frac{1}{2}}r), & \text{for } K < 0 \text{ (hyperbolic)} \end{cases} \tag{1.2.6}$$

Applying the Fourier-Bessel transform in Eq. D.1 to Eq. 1.2.5 allows the representation of the lensing potential ψ, in relation to the gravitational potential ϕ, in Fourier-Bessel space,

$$\psi_{\ell m}(k) = \frac{4}{\pi c^2}\int_{\mathbb{R}^+}\mathrm{d}r r^2 j_l(kr)\int_0^r \mathrm{d}r' f_k(r,r')\int_{\mathbb{R}^+}\mathrm{d}k' k'^2 j_l(k'r')\phi_{\ell m}(k';r), \tag{1.2.7}$$

where this value does not weight for the number of galaxies $N_{gal}(z)$. Subsequently Eq. 1.2.7 can be combined with Eq. D.2 to relate the lensing potential ψ to the matter overdensity δ in harmonic space as

$$\psi_{\ell m}(k) = \frac{6\Omega_M H_0^2}{k^2\pi c^2}\int_{\mathbb{R}^+}\mathrm{d}r r^2 j_l(kr)\frac{1}{a(r)}\int_0^r \mathrm{d}r' f_k(r,r')\int_{\mathbb{R}^+}\mathrm{d}k' k'^2 j_l(k'r')\delta_{\ell m}(k',r). \tag{1.2.8}$$

1.2.3 Weak lensing

Gravitational lensing can be divided into strong lensing and weak lensing. Strong lensing occurs when the lensing is strong enough to significantly distort the observed shape into multiple images, arcs or Einstein rings. Strong lensing can be used as a probe for studying cosmology and focuses on individual lenses such as galaxies, which tend to be relatively few in number.

The focus of this thesis is weak lensing of the LSS, which while possessing a much weaker signal can be observed as a subtle effect caused by the LSS in all directions on the sky. Weak lensing occurs when the gravitational field is not sufficient to distort the observed image to the point where there are multiple images or significant stretching occurs. Cosmic shear, the gravitational lensing caused by the LSS, is a weak lensing signal where the intervening matter is not dense enough to lens the light into arcs or rings. In the case of weak lensing, the distortion of the galaxy's shape is very small compared to the galaxy's intrinsic shape and it is not possible to discern information from only one weakly lensed galaxy. Instead, weak lensing must be studied statistically over a large number of galaxies, and the signal is often small enough that it is easily obscured by noise or systematics such that large data sets are preferable to counteract this.

The Jacobian matrix A_{ij} describes the change in shape caused by the lensing potential ψ and can be defined by taking the derivative of Eq. 1.2.2

$$A_{ij} = \frac{\partial \beta}{\partial \theta} = \left(\delta_{ij} - \frac{\partial^2 \psi(\theta)}{\partial \theta_i \partial \theta_j}\right) = \begin{pmatrix} 1-\kappa-\gamma_1 & -\gamma_2 \\ -\gamma_2 & 1-\kappa+\gamma_1 \end{pmatrix} \tag{1.2.9}$$

where $i,j = (1,2)$. From this, convergence κ and shear γ are defined as

$$\kappa = -\frac{1}{2}(\partial_1\partial_1 + \partial_2\partial_2)\psi = \frac{1}{2}\nabla^2\psi \tag{1.2.10}$$

$$\gamma_1 = -\frac{1}{2}(\partial_1\partial_1 - \partial_2\partial_2)\psi; \quad \gamma_2 = \partial_1\partial_2\psi \tag{1.2.11}$$

It can be seen that distortion in shape is defined by two qualities, the convergence κ and shear γ. The convergence is a scalar that contributes the isotropic part of the magnification of the galaxy's observed shape by changing its apparent brightness. For strong lensing, $A_{i,j}$ is singular and describes the translation of the source into

multiple images. For weak lensing, A_{ij} is invertible and maps the source onto only one image.

The convergence and shear are spin-0 and spin-2 signals respectively, meaning the convergence and shear signals are a scalar field with spherical symmetry and a field with two components and hence an order of two rotational symmetry. They can be related to the lensing potential ψ through

$$\begin{aligned} \kappa &= \frac{1}{2}[\eth\overline{\eth} + \overline{\eth}\eth]\psi \\ \gamma &= \frac{1}{2}[\eth\eth]\psi, \end{aligned} \tag{1.2.12}$$

where the operators $\eth$ and $\overline{\eth}$ are the spin raising and lowering operators respectively, defined on the celestial sphere as

$$\begin{aligned} \eth &= -\sin^s\theta\left(\frac{\partial}{\partial\theta} + \frac{i}{sin\theta}\frac{\partial}{\partial\varphi}\right)\sin^{-s}\theta \\ \overline{\eth} &= -\sin^{-s}\theta\left(\frac{\partial}{\partial\theta} - \frac{i}{sin\theta}\frac{\partial}{\partial\varphi}\right)\sin^{s}\theta. \end{aligned} \tag{1.2.13}$$

In a spherical harmonic representation this becomes

$$\begin{aligned} {}_0\kappa_{\ell m} &= -\frac{1}{2}\ell(\ell+1)\psi_{\ell m}, \\ {}_2\gamma_{\ell m} &= \frac{1}{2}\sqrt{\frac{(\ell+2)!}{(\ell-2)!}}\psi_{\ell m}, \end{aligned} \tag{1.2.14}$$

where ℓ and m are the angular harmonic coefficients. The observed shear exists natively on the surface of the celestial sphere and so in the full sky case ${}_2\gamma_{\ell m}$ can be decomposed using a spin-weighted spherical harmonic basis ${}_{\pm2}Y_{\ell m}$ like

$${}_{\pm2}\gamma(\boldsymbol{n}) = \sum_{\ell=0}^{\infty}\sum_{m=-\ell}^{\ell} {}_{\pm2}\gamma_{\ell m}\,{}_{\pm2}Y_{\ell m}(\boldsymbol{n}), \tag{1.2.15}$$

where ${}_{\pm2}Y_{\ell m}(\boldsymbol{n})$ are the standard spin-weighted spherical harmonic functions.

1.2.4 Convergence

Applying and substituting Eq. 1.2.4 and Eq. 1.2.5 into Eq. 1.2.10, the convergence can be given in terms of the mean matter density δ through

$$\kappa(\boldsymbol{\theta}) = \frac{3H_0^2\Omega_m}{2c^2}\int_0^{r_{\rm lim}} \frac{\mathrm{d}r}{a(r)} q(r) f_K(r)\delta(f_K(r)\boldsymbol{\theta}, r), \tag{1.2.16}$$

where $r_{\rm lim}$ is the limit in the radial direction, $q(r)$ is the lens efficiency that describes the strength of the lensing on the background galaxies at distance r. It is defined as

$$q(r) = \int_r^{r_{\rm lim}} \mathrm{d}r' n(r') \frac{f_K(r'-r)}{f_K(r)}, \tag{1.2.17}$$

where $n(r)$ is the source galaxy number density.

1.2.5 Shear

The shear describes the anisotropic distortion of the galaxy's observed shape and can be written in complex form as $\gamma = \gamma_1 + i\gamma_2 = |\gamma|e^{2i\varphi}$. Shear is a spin 2 quantity, meaning that it has rotational symmetry of 2, it is symmetric when rotated 180°.

As the shear is a spin-2 signal, the shear of an individual galaxy is comprised of the tangential component γ_t and the cross-component $\gamma_\times$. These can be defined for shear with angular direction $\boldsymbol{\theta} = (\theta, \varphi)$ as

$$\gamma_t = -\mathrm{Re}[\gamma e^{-2i\varphi}], \quad \gamma_\times = -\mathrm{Im}[\gamma e^{-2i\varphi}]. \tag{1.2.18}$$

When studying cosmic shear, only the shape of the galaxy is of interest, not the size, so it is useful to use reduced shear g which is defined as

$$g = \frac{\gamma}{1-\kappa} \tag{1.2.19}$$

Shear can be measured by studying the change in a galaxy's ellipticity. There are several ways of defining the ellipticity of a galaxy, the most common of which are through quadrupole moments of a source galaxy[Schneider and Seitz, 1995], which are defined as

$$Q_{ij} = \frac{\int \mathrm{d}\boldsymbol{\theta} q(I(\boldsymbol{\theta}))(\boldsymbol{\theta}_i - \overline{\boldsymbol{\theta}}_i)(\boldsymbol{\theta}_j - \overline{\boldsymbol{\theta}}_j)}{\int \mathrm{d}\boldsymbol{\theta} q(I(\boldsymbol{\theta}))} \tag{1.2.20}$$

where $i, j = (x, y)$ denote the Cartesian coordinates of observed galaxy, $(\boldsymbol{\theta})$ is the surface brightness distribution of of the source galaxy, $\overline{\boldsymbol{\theta}}$ denotes the centre of the source galaxy and $q(I)$ is a distribution function such as the Heaviside step function.

Galaxies have an intrinsic source ellipticity ϵ^s that would be observed in the absence of intervening lensing mass. This allows the observed ellipticity ϵ to be defined as

$$\epsilon = \frac{\epsilon^s + g}{1 + g^* \epsilon^s} \tag{1.2.21}$$

which in the weak lensing regime approximates to

$$\epsilon \approx \epsilon^s + \gamma \tag{1.2.22}$$

[Bartelmann and Schneider, 2001]

When assuming that the intrinsic ellipticities are randomly oriented, $\langle \epsilon^s \rangle = 0$, so the observed ellipticity acts as an unbiased estimator of shear as $\langle \epsilon \rangle = \gamma$.

1.2.6 E-B modes

The shear components γ_1 and γ_2 are not independent and can be alternately described by E-mode and B-mode signals, which are fields analogous to the electric field and magnetic field respectively. The E-modes and B-modes arise from the spin-2 nature of the shear signal and are a measure of the observed alignments of the shear around matter over- or underdensities caused by gravitational lensing. A representation of the E-modes and B-modes is shown in Fig. 1.2 [Amara and Kitching, 2016], with the lines indicating the alignment of the distorted galaxies. Gravitational lensing should only produce E-mode signals, but observations may display the presence of a B-mode field due to various systematic errors and biases.

From the spherical harmonic representation of the shear field in Eq. 1.2.15, we can write the E- and B-mode fields as comprised of the spin-2 harmonic coefficients

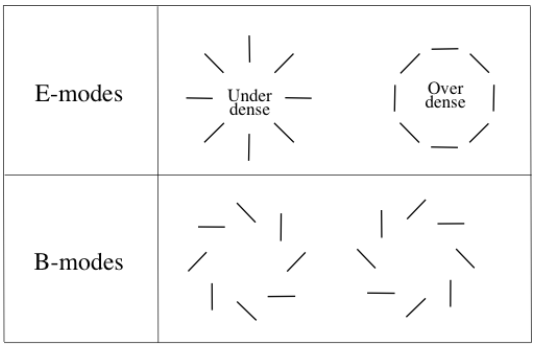

Figure 1.2: Diagram representing E-modes and B-modes. [Amara and Kitching, 2016]

$$\begin{aligned} E_{\ell m} &= -\frac{1}{2}({}_2\gamma_{\ell m} + {}_{-2}\gamma_{\ell m}), \\ B_{\ell m} &= \frac{i}{2}({}_2\gamma_{\ell m} - {}_{-2}\gamma_{\ell m}), \end{aligned} \tag{1.2.23}$$

which for a spin-2 signal, in harmonic representation, gives

$${}_{\pm 2}\gamma_{\ell m} = (\gamma_1 \pm i\gamma_2)_{\ell m} = -(E_{\ell m} \pm iB_{\ell m}). \tag{1.2.24}$$

These E/B modes can also be related to the E/B modes of the lensing potential ψ by a normalisation

$$\begin{aligned} \psi^E_{\ell m} &= 2N_{\ell,-2}E_{\ell m}, \\ \psi^B_{\ell m} &= 0. \end{aligned} \tag{1.2.25}$$

where $N_{\ell,-2}$ is the normalisation arising from applying the Fourier-Bessel transform defined as

$$N_{\ell,k} = \sqrt{\frac{(\ell+k)!}{(\ell-k)!}}. \tag{1.2.26}$$

These preliminaries can be used to construct various estimators for ${}_0\kappa(\boldsymbol{n})$ i.e. a convergence/'mass' map. Recalling that ψ^B should be zero for a pure lensing potential with no systematics and inserting Eq. 1.2.25 into Eq. 1.2.23, the shear can be related to the Fourier-Bessel transform of the lensing potential $\psi_{\ell m}$ [Castro et al., 2005] to match Eq. 1.2.14

$$ {}_2\gamma_{\ell m} = \frac{1}{2} N_{\ell,2} \psi^E_{\ell m}. \tag{1.2.27} $$

1.2.7 The Weak Lensing Power Spectrum, $C_l^{\psi\psi}(k,k')$

The means of convergence and shear are zero because they average out on the large scale, so it is necessary to look at the second-order moments of the convergence and shear. The 2D lensing potential power spectrum of the signal on spherical geometry $C_l^{\psi\psi}$ can be defined through the second-order moment of the lensing potential in spherical harmonic space $\langle \widetilde{\psi}^E_{\ell m} \widetilde{\psi}^{E*}_{\ell' m'} \rangle$, where the angular brackets denote average over spatial position,

$$ \langle \widetilde{\psi}^E_{\ell m} \widetilde{\psi}^{E*}_{\ell' m'} \rangle = C_l^{\psi\psi}(k,k') \delta^K_{ll'} \delta^K_{mm'}, \tag{1.2.28} $$

where δ^K denotes the Kronecker delta function, and ℓ and m are the spherical harmonic coefficients of θ and φ respectively.

Extending this, the 3D lensing potential power spectrum $C_l^{\psi\psi}(k,k')$ uses the same formalism in Fourier-Bessel space with $\langle \widetilde{\psi}^E_{\ell m}(k) \widetilde{\psi}^{E*}_{\ell' m'}(k') \rangle$, giving

$$ \langle \widetilde{\psi}^E_{\ell m}(k) \widetilde{\psi}^{E*}_{\ell' m'}(k') \rangle = C_l^{\psi\psi}(k,k') \delta^K_{ll'} \delta^K_{mm'}, \tag{1.2.29} $$

where k, ℓ and m are the spherical-Bessel variables corresponding to radial distance r and spherical harmonic θ and φ respectively. The lensing potential ψ is statistically homogeneous and isotropic in the angular direction, but not in the radial direction, as it is a 2D projection of the Newtonian potential along the radial direction.

The 3D lensing potential combines the 2D lensing potential with a radial element r, and is homogenous and isotropic in the 2D angular sphere component but is not in the radial component. Relating Eq. 1.2.27 to Eq. 1.2.29 it is possible to relate the cosmic shear to the 3D lensing power spectrum in Fourier space as

$$ \langle \widetilde{\gamma}_{\ell m}(k) \widetilde{\gamma}^*_{\ell' m'}(k') \rangle = \frac{1}{4} (N_{\ell,2})^2 C_l^{\psi\psi}(k,k') \delta^K_{ll'} \delta^K_{mm'}. \tag{1.2.30} $$

More explicitly, the shear power spectrum $C_l^{\gamma\gamma}$ can be related to the matter density power $C_l^{\kappa\kappa}$ through a Fourier transform of Eq. 1.2.16 and applying the Limber

approximation (see Appendix E and Lemos et al. [2017]; Limber [1953]; LoVerde and Afshordi [2008]) to give

$$C_l^{\kappa\kappa} = \frac{9H_0^4\Omega_0^2}{4c^4}\int_0^{r_H} \mathrm{d}r \frac{W^2(r)}{a^2(r)} P_\delta\left(\frac{\ell}{f_k(r)}, r\right), \tag{1.2.31}$$

where P_δ is the matter power spectrum and r_H is the horizon distance defined as the comoving distance for infinite redshift. See Bartelmann and Schneider [2001] and Kitching et al. [2011] for more details on how the Limber approximation was applied. The weighting function $W(r)$ is defined as

$$W(r) = \int_r^{r_H} G(r')\frac{f_k(r'-r)}{f_k(r')}\mathrm{d}r, \tag{1.2.32}$$

where source-distance distribution $G(r)\mathrm{d}r = p_z(z)dz$ with $p_z(z)$ being the galaxy redshift probability distribution function. It should be noted that Eq. 1.2.31 shows the projected power spectrum that integrates along the radial component, mixing the 3D k-modes into the 2D ℓ-modes and losing radial information and muddying some important 3D features, making it less sensitive to cosmological parameters [Kilbinger, 2015].

Transforming Eq. 1.2.10 and 1.2.11 into Fourier space (see Appendix B) and equating the $\widetilde{\psi}$, the following relation is obtained

$$\widetilde{\gamma}_l = \frac{(l_1 + il_2)^2}{\ell^2}\widetilde{\kappa}_l = e^{2i\theta}\kappa_l, \tag{1.2.33}$$

where l_1 and l_2 are the complex components of the ℓ mode corresponding to the γ_1 and γ_2 components of the shear γ and θ is the polar angle of the complex representation of ℓ. This finds that $C_l^{\gamma\gamma} = C_l^{\kappa\kappa}$, hence the shear power spectrum is equivalent to the convergence power spectrum in the flat-sky limit and relates to the density power spectrum through 1.2.31 similarly.

There exist other higher-order statistics such as the bi-spectrum and tri-spectrum, but these are more computationally intensive to calculate and are less efficient in probing cosmology, so the power spectrum is typically used as the standard statistic for analysis. The real space correlation function is commonly used in weak lensing studies and is not significantly affected by masks in the data, but

has more complicated covariance properties and the dependence of the correlation function on the matter power spectrum varies between real space angles and redshift bins. The 3D cosmic shear signal has a radial component in addition to the angular components and there are correlations between redshifts of the signal, not just between angular distances. Future research in the field of 3D cosmic shear therefore seeks to take into account the radial component. However, for this thesis we concern ourselves primarily with shear data in projection. When accounting for the redshift typically approximations such as the Limber approximation and tomographic binning are used (see Section 1.2.8).

1.2.8 Observational Considerations

There are a number of complications with using weak lensing that must be accounted for. The source galaxies possess intrinsic shape and alignment which cannot be observed, so it is unknown how much the observed ellipticity deviates from the intrinsic ellipticity. This can be compensated for when using large numbers of galaxies by assuming that their intrinsic ellipticities are randomly oriented and therefore the mean averages to zero. However there is also the possibility that nearby galaxies might have been influenced by their shared environment that caused their intrinsic ellipticities to become aligned [Joachimi and Bridle, 2010; Troxel and Ishak, 2014]. Additionally, if a galaxy is close to a lensing mass, the tidal field of the lensing mass could cause this galaxy's alignment to correlate with the lensing effect. One possible way of dealing with the problem of intrinsic alignment is the nulling technique developed by Joachimi and Schneider [2010].

As another example, the image of the galaxy will also be smeared by the point-spread function (PSF) due to effects from the atmosphere and by the mechanics of the detector, which presents an issue due to the weakness of the weak lensing signal. The PSF can be accounted for with various methods which employ a point-like object such as a star to calibrate, and calculations have been performed to evaluate the required accuracy of calibration required for cosmic shear analysis [Paulin-Henriksson et al., 2008].

The redshifts used for weak lensing surveys are photometric redshifts, which are derived from the photometric data of the galaxies. The observed Spectral Energy

Distribution (SED) of a galaxy is compared with a library of templates (of simulations or galaxies with known redshifts) and fitting methods, such as χ^2 minimisation or Bayesian statistics, are applied to determine the closest match and therefore the estimated redshift [Bolzonella et al., 2000][Benitez, 2000].

Weak Lensing Approximations

The observed data exist on the sky, which has the shape of a curved surface of a sphere, so any studies performed on this data must take this geometry into account. There are several approximations that are often applied to account for this, but as we will see these approximations have their limitations and it would be preferable to develop a technique to fully encapsulate the 3D geometry of the data.

For many current observations (e.g. galaxy groups or clusters) the information in the weak lensing signal occurs on small angular scales. This allows the flat-sky approximation [Bernardeau et al., 2011] to be used, treating the sky as a flat 2-dimensional plane and for analysis of the weak lensing data replacing the spherical harmonic transforms (see Appendix C) with Cartesian Fourier transforms (see Appendix B), which are easier to calculate. However, the cosmic shear exists on larger scales, and future surveys will expand the scale of observations and cover larger areas of the sky, where the flat-sky approximation may no longer hold.

The Limber approximation (see Appendix E and LoVerde and Afshordi [2008]), typically applied to correlation functions such as the power spectrum, is valid over small angular scales, where the radial modes vary little over the volume being surveyed. It approximates the spherical Bessel functions with Dirac delta functions during analysis of the weak lensing data, simplifying the integrations to be performed and making the calculations significantly less computationally intensive. The Limber approximation holds on the scales used for cosmological analysis where $\ell \geq 100$ in the power spectrum where ℓ is the harmonic coefficient of the angle.

One of the issues with 3D lensing studies is that the radial component provides another element of computation and, if treated as continuous, calculations involving it can get computationally intensive. The tomographic binning can be used to try and get around this by dividing the observations into redshift bins in order to simplify

calculations involving the radial component. The drawback of this is that redshift binning does not capture information on radial scales smaller than the bin widths, so it is necessary to establish a balance between precision and efficiency. Using tomographic redshift bins only approximates the true 3D properties of the data, so attempts have been made to study the data in spherical harmonic space instead in order to fully utilise the 3D information of the observations.

For the research in this thesis, the focus is on analysis of the data on 2D surface of the 3D sphere, representing the curved sky, not accounting for the range of redshift data, although this provides a promising avenue for future research.

Data Masks

Real data will usually be incomplete, missing data in certain areas of the sky due to flaws in the observation method. Also, masking usually occurs when areas of the sky cannot be observed due to limitations of the observation method or when sections of data must be discounted due to flaws in the observation that cannot be removed. The most straightforward cause of masks is from improperly functioning pixels in the observation equipment used, giving incorrect data that must be removed. Another source of masks is point sources, typically bright stellar objects with a circular profile that obscure neighbouring galaxies. For sufficiently large point-sources, their light may cause 'saturation spikes' that contaminate the light from the nearby galaxies [Hikage et al., 2011].

Masks cause mixing of power on different scales due to the missing data as the lack of data gives an incorrect representation of the statistics of the real signal. Another effect of masks is they cause the mixing of E-modes and B-modes, which causes problems for analysis methods that rely on the signal being primarily E-modes and systematic effects causing B-modes. This effect on E-modes and B-modes (and one potential method of dealing with this) is the focus of chapter 3 and discussed in further detail there. Masks also affect the Fourier transform, which needs the presence of all of the data to be fully accurate. These combined effects result in a significant effect on the derived correlation function and power spectrum.

Cuts in Fourier Space

Analogous to data masks in real space, Fourier/spherical harmonic space cuts are another way sections of data may be absent from the data. These cuts manifest as sections of data with a range of ℓ or k modes not being present, which correspond to missing data on certain angular scales or radial scales respectively. It is expected that cuts in data should have a noticeable effect on the derived power spectrum, as removing data on certain scales limits the sampling of the power spectrum. Cuts in harmonic space do not translate directly to cuts in real space, so correlation functions should be less significantly affected by such cuts than the power spectrum. In the 3D case, cuts on the radial k mode and angular ℓ mode can influence each other if tomographic redshift bins are used. Specifically, the impact of k mode cuts are felt by the ℓ modes when $k \geq \frac{\ell}{r_{\rm max}} \gtrsim \ell/3000 z_{\rm max} h^{-1}$Mpc for distances probed up to $z_{\rm max}$, limiting the ℓ modes that can be probed for a given k mode cut [Kitching et al., 2014].

1.2.9 Reconstruction on the Plane - the Kaiser-Squires estimator

The most commonly used method used to reconstruct the convergence map is the Kaiser-Squires (KS) reconstruction/inversion [Kaiser and Squires, 1993]. Transforming the convergence and shear, as defined in equations (1.2.12), into Fourier space allows the relation of the convergence and shear to be expressed. On the plane, provided that the planar approximation holds, this is done by solving the inverse equation of Eq. 1.2.33, which is often stated as

$$\widetilde{\gamma}_l = \mathcal{E}\widetilde{\kappa}_l, \tag{1.2.34}$$

where $\widetilde{f}$ denotes the Fourier transform of f, ℓ_x,ℓ_y are the Fourier coefficients of the spatial coordinates on the plane and

$$\mathcal{E} = \frac{\ell_1^2 - \ell_2^2 + i2\ell_1\ell_2}{\ell_1^2 + \ell_2^2}. \tag{1.2.35}$$

This is inverted and uses the property $\mathcal{E}^{-1} = \mathcal{E}^*$ to obtain a the KS estimator for the convergence in Fourier space,

$$\widetilde{\kappa}_l = \mathcal{E}^* \widetilde{\gamma}_l. \tag{1.2.36}$$

Applying the inverse Fourier transform to this $\widetilde{\kappa}_l$ estimator will give the convergence in real space, which can be used to construct a map of convergence from shear observations.

It should be noted that the KS method makes no attempt to accommodate any masking of data, treating the masked areas as absence of relevant data. While this is useful in its simplicity, it has drawbacks as cosmic shear analysis is heavily influenced by the mask and this can result in inaccurate results if one fails to consider the mask, some of which will be discussed in later chapters.

In addition to this, reconstructing the convergence map through the KS estimator effectively is a method of separating the E-modes and B-modes as described in Section 1.2.6. However, as shall be later discussed in Section 3.3 in chapter 3, this does not fully account for the incomplete data caused by masking and hence the E-modes and B-modes recovered this way are inaccurate. In effect, the KS estimator method corresponds to the harmonic pseudo estimator with masking neglected, as described in Section 3.3.

1.2.10 Reconstruction on the Sphere

An analogous equation can be obtained in the spherical case [Wallis et al., 2017] by using the spherical harmonic transform to give

$$\hat{\gamma}_{\ell m} = \mathcal{D}_\ell \hat{\kappa}_{\ell m}, \tag{1.2.37}$$

where ℓ and m are the harmonic coefficients of the spatial coordinates and

$$\mathcal{D}_\ell = \frac{-1}{\ell(\ell+1)} \sqrt{\frac{(\ell+2)!}{(\ell-2)!}}. \tag{1.2.38}$$

The process of reconstructing the convergence map involves inverting this relation in spherical harmonic space in a similar method to the Kaiser-Squires estimator on the plane, in order to find the Kaiser-Squires estimator on the sphere

$$\hat{\kappa}_{\ell m} = \mathcal{D}_{\ell}^{-1} \hat{\gamma}_{\ell m}. \tag{1.2.39}$$

Finally, performing the inverse spherical harmonic transform on $\kappa_{\ell m}$ allows the convergence map κ to be recovered.

1.3 Statistics and Analysis Methods

1.3.1 Basic statistics

The statistics relevant to this are detailed in this section for the purpose of reference and clarity. In this project, the data sets under observation are either galaxy catalogues containing observed properties of each individual galaxy, or simulated shear maps. In the case of using galaxy catalogues, the data is converted into shear maps based on sorting galaxies into different pixels based on their sky location and finding the weighted mean of the ellipticity at each pixel. The use of these statistics can apply to a set of data maps, simulated or resampled, or to an individual data map when considering the statistics as applied solely to the map over its constituent pixels. When discussing a population of data sets, whether real or simulated, these are characterised by their underlying true statistics and it is through estimators that one seeks to find the true values of these statistics.

This section will cover the statistics used throughout all chapters, and in cases where certain methods are used only in one chapter, these will be detailed in that specific section.

Mean

Given a set of data x of size N, the mean $\overline{x}$ is the expected value when sampling from x, and as the number of samples tends towards infinity the true mean of the data set μ. The expectation value $\mathrm{E(x)}$ is an estimator of the true mean μ over repeated samples, and frequently is used interchangeably with the mean. The expectation value for x is also written as $\langle x \rangle$, which also denotes the ensemble mean.

When discussing a probability distribution, where each possible value x_i has associated probability p_i, the expectation value $\mathrm{E(x)}$ is

$$\langle x \rangle = \overline{x} = \sum_{1=i}^{N} x_i p_i. \tag{1.3.1}$$

In this thesis, we primarily use the arithmetic mean as each possible outcome x_i has equal $p_i = 1/N$. The arithmetic mean of data set x is defined as

$$\overline{x} = \frac{1}{N}\sum_{1=i}^{N} x_i. \tag{1.3.2}$$

When discussing the mean of an individual data map, Eq. 1.3.2 is used, where the data set x is the set of pixels in the data map under consideration.

Standard deviation and variance

The standard deviation σ of data set x is a measure of the dispersion of the data set, specifically the degree to which the data points deviate from the mean. The standard deviation is the square root of the variance, which is defined as

$$\begin{aligned} \sigma^2(x) &= \langle x - \overline{x} \rangle \\ &= \langle x^2 \rangle - \langle x \rangle^2 \\ &= \frac{1}{N}\sum_{1=i}^{N} x_i^2 - \overline{x}^2. \end{aligned} \tag{1.3.3}$$

It should be noted that in this thesis, the notation σ will be used for other quantities, in most cases the degree of smoothing, and care will be taken to distinguish these quantities from the standard deviation through subscripts.

Covariance

The covariance is a two-point statistic measuring the correlation between two data sets x and y, and when $y = x$ the covariance reduces to the variance. The covariance is defined as the expectation value

$$\begin{aligned} \mathrm{Cov(x,y)} &= \langle x - \overline{x} \rangle \langle y - \overline{y} \rangle \\ &= \langle xy \rangle - \overline{xy} \\ &= \frac{1}{N}\sum_{0=i}^{N} (x_i - \overline{x})(y_i - \overline{y})^*, \end{aligned} \tag{1.3.4}$$

where the asterisk indicates complex conjugation if the data is complex.

Root-mean square

The root-mean-square (RMS), also known as the quadratic mean, of a data set x is the square root of the arithmetic mean of the square of the data points in x.

$$x_{\mathrm{RMS}} = \sqrt{\langle x^2 \rangle} \quad = \sqrt{\frac{1}{N} \sum_{0=i}^{N} x_i^2}. \tag{1.3.5}$$

The RMS is related to the arithmetic mean $\overline{x}$ and standard deviation σ by

$$x_{\mathrm{RMS}}^2 = \overline{x}^2 + \sigma^2, \tag{1.3.6}$$

hence if the variance of the data is $\sigma \sim 0$, the RMS is close to the mean, and if the mean of the data is $\overline{x} \sim 0$, the RMS is close to the variance. The latter case is expected when finding the RMS of shear and convergence maps, as by definition the mean of these maps is close to 0.

1.3.2 Two-point Statistics

Here we describe the relevant higher order two-point statistics.

The Correlation Function

Given an independent variable, if one measures a data set sampled from points along this variable, one can find the correlation between any two points on this signal. The correlation between two points is the extent to which they have a statistical relationship with each other, and if uncorrelated then they are independent of each other. In context of this thesis, the variable under consideration is a signal or data map. The correlation function ξ is a two-point statistic containing information of the correlation between each pair of points in the analysed signal, for all pairs of two points, as a function of the distance between each pair of points. Some examples of the signal f being considered may be the CMB temperature variation, the cosmic shear signal or the matter overdensity signal. The general form of the correlation function for signal f is

$$\xi(\boldsymbol{\theta}, \boldsymbol{\theta}') = \langle f(\boldsymbol{\theta}) f(\boldsymbol{\theta}') \rangle, \tag{1.3.7}$$

where * indicates the conjugate, $\boldsymbol{\theta} = (\theta, \varphi)$, $\boldsymbol{\theta}' = (\theta', \varphi')$ are the spatial coordinates of each point, and ℓ and m are the spherical harmonic coefficients. If the signal f is in the form of a data map on the curved sky, this can be expanded to

$$\begin{aligned}\xi(\boldsymbol{\theta},\boldsymbol{\theta}') &= \langle f(\boldsymbol{\theta}) f(\boldsymbol{\theta}') \rangle \\ &= \Big\langle \sum_{\ell m} a_{\ell m} Y_{\ell m}(\boldsymbol{\theta}) \sum_{\ell' m'} a_{\ell' m'} Y^*_{\ell' m'}(\boldsymbol{\theta}') \Big\rangle,\end{aligned} \tag{1.3.8}$$

where where $a_{\ell m}$ is the value of the spherical harmonic transform of the signal f at specific ℓ, m and $Y_{\ell m}$ are the spherical harmonic functions (see Appendix C). The correlation function is in effect a function of spatial separation that quantifies the correlation between two points on the signal at different physical distances of separation. The definition in Eq.1.3.8 gives the auto-correlation function, which is what the term 'correlation function' is used to mean in this thesis. If instead two different signals f and g were used to find $\langle f(\boldsymbol{\theta}) g(\boldsymbol{\theta}') \rangle$, this gives the cross-correlation function.

This is frequently applied to the weak lensing signal to find the shear correlation function. Due to the shear being comprised of the tangential and cross components as in Eq. 1.2.18, one can obtain two autocorrelations, $\langle \gamma_t \gamma_t \rangle$ and $\langle \gamma_\times \gamma_\times \rangle$, and one cross-correlation, $\langle \gamma_t \gamma_\times \rangle$. As the cross-correlation is zero provided the universe is parity-symmetric, the 2-point correlation function of the shear can be given as

$$\xi_\pm(\theta) = \langle \gamma_t \gamma_t \rangle(\theta) \pm \langle \gamma_\times \gamma_\times \rangle(\theta). \tag{1.3.9}$$

The advantage of the correlation function is its ease of use and straightforwardness. However, the most commonly used formulations do not fully take into account the 3D dimensions of the astronomical data observed on the sky, including the redshift coordinate. The correlation function preserves only information relating to the real space distances, neglecting the information that can be derived from scale properties of the data in harmonic space. Unlike the power spectrum, where the modes are uncorrelated, the strength of correlation function at different values of the spatial angle parameter is more likely to be correlated, making it more difficult to handle the data. Additionally, masking caused by incomplete data has a significant effect on the accuracy of the correlation function.

Power Spectrum

The power spectrum is a two-point statistic measuring the power of a signal as a function of frequency through evaluating the auto-correlation of the signal in spherical harmonic, or frequency, space. From this, it is possible to calculate which frequencies contain the most power in a signal.

The lensing power spectrum C_l can be calculated from the lensing signal in harmonic space $a_{\ell m}$ through

$$C_l = \langle a_{\ell m} a^*_{\ell m} \rangle = \frac{1}{2l+1} \sum_{m=-\ell}^{l} |a_{\ell m}|^2. \tag{1.3.10}$$

Therefore, observed data in real space can undergo a spherical harmonic transform to obtain $a_{\ell m}$ and this can be used to recover the power spectrum C_l. Equation 1.3.10 can be inverted to obtain

$$\langle a_{\ell m} a^*_{\ell' m'} \rangle = C_l \delta^K_{ll'} \delta^K_{mm'}, \tag{1.3.11}$$

where δ^K is Kronecker delta. Relating this back to Equation 1.3.8, it is possible to calculate the correlation function from the power spectrum as

$$\begin{aligned} \xi(\boldsymbol{\theta}, \boldsymbol{\theta}') &= \sum_l C_l \sum_m Y_{\ell m}(\boldsymbol{\theta}) Y^*_{\ell' m'}(\boldsymbol{\theta}') \\ &= \sum_l \frac{2l+1}{4\pi} C_l P_l(\boldsymbol{\theta} \cdot \boldsymbol{\theta}'), \end{aligned} \tag{1.3.12}$$

where $P_l(\boldsymbol{\theta} \cdot \boldsymbol{\theta}')$ is the Legendre polynomial and $\boldsymbol{\theta} \cdot \boldsymbol{\theta} = \cos(\beta)$ with β being used to refer to the angle between $\boldsymbol{\theta}$ and $\boldsymbol{\theta}'$. Using Equation 1.3.12, the correlation function can be calculated from a given power spectrum C_l. This can be used to take a model C_l and find the corresponding correlation function, and then compare this theoretical correlation function to the correlation function recovered from the data through a certain analysis method. By comparing the theoretical correlation function with the recovered correlation function with a particular analysis method, it should be possible to measure how accurately the analysis method performs. However, caution must be taken when deriving these two-point correlation statistics from

data if the true values of the data under consideration are unknown, as they can be significantly affected by masks and cuts in harmonic space.

The power spectrum has the advantage that on the large, linear scales, where the matter overdensity is significantly smaller than 1, the modes are uncorrelated and grow independently. However, the independence of the different modes does not hold on small scales, where the non-linear regime begins, as the modes begin to interfere with one another and the influence of complex structure growth and baryonic feedback come to dominate the signal. Despite this, there has been much study into understanding the power spectrum at these scales and from simulations its properties at these scales can be understood [Cooray and Hu, 2001; Hu and White, 2001; Pielorz et al., 2010a; Takada and Jain, 2009a]. The power spectrum is also affected by cuts in harmonic space or masks in real space. Cuts in harmonic space remove specific modes and data masks cause mixing of power on different scales and presenting misleading information due to limited data, both of which cause inaccuracies and bias in the power spectrum. Like the common formulations for the two-point correlation function, most usages of the power spectrum neglect to account for the full 3D nature of the data and rely on approximations.

1.3.3 Convergence Map Analysis Methods

In addition to correlation functions such as the power spectrum, there are a number of analysis methods that can be performed directly on the convergence maps. These include using higher-order spectra [Munshi et al., 2012], measuring the degree of isotropy of the map [Marques et al., 2018], evaluating correlation with locations of galaxy cluster locations and galaxy distribution maps [Chang et al., 2017; Vikram et al., 2015], identification of peaks and voids [Chang et al., 2017], peak count statistics [Lin and Kilbinger, 2015a] and Minkowski Functionals [Mecke et al., 1994a]. The last two of these will be the main focus of chapter 2, and the Minkowski Functionals will also be used in chapter 4.

1.3.4 Peak counts

The peak count of a mass map is simply the number of local maxima that can be identified. This can be used as a statistic by evaluating the number of peaks above a

certain threshold. The convergence map peaks trace matter overdensities and are closely associated with galaxy clusters and halo structures, hence the peak count statistic as a function of threshold proves a useful tool for constraining cosmological parameters [Kacprzak et al., 2016a; Lin and Kilbinger, 2015a,b; Lin and Kilbinger, 2018; Marian et al., 2009; Peel et al., 2017] and probing the halo mass function and non-Gaussian features of the LSS [Shirasaki, 2017]. The main drawback to peak count analysis is the presence of noise, which can produce false peak detections and obscure the identification of true peaks. We attempt to deal with the noise through smoothing the data, as detailed individually for each chapter. Full details on how the peaks are defined and identified are given in Section 2.2.3.

The peak count function is an evaluation of the number of peaks at a given SNR threshold, which is sensitive to the cosmological parameters and evolution of the universe [Shirasaki, 2017]. The SNR map, also used for the computation of Minkowski functionals, is derived from the convergence map κ, its mean $\overline{\kappa}$ and its standard deviation σ as

$$\nu(\boldsymbol{\theta}) = \frac{\kappa(\boldsymbol{\theta}) - \overline{\kappa}}{\sigma}. \tag{1.3.13}$$

From an SNR map on a pixel grid, the local peaks are identified by evaluating if for a given pixel, the SNR value is greater than the eight surrounding pixels that are orthogonally and diagonally adjacent. Further detail on this definition we use is given in Section 2.2.3.

1.3.5 Minkowski Functionals

The Minkowski Functional (MF) is a function characterising the geometrical properties, such as distance measures, of a space. When extended to higher dimensions, they are functions containing information about the morphological properties of the space and provide a statistical measure of the morphological features of random fields. In this thesis and in the wider field of MF analysis for cosmology [Petri et al., 2013; Schmalzing et al., 1996], the MFs are used to interpret and describe the topological features of a field, in this case focusing on the 2D field unless otherwise noted.

Using the MFs this way as a tool for understanding the topology of the universe and its constituent matter [Kerscher et al., 1997; Mecke et al., 1994a] allows probing of high-order non-Gaussian properties [Munshi et al., 2012; Petri et al., 2013; Schmalzing and Buchert, 1997] arising from the random fluctuations in the cosmological data. For a 2D random field, three MFs V_0, V_1 and V_2 can be obtained, which respectively serve as a measure of the area, boundary length and Euler characteristic of the excursion set of the 2D field as a fraction of the total area of the field. Typically the MFs are derived from the SNR map as described in Eq. 1.3.13, which is the definition we opt to use. These MFs are defined for a field ν through the following equations [Petri et al., 2013]

$$V_0(\nu_0) = \frac{1}{A}\int \Theta(\nu(\mathbf{x}) - \nu_0)\mathrm{da}, \tag{1.3.14}$$

$$V_1(\nu_0) = \frac{1}{A}\int \delta(\nu(\mathbf{x}) - \nu_0)\sqrt{\nu_x^2\nu_y^2}\mathrm{da}, \tag{1.3.15}$$

$$V_2(\nu_0) = \frac{1}{A}\int \delta(\nu(\mathbf{x}) - \nu_0)\frac{2\nu_x\nu_y\nu_{xy} - \nu_x^2\nu_y y - \nu_y^2\nu_x x}{\nu_x^2\nu_y^2}\mathrm{da}, \tag{1.3.16}$$

where Θ is the Heaviside step function, δ is the Dirac delta function, ν_x and ν_y denote partial differentiation of ν on the horizontal and vertical (or latitudinal and longitudinal) coordinate directions respectively, A is the total area of the map, da denotes the area element of the map, ν is the SNR map and ν_0 is the SNR threshold. When integrating over the area with da, we integrate along the x and y axes and then divide the result by the total area of the map calculated from the pixel array, as we want the Minkowski functionals expressed as a fraction of the overall area. We make the Dirac delta functions more appropriate for computation by dividing the range of SNR values into bins ν_i and using

$$\delta = \begin{cases} 1, & \text{if } \nu_i - \frac{1}{2}\Delta\nu_i \leq \nu(\mathbf{x}) \leq \nu_+\frac{1}{2}\Delta\nu_i \\ 0, & \text{otherwise} \end{cases} \tag{1.3.17}$$

where ν_i is the SNR threshold of bin i and $\Delta\nu_i$ is the width of the SNR threshold bins. For Gaussian random fields, the power spectra can be constructed from the Minkowski functional and vice versa. Non-Gaussian fields require approximations

or perturbation methods to relate the power spectra to the Minkowski functionals [Petri et al., 2013].

The MFs are used in chapter 2 and chapter 4 to quantify the morphological information of the reconstructed convergence maps. First, the convergence map is converted into SNR map ν through Eq. 1.3.13 and equations 1.3.14, 1.3.15, 1.3.16 are used to construct the MFs from the SNR map. When dealing with data maps projected to the 2D plane in chapter 2, the gradient map is straightforward to calculate. The spherical case requires us to account for the geometry of the data on the sphere when calculating the partial derivatives, this is done using the following equations [Wandelt et al., 1998]

$$\frac{\partial}{\partial\varphi}Y_{\ell m}(\theta,\varphi) = imY_{\ell m}(\theta,\varphi), \tag{1.3.18}$$

$$\frac{\partial}{\partial\theta}Y_{\ell m}(\theta,\varphi) = -m\cot\theta Y_{\ell m}(\theta,\varphi) - [\ell(\ell+1)-m(m-1)]^{\frac{1}{2}}Y_{\ell m-1}(\theta,\varphi), \tag{1.3.19}$$

$$\frac{\partial^2}{\partial\varphi^2}Y_{\ell m}(\theta,\varphi) = -m^2Y_{\ell m}(\theta,\varphi), \tag{1.3.20}$$

$$\frac{\partial^2}{\partial\theta^2}Y_{\ell m}(\theta,\varphi) = \left(\ell(\ell+1)-\frac{m^2}{\sin\theta^2}+\cot\theta\frac{\partial}{\partial\theta}\right)Y_{\ell m}(\theta,\varphi), \tag{1.3.21}$$

$$\frac{\partial^2}{\partial\theta\varphi}Y_{\ell m}(\theta,\varphi) = \left(im^2\cot\theta - im[\ell(\ell+1)-m(m-1)]^{\frac{1}{2}}e^{i\varphi}\right)Y_{\ell m-1}(\theta,\varphi). \tag{1.3.22}$$

The code `HEALPix` [Górski et al., 2005] is used to calculate the derivatives in spherical harmonic space on the sphere for the spherical case. The SNR maps retain the sampling scheme (see McEwen and Wiaux [2011b]); they are converted into a `HEALPix` map for analysis, and subsequently the calculated gradient fields are converted back into a map with equiangular sampling. The band limits are selected such that minimal information is lost in the conversion. In all cases, the integrations are performed on the pixelised array, hence the total area used is given as the total number of pixels examined. When the data is masked, we evaluate only the unmasked subsection of the map and treat the number of unmasked pixels as the total area.

1.4 Wavelets

We make use of wavelets for the E-B separation method applied in chapter 3 and chapter 4. This section will cover the wavelet formalism, with more detail on how wavelets are used for weak lensing analysis being given in the aforementioned chapters. A signal can be converted into a series of wavelets and associated scaling function through the use of wavelet transforms, analogous to the Fourier transform and spherical harmonic transform as described in the Appendix. The use of scale-discretised wavelets allows the structure of the map to be preserved at each relevant angular scale, and in the presence of masks this allows extraction of greater detail than the harmonic method. A spin scale-discretised directional wavelet is used, which allows for the localised capture of information in both real and harmonic space. Further details of the construction of these wavelets are given in McEwen et al. [2015], McEwen et al. [2018] and Leistedt et al. [2017].

Wavelets provide a way of representing a signal through a series of basis functions, analogous to a Fourier series [Antoine et al., 2008; Graps, 1995]. Using a signal with time and frequency information as an example, a Fourier series of this signal has only frequency resolution but no time resolution. Wavelets are localised in both time and frequency domains and so can capture both the time and frequency information of the signal.

The wavelet basis functions are all derived from translations and dilations of a 'mother wavelet' $\Psi(x)$. For a given scaling factor λ and translation factor τ, a derived wavelet is defined as

$$\Psi_{\lambda,\tau}(x) = \frac{1}{\sqrt{\lambda}}\Psi\left(\frac{x-\tau}{\lambda}\right). \tag{1.4.1}$$

These derived wavelets yield a window that is applied to a section of the signal to calculate the wavelet transform. The window is shifted along the signal and the wavelet coefficient is calculated at each point to capture the time information. To capture the scale information, the wavelet is dilated by a set amount and the wavelet coefficient is calculated for each dilation. A scaling function Φ is used to capture the signal information at the lowest scales (this should not be confused with the symbol ϕ used to denote the gravitational potential).

Wavelets on the plane

On a 2D plane, the wavelet coeffcients for each scale and translation factor are given by the continuous wavelet transform, which convolves the original signal with the wavelet as

$$W_{\lambda,\tau} = (f \circledast \Psi)(x) = \int f(x)\Psi^*_{\lambda,\tau}(x)dx, \tag{1.4.2}$$

where $f(x)$ is the real space signal, * denotes the complex conjugate and $\circledast$ denotes convolution. The inverse wavelet transform reconstructs the original signal from the wavelet coefficients and the wavelets as such

$$f(x) = \int W_{\lambda,\tau}\Psi_{\lambda,\tau}(x)d\tau d\lambda. \tag{1.4.3}$$

The wavelet transforms must fulfil certain admissibility conditions for the forward and inverse transforms to be exact and able to reconstruct the original signal with no information lost. The admissibility condition for a wavelet is

$$\int \frac{|\widetilde{\Psi}(\omega)|^2}{|\omega|}d\omega < +\infty, \tag{1.4.4}$$

where $\widetilde{\Psi}$ is the Fourier transform of Ψ. The admissibility condition implies that $\tilde{\Psi}$ is zero when frequency $\omega = 0$.

Wavelets on the sphere

In the case of the cosmic shear the signal exists on the curved sky, so frequency is replaced by angular scale and the time coordinate is replaced by spatial coordinates $\omega = (\theta, \varphi)$ on the sphere, where $\theta \in [0, \pi]$ and $\varphi \in [0, 2\pi)$. Leistedt et al. [2015] have constructed wavelets on the ball, which prove useful for analysing the weak lensing signal as it exists on the curved sky. Wavelet scaling is governed by the angular modes ℓ and m. The scaling factor λ remains the same, but the translation is replaced by a rotation around the sphere, denoted by rotation operator $\mathcal{R}_\omega$ that is parameterised by angular position ω only in the axisymmetric case. In the non-axisymmetric case, direction plays a role and the rotation operator becomes $\mathcal{R}_\rho$ where $\rho = (\alpha, \beta, \gamma)$ where $\alpha \in [0, 2\pi), \beta \in [0, \pi], \gamma \in [0, 2\pi)$ are Euler angles.

Previously the wavelet scaling has been continuous, but this is impractical as it would require integrating over an infinite number of scales in order to fully capture all of the information. Scale-discretised wavelets [Wiaux et al., 2008] do not treat the scale as continuous, but split it into discrete integer scales that are each associated with a specific wavelet coefficient. This allows each scale wavelet to probe the different scales and combine contributions from all terms, which is much more efficient. The maximum wavelet scale J is defined as $\lceil \log_\lambda(L-1) \rceil$, where $\lceil \cdot \rceil$ denotes the ceiling function, λ is the wavelet scaling factor, and the minimum wavelet scale J_0 can be freely selected provided that the scaling function ${}_s\Phi(\boldsymbol{n})$ covers the signal at low ℓ-mode.

The `S2LET` code [Leistedt et al., 2013] used throughout this thesis implements the fast spin spherical harmonic transform code `SSHT` [McEwen and Wiaux, 2011b] to facilitate the wavelet transform and form scale-discretised wavelets on the sphere.

For the function ${}_sf(\boldsymbol{n})$ with spin s, the wavelet forward transform is given as the convolution of ${}_sf(\boldsymbol{n})$ with the wavelet ${}_s\Psi^j(\boldsymbol{n})$ and a scaling function ${}_s\Phi(\boldsymbol{n})$ as

$$\begin{aligned} W_{sf}^{s\Psi^j}(\rho) &= \int_{S^2} d\Omega(\boldsymbol{n}) {}_sf(\boldsymbol{n}) [\mathcal{R}_\rho {}_s\Psi^j]^*(\boldsymbol{n}), \\ W_{sf}^{s\Phi}(\boldsymbol{n}') &= \int_{S^2} d\Omega(\boldsymbol{n}) {}_sf(\boldsymbol{n}) [\mathcal{R}_{\boldsymbol{n}'} {}_s\Phi]^*(\boldsymbol{n}), \end{aligned} \tag{1.4.5}$$

where $W_{sf}^{s\Psi^j}(\rho)$ denotes the wavelet coefficient of the wavelet ${}_s\Psi^j(\boldsymbol{n})$ at a discrete scale $j = J_0, J_1, ..., J$, where J_0 and J are the minimum and maximum wavelet scales respectively, and $W_{sf}^{s\Phi}(\boldsymbol{n}')$ denotes the wavelet coefficient of the scaling function ${}_s\Phi(\boldsymbol{n})$, which captures the information on the largest scale. The integration is defined over the surface of the sphere S^2 where $\mathrm{d}\Omega(\boldsymbol{n}) = \sin\theta \mathrm{d}\varphi \mathrm{d}\theta$. The rotation operators on rotation group $SO(3)$ and on the sphere S^2 are denoted by $\mathcal{R}_\rho$ and $\mathcal{R}_{\boldsymbol{n}'}$ respectively, with $\boldsymbol{n} = (\theta, \varphi) \in S^2$ and $\rho \in SO(3)$ parameterised by the Euler angles (α, β, ξ).

Conversely, the original function ${}_sf(\boldsymbol{n})$ is reconstructed exactly through a convolution of the wavelet and scaling function and the corresponding coefficients as

$$\begin{aligned} {}_sf(\boldsymbol{n}) &= \int_{S^2} d\Omega(\boldsymbol{n}') W_{sf}^{s\Phi}(\boldsymbol{n}') [\mathcal{R}_{\boldsymbol{n}'} {}_s\Phi](\boldsymbol{n}) \\ &+ \sum_{j=J_0}^{J} \int_{SO(3)} d\mu(\rho) W_{sf}^{s\Psi^j}(\rho) [\mathcal{R}_\rho {}_s\Psi^j](\boldsymbol{n}), \end{aligned} \tag{1.4.6}$$

where $\mathrm{d}\mu(\rho) = \sin\beta \mathrm{d}\alpha \mathrm{d}\beta \mathrm{d}\xi$ denotes integration over the Euler angles. Here, J denotes the maximum wavelet scale, λ is the wavelet scaling factor, and the minimum wavelet scale J_0 can be freely selected provided that the scaling function ${}_s\Phi(\boldsymbol{n})$ covers the signal at low ℓ-mode. Further information on the construction of spin scale-discretised wavelets is found in McEwen et al. [2015].

The wavelets ${}_s\Psi^j(\boldsymbol{n})$ and scaling function ${}_s\Phi(\boldsymbol{n})$ must have their harmonic coefficients fulfill the following conditions for all ℓ if the transform is to be invertible and to contain the full information of the original function:

$$\frac{4\pi}{2\ell+1}|{}_s\Phi_{\ell 0}|^2 + \frac{8\pi^2}{2\ell+1}\sum_{j=J_0}^{J}\sum_{m=-\ell}^{\ell}|{}_s\Psi^j_{\ell m}|^2 = 1, \tag{1.4.7}$$

where ${}_s\Phi_{\ell m}$ and ${}_s\Psi^j_{\ell m}$ are the spherical harmonic transforms of ${}_s\Psi^j(\boldsymbol{n})$ and ${}_s\Phi(\boldsymbol{n})$.

CHAPTER 2

Investigating the effects of projections on the peak count and Minkowski Functionals of convergence maps

2.1 Introduction

Gravitational lensing has proven to be a useful tool for probing the cosmology of the Universe and the field is a rapidly growing one, with current surveys providing a wealth of weak lensing data (e.g. the Kilo Degree Survey [de Jong et al., 2013], the Dark Energy Survey [The Dark Energy Survey Collaboration, 2005]) and future surveys (e.g. *Euclid* [Laureijs et al., 2011], the Large Synoptic Survey Telescope [LSST Science Collaboration et al., 2009], the Wide Field Infrared Survey Telescope [Spergel et al., 2013]) promising to further expand the potential of the field. Gravitational lensing occurs when light from distant galaxies passes through mass overdensities, causing a distortion in the galaxy ellipticities detectable by observers. Cosmic shear refers to the weak lensing distortion caused by the Large Scale Structure (LSS) – intermediate matter between the galaxies and the observer. The distribution and evolution of the LSS is governed by the cosmological model of the Universe, hence the suitability of weak lensing studies of the LSS for probing cosmology. We can probe the structure of the LSS through cosmic shear to analyse dark energy, evaluate different cosmological models and constrain cosmological parameters; for a recent review see Kilbinger [2015].

Among the most commonly used cosmic shear analysis methods are two-point statistics (see Section 1.3.2) – the power spectrum or the correlation function – which probe the second-order properties of the cosmic shear. However, the power spectrum and correlation function average over phase information on the sky, and thereby reduce spatial information to a single angular or scale dependence, and cause mixing of angular modes. These statistics do not fully capture the non-Gaussian properties of the lensing matter and perform best on linear scales, where the modes are uncorrelated and grow independently, but lose effectiveness on smaller non-linear scales. Studies have been done attempting to model the resulting two-point statistics in the non-linear regime and to model the non-Gaussian properties with the power spectrum [Pielorz et al., 2010b; Takada and Jain, 2009]. Furthermore, partial sky coverage and masking of the data cause inaccuracies resulting from mixing of the E-modes and B-modes of the cosmic shear [Kilbinger et al., 2006] (see chapter 3 and chapter 4).

The increased precision and sky coverage of upcoming surveys can help to mitigate the drawbacks of these two-point statistics, but will not help to capture the non-Gaussian properties of the LSS. The non-linear and non-Gaussian properties of the LSS can potentially be better analysed by alternative statistics such as the peak counts of the convergence map [Lin and Kilbinger, 2015a] and Minkowski functionals (MFs) [Mecke et al., 1994a] (covered in Sections 1.3.4 and 1.3.5) such as the genus statistics [Matsubara and Jain, 2001], as well as higher-order spectra [Munshi et al., 2012].

The reconstructed convergence map is a useful tool in studying the non-Gaussian statistics, as it captures the non-Gaussian properties of the underlying matter density distribution [Bergé et al., 2010b; Pires et al., 2010b; Vikram et al., 2015]. The peak count statistic is a straightforward evaluation of the number of detected peaks of the reconstructed convergence map as a function of their SNR. The convergence map represents the line-of-sight integration of the gravitational lensing effect caused by the underlying matter field, and so their peaks trace the locations of maximum projected overdensities in the lensing structure and are associated with high-density galaxy clusters and halos, and hence are sensitive to the halo mass function and cosmological parameters [Marian et al., 2009]. The low SNR peaks are frequently contaminated by noise, so studies seeking solely to identify the locations of true peaks focus on high SNR peaks with SNR ≥ 3. However, peaks at SNR $1-2$ contain valuable cosmological information, provided the noise is accounted for [Kratochvil et al., 2010]. By binning the observed galaxies by redshift, it is possible to trace the evolution of the LSS over time. Previous studies have measured the effectiveness of peak count statistics at constraining cosmological parameters [Kacprzak et al., 2016a; Lin and Kilbinger, 2015a,b; Lin and Kilbinger, 2018; Peel et al., 2017]. For a range of SNR values the peaks can be used as tracers of dark matter halos and structure, and so therefore the non-Gaussianities in the matter distribution [Fan et al., 2010; Shirasaki, 2017].

There are a number of approaches to recovering mass maps from a catalogue of measured galaxy shapes. The most commonly used method for analysis of large weak lensing data sets is the Kaiser-Squires method [Kaiser and Squires, 1993], which is based on the direct inversion of observed shear field to the convergence

field. There are a number of well known draw backs to this method including noise growth on small scales, and errors due to survey boundaries. Due to its simplicity the Kaiser-Squires method is the standard method to recover mass-maps from data on large scales. For example, the Cosmic Evolution Survey (COSMOS; [Scoville et al., 2007]), the Canada-France-Hawaii Telescope Lensing Survey (CFHTLenS; [Heymans et al., 2012]) and the Dark Energy Survey (DES; [Flaugher et al., 2015]) Science Verification (SV) data [respectively, Chang et al., 2015; Massey et al., 2007; Van Waerbeke et al., 2013] all use this method. Other mass mapping techniques have also been developed. On the galaxy cluster scale parametric models [e.g. Jullo et al., 2007]) and non-parametric methods [e.g. Lanusse et al., 2016; Massey et al., 2015] have been presented. Other methods have been developed for 3D mass map reconstruction, to deal with masking and heavy noise-domination of the shear signal [Bacon and Taylor, 2003; Leonard et al., 2012, 2014; Massey et al., 2004; Simon, 2013; Simon et al., 2009; Taylor et al., 2004; VanderPlas et al., 2011]. Recently peak counts have been used to measure cosmological parameters from the DES Kacprzak et al. [2016b], where a planar projected mass map was used.

The methods discussed above performing reconstruction on the 2D plane all require a projection of the shear. Wallis et al. [2017] demonstrated the extension of the commonly used 'Kaiser-Squires' method to the sphere (see Section 1.2.10) and performed a comparison with projections, and this method was subsequently applied to DES data by Chang et al. [2017]. Wallis et al. [2017] have made their python code `massmappy`[1] publicly available and will be used in this project. Along with the publicly available `SSHT`[2] [McEwen and Wiaux, 2011b], this allows one to evaluate the comparative performance of different projections for the purpose of convergence map reconstruction on the 2D surface of the celestial sphere and we build upon their study for the analysis of projection effects on peak count statistics.

The Kaiser-Squires inversion applies non-locally to transform the dataset as a whole and does not take into account the mask. The common way of dealing with masked data when using the Kaiser-Squires method is to exclude data falling within the masked regions, but this breaks down when the masking covers large areas of

[1] http://www.massmappy.org
[2] http://www.spinsht.org

the sky, as investigated by Wallis et al. [2017]. We choose to use a simple mask that removes a solid area of the sky, and seek to investigate how it impacts the projected cases compared to the spherical case. This simple circular mask was chosen for ease of implementation and to more intuitively understand the results in context of the mask.

Future surveys will provide greater sky-coverage than before, with the upcoming *Euclid* survey covering 15,000 deg^2 [Amendola et al., 2013; Laureijs et al., 2011] and LSST [LSST Science Collaboration et al., 2009] covering 20,000 deg^2, compared to current surveys DES [The Dark Energy Survey Collaboration, 2005] at 5000 deg^2 CFHTLenS [Erben et al., 2013b] at 154 deg^2. As we move towards greater sky coverage in these upcoming surveys, it becomes necessary to fully understand the effects of planar projection and to seek possible alternatives to reconstruction on the plane. These surveys will cover larger areas of the sky, necessitating that we take the sky geometry into account and providing an incentive to move towards analysis directly on the sphere over planar approximations.

Previous analysis of peak counts and MFs have been performed on the projected plane because current surveys cover small areas of sky where a planar approximation holds. However with future surveys covering significantly larger areas of the sky, the geometry of the sky must be accounted for and it is expected that the projections will no longer accurately capture the full information of weak lensing data on the sky. While planar projection analysis has the advantage of being less computationally demanding than performing analysis on the sphere, the movement of research towards analyzing full-sky data necessitates examination of the performance of planar projections used for deriving statistics containing cosmological information compared to the spherical case.

In this chapter we investigate the effect of projections on peak count statistics and Minkowski functionals. Peak count statistics rely on accurate mass map reconstructions and minimisation of noise, which is a significant problem at low peak thresholds. Projections to the plane cannot preserve all the features of the spherical map and prioritise accuracy to different map properties, such as preserving angles or relative area. High resolution is required to detect the fine structure of the convergence map and to minimise the merging of closely positioned peaks during

projection. It is expected that these factors will influence the peak counts, resulting in distinct differences between projection methods. The Minkowski functionals [Kratochvil et al., 2012; Mecke et al., 1994a; Munshi et al., 2012; Petri et al., 2013; Schmalzing and Buchert, 1997] and genus statistics [Matsubara and Jain, 2001; Sato et al., 2003], may also be affected by how projections affect the geometry of the shear data. Alternative methods of deriving statistics from the convergence map involve additional data sets such as the CMB-LSS cross-correlation [Liu and Hill, 2015; Pearson and Zahn, 2014].

The focus of this chapter is to evaluate how the peak count statistic and Minkowski Functionals are affected for different projections to the plane. This is done by making convergence map reconstructions on the sphere from simulated data based on a CosmoSIS-generated power spectrum [Zuntz et al., 2015]. The peak counts are calculated from the SNR map instead of the convergence map itself, to allow for more natural thresholding. Most of the relevant background information is covered in Section 1, but Sections 2.2.1, 2.2.2 and 2.2.3 detail new important information. Section 2.3 will outline the methods used, including the reconstruction of the convergence map, details on smoothing the map during reconstruction, and method of peak detection and MF calculation. We present our findings in Section 2.4 and draw our conclusions in Section 2.5.

2.2 Background

2.2.1 Convergence map reconstructions

The most commonly used method of reconstructing the convergence map from shear data is the Kaiser-Squires (KS) estimator [Kaiser and Squires, 1993]. The KS estimator can be applied on the plane using Fourier transforms, or on the sphere using spherical harmonic transforms (see Appendices B and C). Details on the reconstruction of the convergence map on the plane and on the sphere are covered in Sections 1.2.9 and 1.2.10 respectively. We opt to use the straightforward KS method on the plane and sphere in order to keep the focus of this study on the effect of projection as the performance of these methods are well-studied, rather than adding in another factor of a newer and less well-tested reconstruction method. The reconstruction of the convergence map from simulated shear maps are performed with the `massmappy` code [Wallis et al., 2017] that uses equations (1.2.36) and (1.2.39), as well as for the reconstruction on the plane.

2.2.2 Projection from the 2D spherical surface to the 2D plane

When using standard planar Kaiser-Squires reconstruction (see Section 1.2.9) a projection from the sphere to a plane is required. As discussed in Wallis et al. [2017] such a projection can cause changes in the structure of the reconstructed convergence map, that increases as the angular size of the reconstructed area increases, and is dependent on the projection used. Here we test whether projections also impact the peak counts and Minkowski funcational measurements obtained from such maps, and to what extent.

For this study, five projections were used: two equatorial projections (Mercator, sine), and three polar projections (orthographic, stereographic, gnomonic). In this section we describe each projection and give visual examples [3] based on projections of the Earth from the globe to the plane with Tissot's indicatrices displayed to illustrate the distortion of shape for each projection. The lines used to indicate the latitude and longitude display the same values across the examples given.

The Mercator projection is given by

$$\begin{aligned} x &= \varphi - \varphi_0, \\ y &= \ln[\tan(\pi/2 - \theta/2)], \end{aligned} \tag{2.2.1}$$

where (x, y) are the planar coordinates, (θ, φ) are the spherical angular coordinates, and φ_0 is the central meridian. Typically, φ_0 is selected to be π. We define θ as the polar angle and φ as the azimuthal angle. This translates to θ representing latitude and φ, often represented by λ, representing longitude. An example of the Mercator projection applied to the Earth is displayed in Fig. 2.1. The Mercator projection is conformal, so the local angles are preserved in the projection, and does not include the poles. This can be seen in Fig. 2.1, where we also observe the consistency in scale along the equator and magnification further from the equator, independent of the longitude.

[3] Produced using the Basemap python package [Hunter, 2007], https://matplotlib.org/basemap/

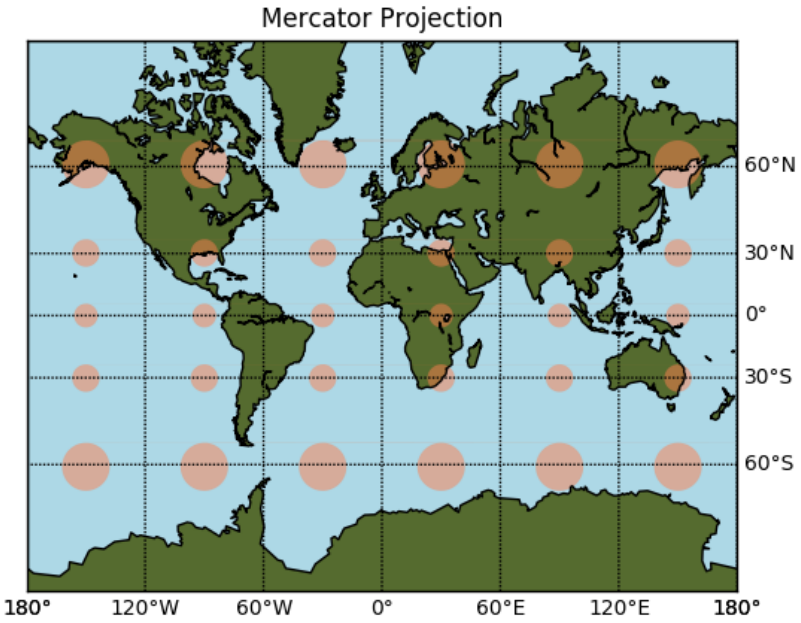

Figure 2.1: Example of the Mercator projection as applied to the map of the Earth, with Tissot's indicatrices displayed as orange circles. Created using Matplotlib Basemap toolkit [Hunter, 2007].

The sinusoidal projection is defined by

$$\begin{aligned} x &= (\varphi - \varphi_0)\sin(\theta) \\ y &= \theta. \end{aligned} \tag{2.2.2}$$

The sinusoidal projection preserves the relative areas of features on the spherical map, but is not conformal so distorts their shape and affects directionality. An example of the sinusoidal projection applied to the Earth is displayed in Fig. 2.6. In comparison to the Mercator projection, there is less observed magnification and along the equator it can be seen that there are no changes in shape or directionality, but diverging from the equator results in drastic changes in shapes on the map.

The polar projections display the map on the plane in polar coordinates, defined on the plane in the form $x = \rho\cos(\psi)$ and $y = \rho\sin(\psi)$. The polar projections do not cover the entire sphere in one plane, but instead are split into north and south hemispheres which are centred on the poles. On the southern hemisphere, the polar coordinate parameter θ for the northern hemisphere is replaced with $\pi - \theta$. The

stereographic projection, is a conformal polar projection, and defined by

$$\begin{aligned} \rho &= 2\tan\left(\frac{\theta}{2}\right) \\ \psi &= \varphi. \end{aligned} \tag{2.2.3}$$

The orthographic projection projects the sphere as if viewed from an infinite distance and is given by

$$\begin{aligned} \rho &= \sin(\theta) \\ \psi &= \varphi. \end{aligned} \tag{2.2.4}$$

The gnomonic projection is given by

$$\begin{aligned} \rho &= \tan(\theta) \\ \psi &= \varphi. \end{aligned} \tag{2.2.5}$$

The gnomonic projection is a projection that maps points on the surface of the sphere along a line through the centre of the sphere to the tangent plane. As a result, the

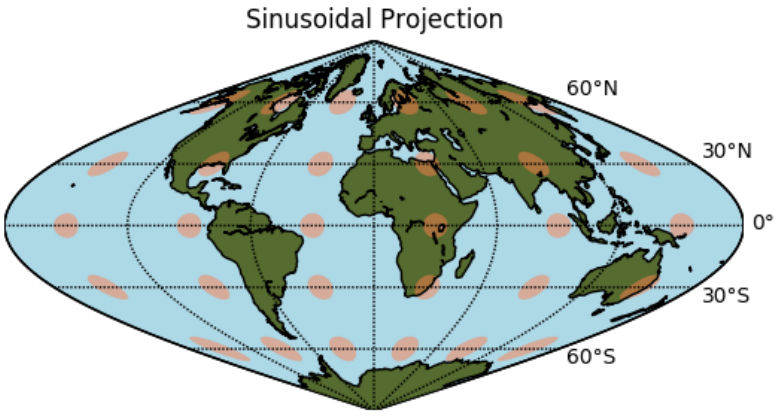

Figure 2.2: Example of the sinusoidal projection as applied to the map of the Earth, with Tissot's indicatrices displayed as orange circles. Lines indicating longitude denote the same positions as in the Mercator projection example. Created using Matplotlib Basemap toolkit [Hunter, 2007].

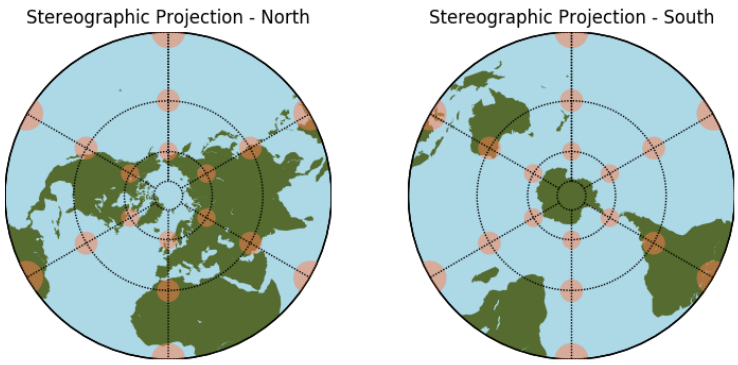

Figure 2.3: Example of the stereographic projection as applied to the map of the Earth, with Tissot's indicatrices displayed as orange circles. Lines indicating latitude and longitude denote the same positions as in the Mercator projection example. The projections display the north and south hemisphere for the globe, including the equator. Created using Matplotlib Basemap toolkit [Hunter, 2007].

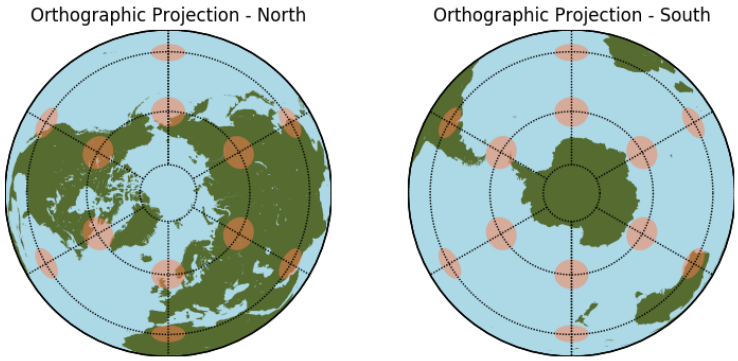

Figure 2.4: Example of the orthographic projection as applied to the map of the Earth, with Tissot's indicatrices displayed as orange circles. Lines indicating latitude and longitude denote the same positions as in the Mercator projection example. The projections display the north and south hemisphere for the globe, including the equator. Created using Matplotlib Basemap toolkit [Hunter, 2007].

maximum viewing angle is limited to be $\theta < \pi/2$, as $\theta = \pi/2$ is at infinity. As the viewing angle approaches $\pi/2$, the shape distortions become significant to the point of obscuring the original map data, hence we selected the viewing angle to be $\theta = \pi/4$. Therefore, the peak counts and the Minkowski Functionals are scaled accordingly to be proportional to the sky coverage of the other projections.

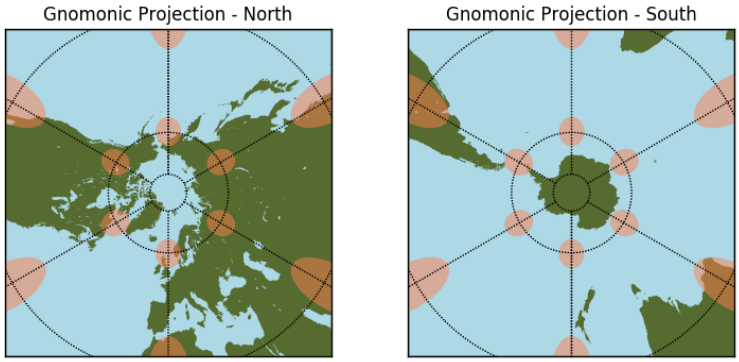

Figure 2.5: Example of the gnomonic projection as applied to the map of the Earth, with Tissot's indicatrices displayed as orange circles. Lines indicating latitude and longitude denote the same positions as in the Mercator projection example. The gnomonic projection cannot display the equator from the position centred on the poles, hence there must always be a degree of zooming in on a region. Created using Matplotlib Basemap toolkit [Hunter, 2007].

Examples of the polar projections applied to the Earth are displayed in Fig. 2.3, Fig. 2.4 and Fig. 2.5 for the stereographic, orthograpic and gnomonic projections respectively. From these examples it can be seen that the stereographic projection best preserves directionality and shape of the map, while the orthographic and gnomonic projections are reasonably accurate at the centrepoints of the projection while showing significant distortion further from the centre. The orthographic and gnomoic projection also display a more prominent cut-off around the projection's equator, due to the orthographic projection's more significant compression at its equator, and the gnomonic projection's cut-off being defined by the viewing angle used.

While we do not use the Mollweide projection in this chapter, chapter 3 and chapter 4 make use of it and hence it will be introduced here. The Mollweide projection, also called the elliptical projection, prioritises accurately preserving the relative area sizes on the map and is given by

$$x = \frac{1}{\pi}\sqrt{22}(\varphi - \varphi_0)\cos(\vartheta),$$
$$y = \sqrt{2}\sin\vartheta, \tag{2.2.6}$$

where ϑ here is defined as

$$2\vartheta + \sin(2\vartheta) = \pi\sin(\theta), \tag{2.2.7}$$

where we assume that the radius of the sphere is set to 1, and λ is the longitude,

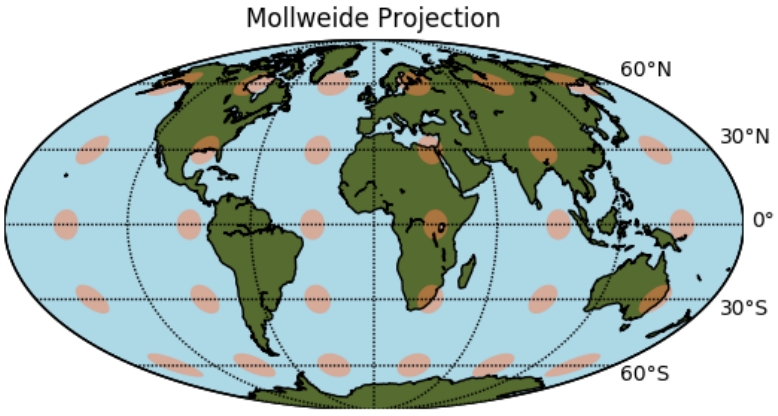

Figure 2.6: Example of the Mollweide projection as applied to the map of the Earth, with Tissot's indicatrices displayed as orange circles. Lines indicating longitude denote the same positions as in the Mercator and sinusoidal projection examples. Created using Matplotlib Basemap toolkit [Hunter, 2007].

When projecting a spin−2 quantity, for example shear or galaxy ellipticities, one must take account for the local rotations. A formalism for calculating these local rotations is outlined in Wallis et al. [2017] for both polar and equatorial projections and is implemented in the projection functions as part of the software package `SSHT`.

Each of these projections are displayed applied to convergence signal-to-noise maps in Fig. 2.7. Observing this figure and previous examples of the projection methods illustrate where the most significant degree of shape distortion occurs when compared to the original map. While these distortions may appear significant, it must also be kept in mind that often analysis is performed only on a smaller section of the sphere, which the projection will be centred on and therefore will be less distorted.

We use the fast and exact sampling theorem of [McEwen and Wiaux, 2011b] to sample the spherical signal, defining upper bandlimit L, to define the convergence map on the sphere. The projections are all centered on the same point and the polar projections display only the northern hemisphere. The planar convergence maps were constructed on the planes from the projected shear, allowing one to see the effect of each projection on the reconstruction. We can see that in all cases, the projected image becomes more distorted further from the centre of the projection, in the manner also illustrated by the projection example figures. Factors that are expected to affect the peak detection include the amount of distortion of the original image and how successfully the noise is smoothed in each projection. As it can be seen that the centres of each projection display less distortion, it is expected that the differences between projection methods will become significant only when evaluation of peak counts and MFs include these areas.

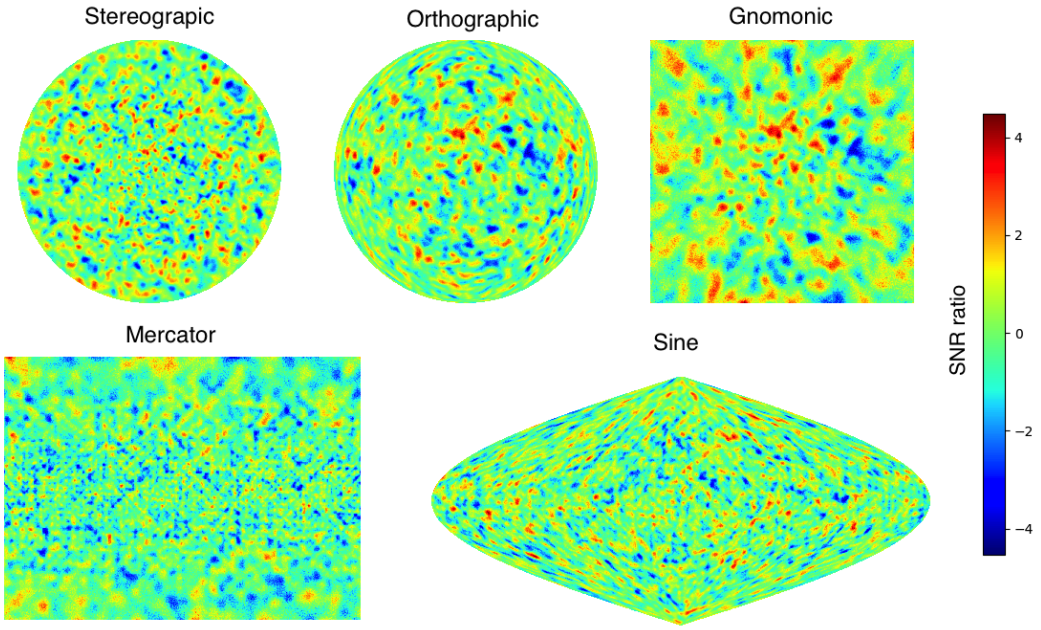

Figure 2.7: The Signal-to-Noise Ratio map obtained from convergence maps simulated from a template power spectrum, using the method described in Section 2.3 with a standard ΛCDM cosmology. The initial convergence map, which is not displayed, is generated on the sphere. The five displayed convergence maps are the original convergence map projected onto the plane through each of the five projections chosen to be analyzed. This is done by mapping each pixel on the sphere to the corresponding pixel on the planar representation, and taking the mean value when multiple pixels on the sphere are mapped to one pixel on the plane. The center of the projected map is defined as a point on the equator selected to be at the center of the flattened spherical map. From these convergence maps κ, the SNR maps are defined as $\nu(\boldsymbol{\theta}) = \frac{\kappa(\boldsymbol{\theta})-\bar{\kappa}}{\sigma}$. The maximum bandlimit is selected to be $L = 2160$, to match that used in Vikram et al. [2015], and the resolution for the projections (except the Mercator) is 2160, in order to ensure that the projections closely match the spherical map in detail and number of pixels.

2.2.3 Peak counts and Minkowski functionals

The two statistics we investigate are peak statistics and Minkowski functionals (MFs), which have been outlined in Sections 1.3.4 and 1.3.5. These statistics can be seen to be clearly influenced by the topology of the convergence map, hence why we choose to use these statistics to evaluate the influence of projection on reconstruction of said convergence map. Peak statistics refers to the number of local maxima in the reconstructed maps as a function of signal to noise of the peak. Minkowski functionals are descriptors of the topological features, which for 2D fields correspond to the area, boundary length and Euler characteristic as functions of SNR (signal-to-noise ratio) thresholds.

Peak counts in cosmology

The detection of convergence peaks has the straightforward purpose of identifying local maxima for the underlying matter density observed, but are also used for probing the halo mass function and placing constraints on cosmological models. This is typically done through evaluating the peak count density as a function of the signal-to-noise (SNR) value of the field, which is commonly referred to as the 'peak function'. This section will summarise how peak count statistics are used in cosmological analysis, although greater detail can be found in the papers referenced.

Convergence maps are tracers of matter density, with regions of greater convergence indicating higher matter densities. Therefore peaks in convergence maps should indicate the of regions centre of high matter density, such as dark matter halos. Hence the convergence peak count of the cosmic shear is expected to show influences of the universe's evolution and should vary for different cosmological models, especially at the 'tail' of the peak count distribution corresponding to very high mass peaks. Early examples of probing the non-Gaussian properties involved evaluating dark matter halos and their mass functions using the aperture mass for different cosmological models [Kruse and Schneider, 1999, 2000; Reblinsky et al., 1999]. These analyses that evaluate the peaks of halo masses are concerned with the true peaks and avoid false peaks; however including false peaks induced by noise and other effects can still allow for useful cosmological studies [Jain and Van Waerbeke, 2000; Van Waerbeke, 2000].

The two main purposes are peak count analysis are 'cluster-oriented' and 'cosmology-oriented' [Lin et al., 2016], with a degree of overlap between them. Cluster-oriented research focus on peaks with high SNR (typically > 4) and examine offset in position, variations in peak height, purity and completeness in order to identify galaxy clusters and their local maxima and cross-correlate them with galaxy cluster data from other sources. Cosmology-oriented peak count research focuses on peaks across a wider range of SNR ratios in order to constrain cosmology through comparison with predictions of peak counts from models. The lower SNR peaks are more likely to be false detections or caused by projections of the LSS rather than from dense matter halos, but nonetheless are included in models and hence useful for analysis.

Peak counts are non-Gaussian and not predicted through a single equation, but rather there are three common approaches to modelling the peak count: analytical formalism [Fan et al., 2010; Maturi et al., 2010; Shirasaki, 2017] , N-body simulations [Dietrich and Hartlap, 2010; Kratochvil et al., 2010] and the fast stochastic model [Lin and Kilbinger, 2015a,b; Lin et al., 2016] . The analytical formalism approach allows the modelling of the peak count function through an analytical formula. However, it has difficulties accommodating observation conditions found in real data such as masking and bias in photometric redshift and shape measurement, relies on separate external simulations to evaluate its errors, and the model has trouble to integrating physical astrophysical properties such as baryons and intrinsic alignment. The N-body simulation and fast stochastic model approaches are able to incorporate these observational problems and astrophysical influences, although the N-body simulation has the significant drawback of high computational times.

The purpose of evaluating the peak count statistic using these models is to compare with observations in order to constrain cosmology. Hence it is important to reduce potential error in results derived from observations, of which projection effects may be a cause.

Local peak identification

In order to identify peaks first we need to construct a signal-to-noise (SNR) map. The SNR map is the map containing the ratio of the convergence map at each

point to the standard deviation of the convergence map. In this thesis we apply peak finding to the SNR map in order to more intuitively define the peak thresholds and to account for different maximum values and variance between maps. This also holds the advantage of being able to distinguish true peaks with higher SNR from the lower SNR peaks that will be heavily noise-dominated. To reiterate from Section 1.3.4, the SNR map is constructed from the convergence map as

$$\nu(\boldsymbol{\theta}) = \frac{\kappa(\boldsymbol{\theta}) - \overline{\kappa}}{\sigma}, \tag{2.2.8}$$

where $\overline{\kappa}$ and σ denote the mean and standard deviation of the convergence map respectively. In the case of the polar projections, where the sphere is projected onto two separate planar maps (one for the north hemisphere and one for the south hemisphere), we calculate the mean and standard deviation over both projected hemispheres.

Peak count statistics typically evaluate the counts above a specific SNR threshold over a range SNR thresholds to extract cosmological information [Shirasaki, 2017]. For a selected SNR threshold, only peaks with values above this threshold are included in the final count.

A pixel is defined as being at a peak if the SNR value at this pixel is greater than the SNR values in the eight neighboring pixels. This requires the following conditions to be satisfied

$$\nu(\theta_{xy}) > \nu(\theta_{ij}) \text{ for } \begin{cases} x-1 < i < x+1; \\ y-1 < j < y+1; \end{cases} \quad \forall (i,j) \neq (x,y) \tag{2.2.9}$$

The advantage to this method is that it is straightforward to use and understand, but can result in false detection if the noise is not fully accounted for. This method is highly local and considers only a block of 9 pixels to determine if there is a peak or not, so therefore is expected to be less affected by large-scale shape distortions from projection. More sophisticated methods in the literature, such as the aperture mass detection [Dietrich and Hartlap, 2010; Marian et al., 2012; Schneider, 1996] have used tangential alignment of the shear map to identify peaks. We choose to use the 8-neighbour peak definition over these other methods because of its ease of use, and discuss the importance of pixelisation and image resolution for projection.

There are several potential drawbacks relating to this definition of a peak. It is relatively easy for noise to be falsely categorized as a peak, which we attempt to reduce by applying appropriate smoothing. We also expect to find that as the SNR threshold is increased, the proportionate effect of noise is reduced. It is possible that there will be cases where a distinct peak is spread out over neighboring pixels that have the same value, leading to no pixel being detected as a peak by this definition. Due to the way we evaluate peaks with our code, the calculations are performed to such a precision that this event is unlikely. Should such failures to detect a peak occur, we expect them to occur in low numbers compared to the total number of peaks. In cases where there are multiple smaller peaks in an area of high SNR, we treat each as separate peaks by this definition, which is valid as we are measuring distinct peaks regardless of height at which they occur. We also seek to minimise these effects by obtaining our results over a significant number of iterations such that any of these spurious peaks or undetected peaks are small in number compared to the real peaks. It is possible for some of these instances to occur as a result of shape distortion from projection, so if a projection leads to a high number of these instances such that there is a distinct impact, then it must be taken into account when evaluating said projection.

2.2.4 Minkowski functionals

Minkowski functionals in cosmology

In addition to peak count statistics we analyse the effect of projection on the Minkowski functionals (MFs). Minkowski functionals provide a statistical measure of the morphological features of random fields. They allow probing of high-order non-Gaussian properties [Munshi et al., 2012; Petri et al., 2013; Schmalzing and Buchert, 1997] arising from the random fluctuations in the shear data. The purpose of using MFs over more commonly used methods of probing non-Gaussian features is to directly analyse the topology of the 2D field. In this case, the field is the convergence field of the cosmic shear, which traces the LSS in the universe and hence MF analysis allows evaluation of the topology of the LSS projected along the line-of-sight to a 2D form. As the properties of the LSS are influenced by different cosmological models, so are the derived MFs, allowing the MFs to place constraints

on potential models through comparison with observations.

The MFs also provide a very simple and direct evaluation of the Gaussianity of the 2D random field under analysis, as the 2D Gaussian random field has a defined analytic form for the MFs (see Eq. 4.2.2 in Section 4.2) that can be compared directly to the field under consideration. The smaller the deviation from the analytic form of the MFs for the 2D Gaussian random field, the greater the Gaussianity of the evaluated field.

Minkowski functional definition

For a 2D random field, we can obtain three Minkowski functionals V_0, V_1 and V_2, which respectively serve as a measure of the area, boundary length and Euler characteristic of the excursion set of the 2D field as a fraction of the total area of the field. We refer to Section 1.3.5 for definition of the MFs, specifically Eq. 1.3.14, Eq. 1.3.15 and Eq. 1.3.16 for definitions of V_0, V_1 and V_2 respectively.

Minkowski functional evaluation

To calculate the MFs from the SNR map ν, we use equations 1.3.14, 1.3.15, 1.3.16. On the projected SNR maps, we simply take the gradient of the map at each point. For the spherical case, we make use of equations Eq. 1.3.18 through Eq. 1.3.22, using `HEALPix` [Górski et al., 2005] to perform these calculations in spherical harmonic space. As detailed in Section 1.3.5, the MFs are normalised by the size of the evaluated area, considering both the pixel grid and physical sky area covered, for projected and spherical cases.

2.3 Method

In this section, we describe the approach taken to assess the impact of any projection on peak count statistics and MFs. The details on how peak counts and MFs are evaluated are covered previously in Section 2.2.3. The general approach we take is to 1) make simulations of shear fields on the sphere, then 2) project these using each of the five selected projections, we then 3) reconstruct the convergence maps either on the sphere, or using planar Kaiser-Squires, and finally 4) measure the peak count statistics and Minkowski functionals in both cases.

Shear map generation

The simulations are produced by generating a simulated power spectrum by adding Gaussian noise to a template cosmic shear power spectrum generated with CosmoSIS [Zuntz et al., 2015] using a standard ΛCDM cosmology [$\Omega_m = 0.3$, $h_0 = 0.72$, $\Omega_b = 0.04$, $\tau = 0.08$, $n_s = 0.96$, $A_s = 2.1e-9$, $\Omega_k = 0.0$, $w = -1.0$, $w_a = 0.0$]. We use `massmappy` to generate the convergence map in harmonic space from the simulated power spectrum, such that the convergence map is based on a Gaussian random field. The angular size of each pixel depends on the bandlimit L used, such that the angular width of each pixel is $\frac{360^\circ}{2L-1}$ and the angular height of each pixel is $\frac{180^\circ}{L}$. We then apply smoothing to the convergence signal in harmonic space to mitigate the effect of noise and pixelisation, using Gaussian kernel $\mathcal{G}_l = e^{-\ell^2\sigma^2}$ where $\sigma = \pi/256$, which provides sufficient, but not excessive, smoothing. The code `SSHT` uses the theoretically exact spin spherical harmonic transform with McEwen-Wiaux (MW) sampling [McEwen and Wiaux, 2011b] to transform this harmonic representation of the convergence into the simulated convergence map on the sphere. The reduced shear map is then obtained from this simulated convergence map, and then random noise, in the form of a Gaussian distribution with $\mu = 0$ and $\sigma = 1$ multiplied by the standard deviation of the shear map which has average value of ~ 0.01, is added to each pixel at this stage. This value of ~ 0.01 is selected in order to correct the standard deviation of the shear, σ_γ, for the number of galaxies per pixel, N_{gal}, such that the corrected standard deviation is $\frac{\sigma_\gamma}{N_{gal}}$. At this point, the convergence map can be recovered and the peak counts calculated on the sphere. To evaluate the projections, the reduced shear data on the sphere is projected into one of

the five projections under examination. Following the projection onto the plane, the convergence map reconstruction is performed natively on the plane using standard Kaiser-Squires reconstruction. During the reconstruction step, another Gaussian smoothing is applied to account for noise, with a user-defined σ. In each case, the smoothing at this step is performed either on the spherical or projected data. We perform the smoothing in the same geometry as that in which the statistical analysis takes place. This reflects what would be done in practice: the projection of the data onto a geometry first in which all subsequent smoothing and data analysis then takes place.

The maps are processed as pixel arrays, with the dimensions being defined by the maximum bandlimit parameter L for the sphere and the user-defined resolution parameter for the projections. We select the maximum bandlimit to be either $L = 2160$ to match Vikram et al. [2015] (for the peak count function) or $L = 512$ (for the MF analysis). Hence, for $L = 2160$ the angular pixel size given as width by height is $0.083^\circ \times 0.083^\circ$ and for $L = 512$ the angular pixel size given as width by height is $0.352^\circ \times 0.352^\circ$. The number of pixels in each projected map is defined by the resolution parameter and this differs between projections. For each projection, we seek to select resolution parameters that give similar numbers of pixels to the spherical case, to have similar image fidelity and deg^2 per pixel. The projection results in a rectangular array of pixels defined by the resolution parameter. However, the sine and orthograpic maps are not rectangular. This results in the number of pixels on these maps being smaller than the total number of pixels produced by the rectangular array that the resolution parameter predicts. We select a resolution parameter equal to 2160 for the stereographic, orthographic, gnomonic and sine projections.

In order to ensure that the number of pixels for the projections closely matches the number of pixels for the sphere, the resolution was set to be equal to L for all projection methods, except the Mercator projection[4].

[4]The dimensions of the Mercator projection are defined differently, so we select an equivalent resolution as $R = \sqrt{N_{\text{sphere}}/0.7377}$ where N_{sphere} is the number of pixels in the spherical map, such that and the total number of pixels for the Mercator map is similar to the spherical case. This is because we define the dimensions of the Mercator projection array as $R \times 0.7377R$, that maps a declination range from $-7\pi/16$ to $7\pi/16$, selected to avoid major projection effects at the poles.

Smoothing and Pixelisation

The second Gaussian smoothing occurs when the convergence map κ is reconstructed from the shear map γ. This uses a default smoothing of 20 arcminutes based on the Full-Width Half-Maximum (FWHM), which converts to $\sigma = 2 \times 20.0 \times \pi/(60 \times 180 \times 2.355) \times \sigma_s$, where 2.355 is from the definition of the FWHM and σ_s is a multiplication factor introduced to allow greater ease when discussing adjustments to the smoothing. When the default smoothing based only on the FWHM is used, we set $\sigma_s = 1$ and this corresponds to a smoothing of 20 arcmin in real space, selected to match the smoothing used in Vikram et al. [2015]. However, it was found that when combined with the significant distortion from projections the smoothing had a distinct effect on the results, hence we selected $\sigma_s = 5$ as the 'default' when the smoothing is kept constant across projections while examining other parameters. This value allowed sufficient smoothing to reduce the effect of the noise, without blurring the underlying structure of the convergence map. Section 2.3 discusses the smoothing in further detail.

The projected maps do not loop around at the boundaries, so therefore the pixels at the edges of the map are not compared against the full 8 pixels they would neighbor on the sphere but instead only the pixels they neighbor in the planar projection. This would result in uncertainty over the validity of such a pixel being a peak, as it is not compared to all of the neighboring pixels as required by the definition of a peak we use. In order to avoid this uncertainty, we do not count any of the boundary pixels as peaks. The boundary pixels are neglected in calculations of the total area of each projection, but used for evaluating their neighboring pixels as peaks. The number of peaks on the boundary pixels is negligible compared to the number of non-boundary peaks due to the large overall number of pixels for each map compared to the number of pixels along each boundary. The number of boundary pixels scale $\propto L$, while the total number of pixels in the map scale $\propto L^2$, hence this effect is only prominent at small values of band-limit L.

The convergence maps differ in size and number of pixels due to the projection method and resolution selected. The application of masks will also decrease the number of pixels available for peak detection. As a result, the projection and masking

will have a significant effect on the peak counts that is not due to the distortion caused by the projection itself. To account for this and to evaluate the relative shapes of the peak count statistics, we normalise the peak counts by the number of pixels in each map. The projections are performed to produce maps with similar total numbers of pixels, and therefore similar resolution scales[5].

Smoothing scale for reconstruction

We used a smoothing parameter $s = 20$ arcmin $= 2 \times 20.0 \times \pi/(60 \times 180 \times 2.355) \times \sigma_s$ for both the peak counts and Minkowski functional analysis on the sphere. Due to the differences in resolution between the spherical case and projected cases the smoothing parameter needs to be adjusted for each projection to ensure that the degree of smoothing applied produces an equivalent mass map.

Applying masks

The presence of masking must be taken into account when analysing simulated data, in order to more accurately represent real data. In order to evaluate the effect of projection to the 2D plane on masked data, we used a simplified method of applying varying sized rectangular masks. The masks are defined on the sphere, such that the whole sphere is masked except for a circle centered on the defined centerpoint of the map with radius defined by the opening angle. The original mask on the sphere is projected with each of the five projection methods, and then applied to the corresponding projected shear map. The convergence reconstruction is applied after the masking. The projections apply a rotation such that the centre of the unmasked area is at the centre of the projection, and at the centre of the north hermisphere for the polar projections. It can be seen that the degree of distortion is more significant for the polar projections. As the shape distortion increases further from the centre,

[5] Additionally, the gnomonic projection does not cover the full sky and has maximum opening angle of $\theta = \pi/2$, $\pi/4$ on either side of the pole. Therefore it is necessary to scale the gnomonic projection peak counts by an appropriate factor to account for this. The surface area of sky covered by viewing angle $\frac{\pi}{4}$ from the pole is $(\sqrt{2}+2)\pi r^2$, and the surface area with full sky coverage, at viewing angle π, is $4\pi r^2$. Hence we take the ratio of area with $\frac{\pi}{4}$ opening angle to the full sky area to obtain the factor $(\sqrt{2}+2)/4$, which we divide the raw gnomonic peak counts by to scale to the full sky case. In the masked case, we still apply the projection to the full map and the resolution scale of the gnomonic projection still differs from the other polar projections, so the normalisation is still required.

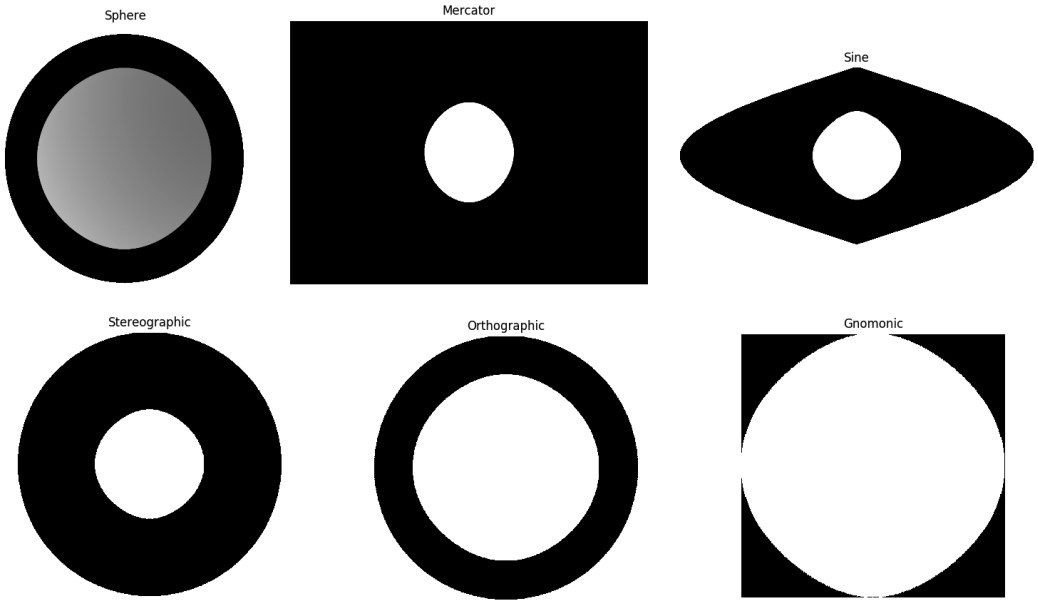

Figure 2.8: Example of the circular mask used in this chapter, using resolution L=1024. Black indicates the masked area and white indicates the unmasked area. In the case of the mask on the sphere, the 3D sphere is not projected but represented in 2D.

the unmasked area's shape is more greatly changed and this occurs at a different rate for different projections given the same initial mask on the sphere. Fig. 2.8 illustrates this mask on the sphere and on the projections.

2.4 Results

2.4.1 Peak counts

Full Sky Case

The normalised peak counts for the sphere and the projections are displayed in Fig. 2.9. These are the mean values across 20 realisations of randomly simulated shear maps and for maximum bandlimit $L = 2160$. The peak counts P_i have been normalised by dividing by the total area of sky covered by each projection, A_{sky}, and scaling by ratio of the number of pixels in each projection to the number of pixels in the spherical map, so the peak counts we see are $\frac{N_{\mathrm{MW}}}{N_i}\frac{P_i}{A_{sky}}$. Here, the subscript 'MW' is used to denote the spherical map which uses the pixelisation scheme from McEwen and Wiaux [2011b]. We can see that the five projection methods produce higher peak counts at low SNR and drop off more rapidly than the spherical case.

Given that the peak counts are normalised by the area of sky covered for peak identification, the projected peak counts are within one to two order of magnitude of the spherical peak counts. We display the results for three cases of smoothing, with smoothing scales $\sigma_s = 1,2,5$ for baseline smoothing of $\sigma_s \times 20$ arcminutes on the sky, and observe that greater smoothing brings the projected peak counts closer to the spherical case peak counts at low SNR thresholds. However, at high SNR thresholds the peak counts are significantly smaller with large errors due to the low number of peaks, so they are often not used for analysis due to unreliability. Additionally, the SNR thresholds close to SNR$= 0$ are dominated by noise and hence less reliable for analysis, hence the accuracy of peak counts at medium SNR thresholds are prioritised and we focus on these intermediate ranges when considering the similarity of projected and spherical peak counts. In our case, at low SNR thresholds none of the projections closely match the spherical case, although the gnomonic comes the closest. However, since low SNR thresholds are heavily noise-dominated and high SNR thresholds exhibit low peak count numbers, it is more appropriate to compare at moderate SNR thresholds, where we observe that the sine and orthographic projections are reasonably close to the spherical case. It must be noted that the gnomonic projection does not cover the full sky but only the areas up to 45° from the poles, and we accommodate this by scaling the peak counts

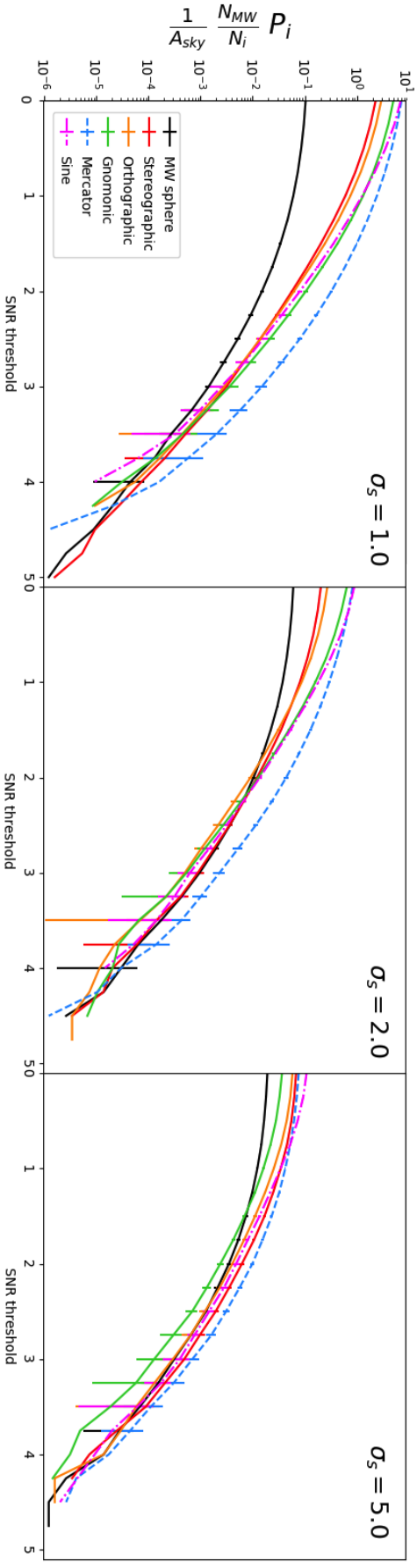

Figure 2.9: Peak counts divided by covered sky area as a function of SNR threshold for different projections on the full sky of 41253 deg^2. The displayed results are the mean of 20 realisations for each projection for the full sky case. We use bandlimit $L = 2160$ for the spherical case and corresponding resolutions for each projection. The peak counts are scaled to the area of sky covered and by the ratio of the number of pixels in each projection to the number of pixels on the sphere. The smoothing is $\sigma_s \times 20$ arcminutes on the sky, converted to $\sigma = 2 \times 20.0\sigma_s \times \pi/(60 \times 180 \times 2.355)$ in pixel space, where σ_s is the Gaussian smoothing scale factor. The three panels show three different Gaussian smoothing scales for the projected maps.

to the reduced area covered.

The ratio of the projected peak counts to the spherical peak counts is displayed in Fig. 2.10 for $\sigma_s = 5$. A smoothing scale of $\sigma_s = 5$ is used as it shows decreased divergence between the peak counts of each projection case while not being significant enough to obscure the structure of the convergence map. There is a consistent trend across all projections that at low SNR threshold the number of peaks is overestimated in comparison to the spherical case. In the threshold range between 1.5 and 3.0, the orthographic and sine projection peak counts are comparable to the spherical peak counts.

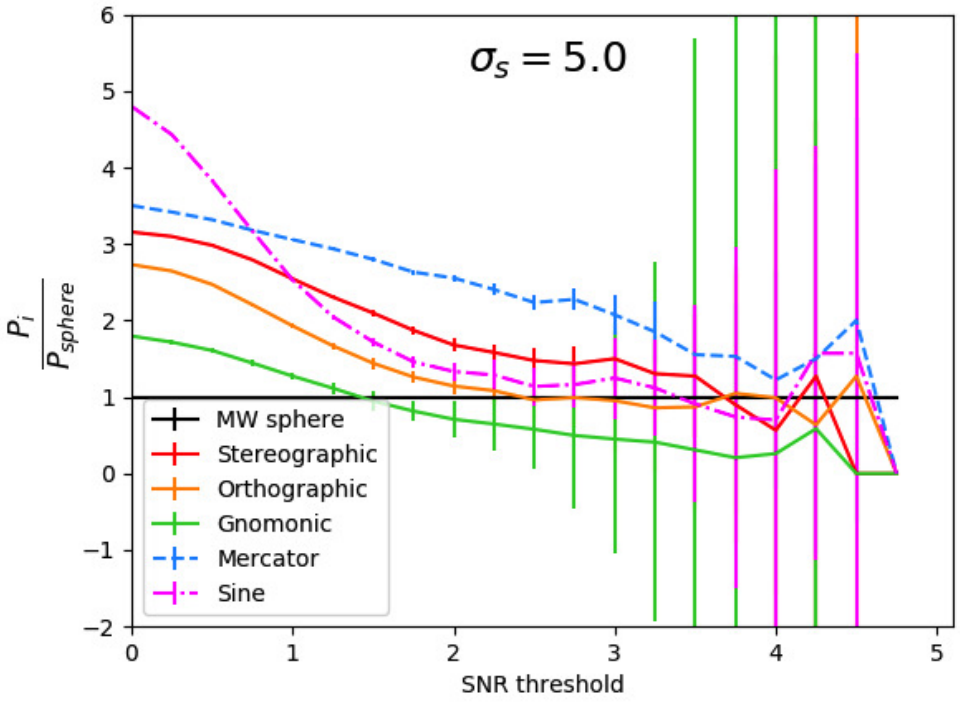

Figure 2.10: Ratios of the peak counts vs SNR thresholds for different projections to the peak counts of the sphere for the full sky case. The peak counts used are the mean of 20 realisations for the unmasked case with smoothing $\sigma_s = 5$, corresponding to a Gaussian smoothing factors of $\sigma_s \times 20$ arcminutes on the sky, and have been scaled to the area of sky covered.

The MW-sampled sphere produced by `ssht` is assumed to be a close approximation of the true underlying data on the celestial sphere. For the case with no masking, the gnomonic projection has the smallest overestimation of the peak count

at low SNR thresholds, and is preferred. However the gnomonic projection does not cover the full sky and only the area close to the centre of the projection is undistorted enough to be properly analysed, so it is possible that the extreme distortion far from the centre of projection results in lower peak counts. The peak counts at low SNR thresholds are likely to be dominated by Gaussian noise and cosmological analysis frequently requires detection of higher SNR threshold peaks, so projections that are closer to the spherical case at a middle SNR range, such as the orthographic and sine, are useful alternatives for peak count analysis; although performing the reconstruction on the sphere is preferable, as the results demonstrate.

Examination of the locations of detected peaks on the SNR maps finds that the most common cause for difference in peaks is how projections map features from the sphere to the plane. In cases where more than one pixel on the sphere are mapped to the same projected pixel, the method we used takes the average of these pixels as the value of the projected pixel. Different projection methods may map pixels in a manner such that a pixel that would be identified as a peak in one projection may have a lower value in relation to its neighbours in other projections and so therefore is not defined as a peak. In addition, features on the sphere are scaled differently on the plane for each projection, as can be seen in Fig. 2.7. This means that for a given area of analysis on the sphere, the corresponding area under analysis on the projected plane will vary in size between projections, leading to the detail being compressed on certain projections compared to others.

Partial Sky Case

We examine the partial sky case by finding peak counts for the full sky case and then applying masks of differing sizes, such that we throw away peaks located in the masked area and keep only the peaks in the unmasked area. We assume that boundary effects are negligible. The opening angles are defined as the total angle covered by the unmasked area defined in Section 1.2.8.

We can see the overall effect of increasing the unmasked area in Fig. 2.11, where the values are the peak counts normalised in the same way as for the full sky case. When examining the peak count as a function of increasing opening angle for selected SNR thresholds, we find that the peak count grows as a function of

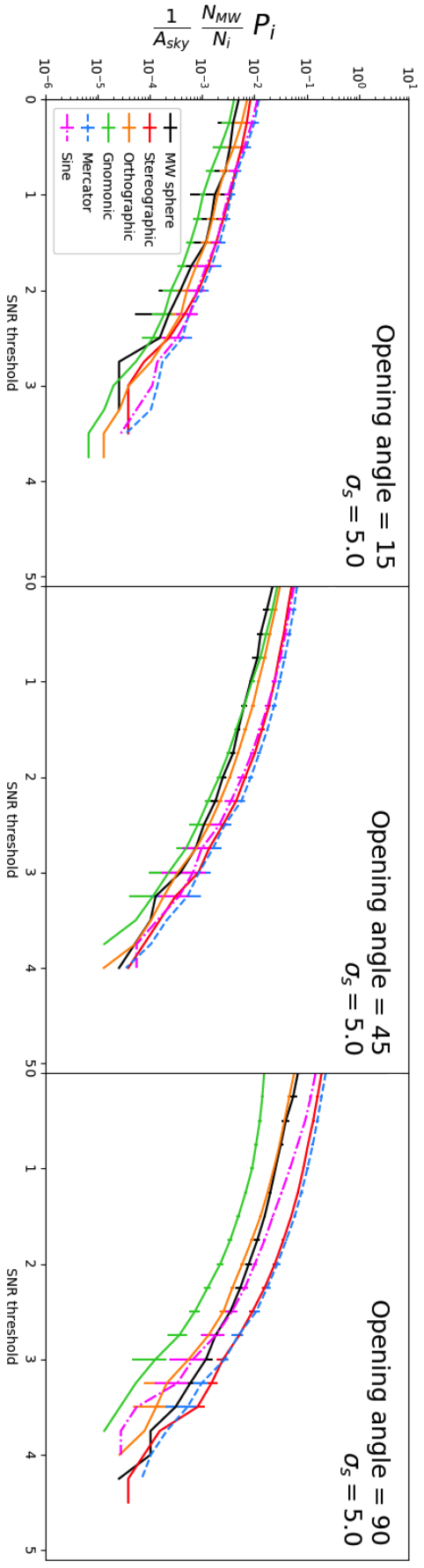

Figure 2.11: Peak counts divided by covered sky area as a function of SNR threshold for three cases of masked projections covering opening angles 15°, 45° and 90°. The displayed results are the mean of 20 realisations for each projection and use smoothing scale $\sigma_s = 5$ and bandlimit $L = 1260$ for the spherical case and corresponding resolutions for each projection. The peak counts are scaled to the area of sky covered and by the ratio of the number of pixels in each projection to the number of pixels on the sphere.

sky coverage at approximately the same rate for all projections and the spherical case. The projected peak counts do not converge exactly to the spherical case for any projection, but for certain opening angles and smoothing scales the peak counts of polar projections closely approach the spherical case for SNR thresholds between 1.5-3, which are the SNR thresholds of most interest for analysis. We observe a consistent pattern that the stereographic and Mercator peak counts remain greater than the other peak counts, while the orthographic and gnomonic peak counts are closer to the spherical case, for opening angles less than 45° in the gnomonic case. The sine projection, in contrast, diverges from the spherical case at smaller opening angles, but is closer to the spherical case at greater opening angles. However, the gnomonic projection is unsuitable for opening angles between 90° and 270°, as the gnomonic projection only applies to angles less than 45° which translates to a 90° opening angle.

2.4.2 Minkowski functionals

The Minkowski Functionals (MFs) described in equations 1.3.14, 1.3.15, 1.3.16 for the spherical case and the five projections for L=512 with sigma scale $\sigma_s = 1$ are displayed in Fig. 2.12 for the full sky case and 3 masked cases with opening angles 15°, 45° and 90°. We see that V_0 has the least difference between the spherical case and projected cases, while the MFs that incorporate the Dirac delta function and derivatives of the ${}_0\kappa$ maps – V_1 and V_2 – show a significant difference. This is primarily due to the Dirac delta function, which traces contours at a given threshold, that contributes most significantly to the differing values of the MFs. In maps with more noise, V_1 and V_2 are inflated due to false detections at the examined SNR thresholds. The resolution used also has a significant influence, as maps with a greater number of pixels resulted in lower values of V_1 and V_2. The projection method also affects the MFs through the presence of noise and distortion of shapes, which can be mitigated by using appropriate smoothing and high resolution. These factors heavily influence the contouring of the map, which impacts V_1 and V_2. However, we wish to identify and minimise other potential causes of the difference in MFs that are not due to the projected geometry, and we discuss this below. We find that V_0 is not significantly affected by the projection method, so subsequent analysis will focus on V_1 and V_2.

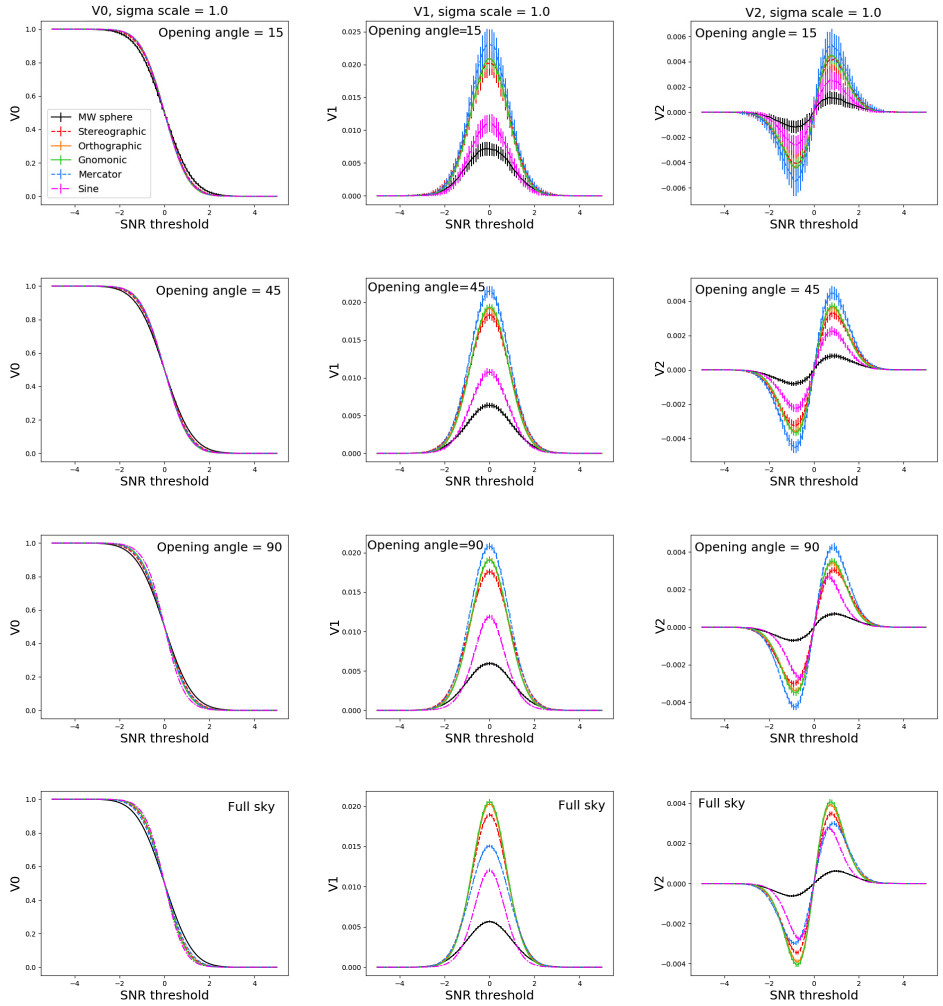

Figure 2.12: Minkowski Functionals of the 2D field V_0, V_1 and V_2, with smoothing using $\sigma_s = 1{,}5$ and opening angles 15°, 45° and 90° for masked cases and the full sky case, at L=512 and for 100 iterations.

As with the peak counts, the degree of smoothing significantly impacts the MFs V_1 and V_2. When the smoothing is not sufficient, significant noise may still be present in the SNR map which leads to amplified values for V_1 and V_2. We find that the presence of noise has a greater impact on the MFs V_1 and V_2 than the choice of projection. The projected maps have significantly greater noise than the map on the sphere due to how the smoothing is performed. We stress the importance of accounting for noise and using appropriate smoothing. Further discussion of the effect of smoothing is detailed in Section 2.3.

We expect to find that on small scales projection effects are minimised and the projected MFs will more closely match the spherical MFs. However, we find that the effects of pixelisation and smoothing have a significant impact on the MFs V_1 and V_2 for different projections for all opening angles of observed area. Using smaller opening angles leads to significantly greater error, as seen in Fig. 2.12, which is caused by the reduced number of pixels observed, hence pixelisation effects are more prominent. The effect of the number of pixels used to calculate MFs is significant enough to dominate over any distortion caused by projection. However, even with large errors it is still clear the manner in which projection affects the MFs on different scales. This can be mitigated by increasing the number of iterations or using greater resolution to achieve higher pixel count.

Variable smoothing for Minkowski functionals

One possible solution to this issue is to use projection-dependent smoothing i.e. applying a different smoothing scale for each projection in order to produce SNR maps that are more closely matched to the spherical case for small opening angles. The MFs measure the areas and contours of the map and not individual peaks, so increased smoothing does not remove significant information as it does with the peak counts. Under the assumption that there will be no projection effects on very small scales, we evaluate the maximum values of V_1 across a range of σ_s, as shown in Fig. 2.13, and for each projection we select a σ_s that corresponds to a value of V_1 closest to a selected V_1 maximum for the spherical case on small scales. The MF V_2 is slightly less affected by σ_s used than V_1, so we use V_1 to define the projection-dependent smoothing.

The MFs are significantly influenced by noise in a different manner to the peak counts because V_1 and V_2 measure the contours of a 2D map which are distorted by projection, hence the degree of smoothing must be carefully considered for the MFs and handled separately to smoothing for peak counts. We also know that the shapes and heights of the MFs are expected to be similar under ideal conditions, while this cannot be done for the peak counts as the peak count function is much more variable and does not have an underlying analytic form, hence it is risky to implement projection-dependent smoothing for the peak count statistic. Increasing smoothing tends to decrease the maximum value of V_1 and V_2 due to reduced noise, bringing several projection MFs closer to the MFs measured in the spherical case. Using smaller opening angles for observed area of sky increases in error on the MFs, but there is no significant difference in the mean of the shape of observed MFs V_1 and V_2 for low smoothing with $\sigma_s = 1$, since the projected map MFs are dominated by noise regardless of observed area.

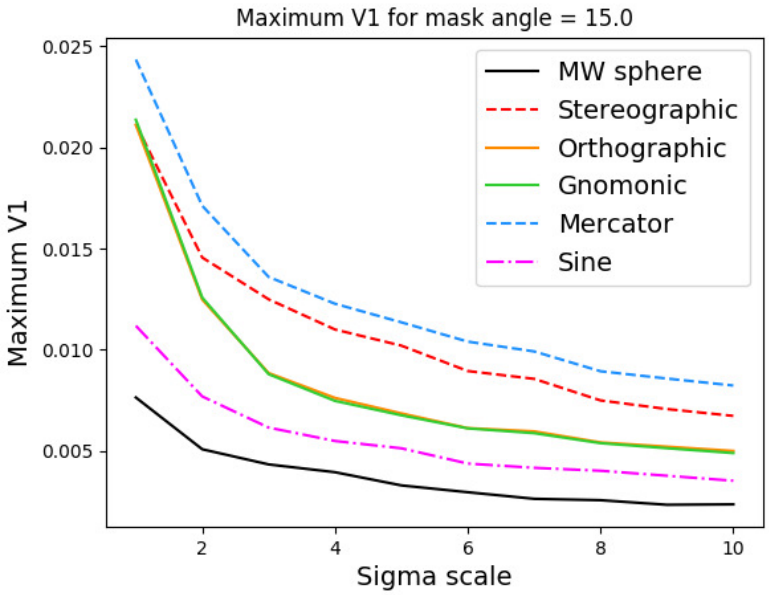

Figure 2.13: Maximum value of Minkowski Functional V_1 over a range of smoothing scales σ_s for window with opening angle 15° and 20 iterations, using a map with L=512.

In Fig. 2.13 we display the maximum value of the MF V_1 as a function of smoothing scaling parameter σ_s for the masked case with a window of opening

angle 15°. The maximum V_1 values decrease at a similar rate across the projections and spherical case, with little overlap other than the orthographic and gnomonic cases. While the maximum V_1 values consistently decrease, they eventually reach a plateau and do not converge even for high σ_s. A similar pattern is observed with the maximum and minimum values of V_2. This implies that even for high smoothing the spherical and projected MFs will not converge, hence there is an inherent difference in the MFs in each geometry after the noise is removed even for small opening angles. In the small area case, where we expect projection effects to be minimised, we still do not find convergence and this is suspected to be due to pixelisation effects due to lower relative resolution, assuming both the small angle and full sky case use the same maximum bandlimit.

We use Fig. 2.13 to identify an appropriate σ_s for each projection to match $\sigma_s = 1$ for the spherical case in order to perform projection-dependent smoothing. For this projection-dependent smoothing, we select the sphere smoothing as the standard $\sigma_s = 1$, and then use $\sigma_s = 10$ for the stereographic projection, $\sigma_s = 4$ for the orthographic projection, $\sigma_s = 4$ for the gnomonic projection, $\sigma_s = 8$ for the Mercator projection and $\sigma_s = 2$ for the sine projection.

The MFs obtained using projection-dependent smoothing are displayed in Fig. 2.14 for the masked case with opening angle 15° and the full-sky case. With the projection-dependent smoothing, the MFs of the full-sky case should more accurately reflect the influence of the projections not caused by noise. We see examples of this displayed in Fig. 2.14 for the masked case with opening angle 15° and for the full sky case. We observe that using projection-dependent smoothing causes the small-angle projected MFs to more closely align with the spherical case. However, in many cases the projected MFs, while matching the spherical case for small angles, are now reduced below the spherical MFs on larger angles. In the full-sky case, although it is not possible to separate the effect of increased smoothing from the influence of shape distortions from projection, using the assumption that the smoothing used produces equivalence for the MFs on small scales, the resulting MFs should approximately reflect the effect of each projection separated from the effects of noise. Since the MFs do not match the spherical case exactly, even with projection-dependent smoothing, analysis of each MF should be performed separately for each projection.

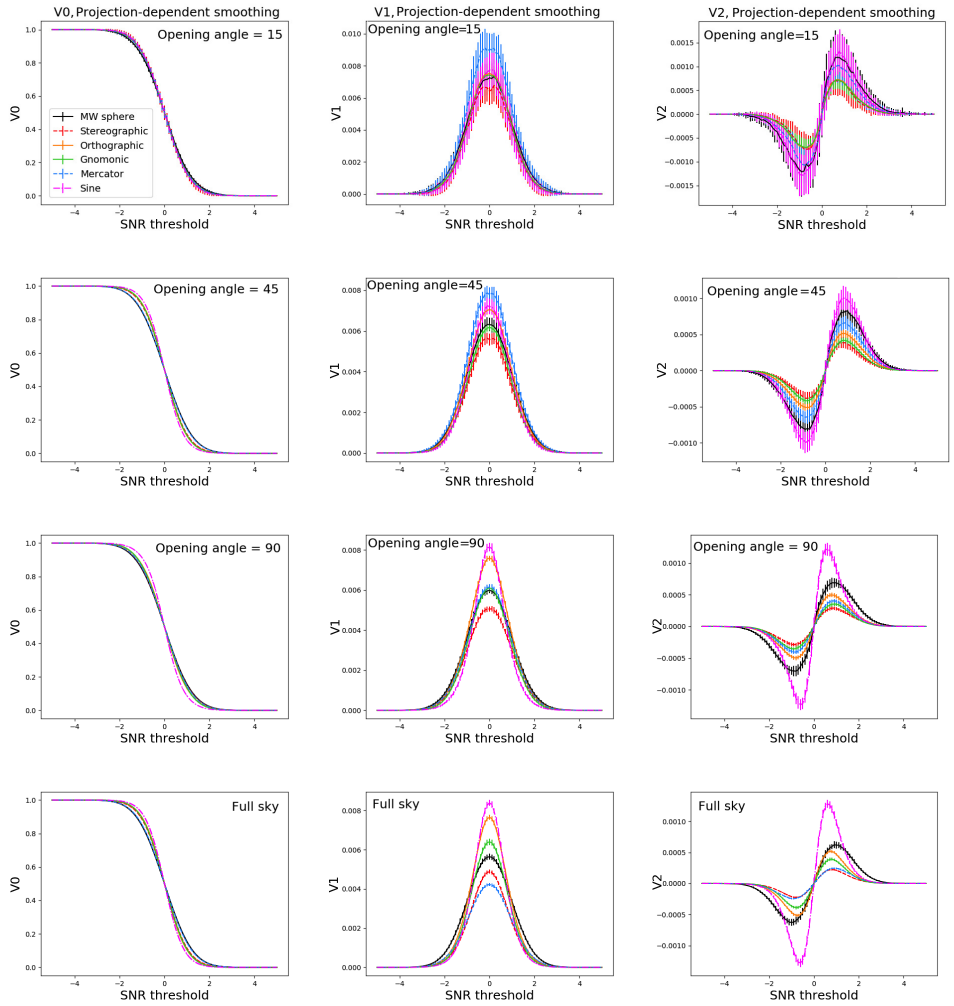

Figure 2.14: Minkowski Functionals of the 2D field V_0, V_1 and V_2, using projection-dependent smoothing for opening angles 15°, 45° and 90° for masked cases and the full sky case, at L=512 and for 100 iterations. We define smoothing scale for each case to be $\sigma_s = 1$ for the spherical case, $\sigma_s = 10$ for the stereographic projection, $\sigma_s = 4$ for the orthographic projection, $\sigma_s = 4$ for the gnomonic projection, $\sigma_s = 8$ for the mercator projection and $\sigma_s = 2$ for the sine projection

2.5 Conclusion

Whenever a planar approximation is made to the spherical celestial sphere a projection must be chosen. Here we investigate the effect of five different projections on the peak count statistic and Minkowski functionals of weak lensing convergence maps.

We use the software packages `SSHT` and `massmappy` to generate simulated recovered convergence maps. This is done using the following perscription; first we simulate shear maps on the sphere, project these shear maps to the plane, reconstruct the convergence maps natively on the plane, construct the SNR map from the convergence map, and identify peaks for a range of Signal-to-Noise Ratio (SNR) thresholds to obtain peak count statistics.

In the five examined projections (see Section 2.2.2) the peak counts derived from planar projected maps are greater than peak counts for the spherical case at low SNR thresholds and lower than the spherical case for high SNR thresholds; provided that the peak count numbers are adjusted for the differing number of pixels in the map and area of sky covered. We find that all of the examined projections have drawbacks in comparison to peak counts evaluated on the sphere. The projected peak counts tend to have lower maximum for the SNR thresholds where peaks are detected than the spherical case. The orthographic projection produces peak counts that are most similar to the spherical case for high SNR thresholds when accounting for differences in pixelisation. While the peak counts from the orthographic and gnomonic projections most closely match the spherical case over the greatest range of SNR thresholds, the peak counts are still overestimated at low SNR thresholds and underestimated at high SNR thresholds. While increasing the smoothing and reducing observed area improves the peak count accuracy, the peak count statistics for the projected data cannot be made to match the peak count statistics for the data on the sphere at all SNR thresholds. Further smoothing to further reduce noise would result in the obscuration of real peaks, and a loss of signal. Thus we recommend that peak count analysis of large areas of sky be performed on the sphere if possible.

We also evaluated the Minkowski Functionals on the five projections in com-

parison to the spherical case. Assuming the same parameters used in the projections as the spherical case, we found large differences in V_1 and V_2 between the spherical case and the projected cases. This difference is primarily due to the greater noise in the maps reconstructed after projection caused by smoothing being applied unevenly (locally asymmetrical compared to the pixel coordinate system) on the projected map in comparison to the evenly applied smoothing on the sphere. This noise effect is significantly greater than other projection effects such as the distortion of shapes from the projection and must be accounted for when evaluating MFs on projections. One possible method of reducing the influence of noise is to apply projection-dependent smoothing, by establishing a smoothing scale for which the MFs match the spherical case on small areas of sky (where the influence of projection is minimised), and subsequently applying these smoothing scales to the projected data for larger areas.

While we find that the projected peak counts, and MFs, resemble the spherical values at small sky areas of sky coverage, as the sky coverage increases they diverge. Planar projections remain appropriate for analyses over small areas of sky, but for future experiments with greater sky coverage the approximations break down and we caution against using the planar projection for analysis and emphasise the necessity of moving towards analysis on the sphere. We must conclude that care must be taken when using projected MFs and peak statistics, and comparisons to simulated fields should be done in the same geometry as the observations.

CHAPTER 3

Pure mode E- and B-mode separation of weak lensing mass maps using scale-discretised spin wavelets

3.1 Introduction

Observations of cosmic shear, the weak lensing signal produced by large-scale structure matter perturbations along the line-of-sight, can provide useful insights into the nature of the Universe. Cosmic shear enables us to probe the underlying distribution of matter in the Universe and its evolution over time, allowing constraints to be placed on cosmological parameters [Refregier, 2003]. Cosmic shear can also be used to infer the total matter present in galaxy clusters [Broadhurst et al., 1995] and make convergence/mass maps of the total matter distribution of the large-scale structure (LSS). Mass maps are useful tools for probing cosmologically sensitive statistics [Bergé et al., 2010a; Pielorz et al., 2010a; Pires et al., 2010a; Takada and Jain, 2009b], for example mapping of the mass distribution in clusters [Taylor et al., 2004], measuring Minkowski functionals [Mecke et al., 1994b], measuring peak statistics [Lin and Kilbinger, 2015a,b] and cross-correlating the convergence maps with CMB lensing and galaxy clustering data [Delabrouille et al., 2018; Hu and Okamoto, 2002; Vikram et al., 2015].

There are a number of existing mass mapping approaches, including the Kaiser-Squires (KS) method [Kaiser and Squires, 1993], sparse reconstruction methods [Leonard et al., 2014; Price et al., 2018a,b,c], reconstruction through Bayesian modeling such as LensTool [Jullo et al., 2007], and mapping of cluster mass distributions [Broadhurst et al., 1995; Taylor, 2001]. Any use of convergence maps for subsequent analysis will require high precision and low contamination from systematic effects caused by the mass mapping algorithm itself.

Mass mapping algorithms attempt to reconstruct a scalar (spin-0) field from the observed spin-2 cosmic shear data. Because of its spin-2 nature the cosmic shear field can be decomposed into two scalar fields, a curl-free E-mode signal and a divergence-free B-mode signal. In the absence of systematic effects, the cosmic shear signal should only be comprised of an E-mode signal, with the presence of the B-mode signal frequently being used to identify systematic effects or probe the possibility of new physics [Barreiro et al., 1997; Barreiro and Hobson, 2001; Davis and Kibble, 2005; Durrer et al., 1999; Feeney et al., 2011; Hobson et al., 1999; Namikawa et al., 2012; Schneider et al., 2010].

One problem encountered in mass mapping is the issue of mode mixing (from E to B-mode, 'E-B mixing', and vice versa) caused by masking of the data; for masked data the E-B separation is not unique and ambiguous modes are introduced. Consequently, standard E-B reconstruction results in leakage between E- and B-modes, which leads to inaccurate reconstructions. Several analysis methods attempt to minimise the effect of this mode mixing, e.g. Hikage et al. [2011]. However, when evaluating weak lensing data on the full sky the geometry of this setting needs to be accounted for, which is exacerbated as the masks in weak lensing surveys can cover significant fractions of the sky. Dealing with mode mixing is also a persistent challenge in the field of CMB polarisation analysis, with similar attempts at a solution [Bunn and Wandelt, 2017; Smith and Zaldarriaga, 2007], many of which are also applicable to the weak lensing case.

There have been various attempts to deal with the problem of mode mixing, such as applying weights to the pure mode function, and apodisation of the mask to minimise ambiguous modes in order to obtain estimators for the power spectra or correlation functions of the E- and B-modes [Becker and Rozo, 2016; Chon et al., 2004; Hivon et al., 2002; Lewis et al., 2002; Pen et al., 2002; Schneider et al., 2010]. However it is also of interest to reconstruct clean E- and B-mode convergence maps directly in order to apply various methods of direct analysis to these convergence maps. The existing methods of reconstructing convergence maps from weak lensing data, and analogous methods of reconstructing the E- and B-mode maps from CMB data [Bowyer and Jaffe, 2011; Bowyer et al., 2011; Namikawa et al., 2012], typically do not attempt to remove the E-B leakage. Extensive work has been performed seeking to address this issue through the use of pure mode estimators [Bunn et al., 2003; F. Gruetjen and P. S. Shellard, 2012; Ferté et al., 2013; Lewis, 2003; Smith, 2006a; Smith and Zaldarriaga, 2007], as pure E-modes (B-modes) are orthogonal to all B-modes (E-modes). These mode pure estimators cancel ambiguous modes and can be further extended to using wavelets and direct reconstruction of the E- and B-mode maps [Leistedt et al., 2017].

Another factor to take into account in convergence map reconstruction is the geometry in which the mass mapping occurs, with most previous mode separation methods being performed on projections where the flat-sky approximation holds

[Van Waerbeke et al., 2013; Vikram et al., 2015]. Upcoming weak lensing surveys, including *Euclid*[1] [Laureijs et al., 2011], the Large Synoptic Survey Telescope [LSST Science Collaboration et al., 2009] and the Wide Field Infrared Survey Telescope [Spergel et al., 2013], will offer a greatly improved view of the Universe in both sky coverage and depth of field, aiming to cover almost the full sky. With this increased sky coverage it becomes necessary to account for the geometry of the sky (the celestial sphere), as projection methods are no longer adequate for accurately capturing mass map-derived statistics when observing data on the full sky [Vallis et al., 2018; Wallis et al., 2017]. Therefore methods of E-B separation must aim to evaluate the data in a spherical geometry, as we do in this chapter.

The extraction of E- and B-mode field maps using pseudo and pure harmonic-based [Bunn et al., 2003; Kim, 2011; Smith, 2006b] and wavelet-based [Leistedt et al., 2017] estimators has been established for the CMB, and it is our intent to apply these methods to the weak lensing shear signal for the first time. This previous work using the E-B separation on CMB maps displays the effectiveness of the additional terms in the pure estimator in canceling E-B leakage. We apply this method to cosmic shear data in the form of simulations of Gaussian random field based on the weak lensing spectrum C_l, including masking that approximates expected weak lensing observations from Euclid. Using the wavelet pure mode estimator, we will draw comparisons with both the harmonic pure mode estimator approach and the standard smoothed Kaiser-Squires method which uses only pseudo modes. The method we employ uses both harmonic and wavelet transforms to perform pure estimator E-B separation, with the wavelet pure estimator allowing greater precision in cancelling the E-B leakage by being applied on different scales separately. We display the residual maps for the E-modes and B-modes to draw comparison between the methods used, defining the residual maps as the difference maps between the masked true data and the masked reconstructions. In addition to these maps, the error maps are shown through using the standard deviation of each point on the map across the simulations generated. We give the ratio of the RMS values of the reconstructed convergence map to the true convergence map, and similarly the ratio of the RMS values of the residual maps to RMS of the reconstructed maps.

[1] http://euclid-ec.org

The power spectra of these reconstructed maps are displayed to illustrate how the reconstruction methods handle masking on different scales, comparing both the pure harmonic and wavelet methods to the smoothed KS method.

3.2 Background

Most of the relevant background information for this chapter are detailed in chapter 1, which will be referred back to. Any important concepts not covered previously will be introduced in this chapter. Details on the weak lensing formalism can be found in Section 1.2.3, with the Eq. 1.2.12 and Eq. 1.2.14 relating convergence κ and shear γ to the scalar lensing potential ϕ through the spin raising and spin lowering operators in real space and harmonic space respectively.

This chapter focuses on the accurate reconstruction of E-modes and B-modes from the shear signal, as detailed in Section 1.2.6. The spin-2 shear behaves akin to a polarisation field and can therefore be decomposed into a constituent spin-0 even-parity scalar E-mode field and an odd-parity pseudo-scalar B-mode field, equivalent to the curl-free and divergence-free gradient fields respectively [Kilbinger, 2015]. Weak lensing should only generate a scalar E-mode signal, with any observed B-mode signal arising from systematic effects. The lensing potential ψ can be written as the corresponding components $\psi = \phi^E + i\psi^B$, and the pure weak lensing signal is expected to produce $\psi^B = 0$. Refer to Eq. 1.2.23 for the definitions of the E-B modes in harmonic space, which will be used to construct estimators of the E- and B-mode fields in the spherical setting.

3.3 E-B mode separation methods

As detailed in Leistedt et al. [2017], E-B reconstruction by separation of E-modes and B-modes can be performed in either a (spherical) harmonic space or in wavelet space. Using the definition of the E- and B-modes following Eq. 1.2.23, analogous definitions can be constructed for the wavelet and harmonic cases. The following is used on the CMB in Leistedt et al. [2017] and adapted to the weak lensing case here.

3.3.1 The harmonic pure estimator

We use both the harmonic and wavelet transforms to reconstruct the convergence maps from the masked shear, to attempt to improve upon the limitations of the Kaiser-Squires method in the case of dealing with the masked full sky data. The KS estimator on the sphere as detailed in Eq. 1.2.39 is a harmonic pseudo estimator that does not account for the map. Here we extend this to form the pure estimator method.

In the case of the harmonic estimators, we use the harmonic transform to obtain the coefficients of the signal in harmonic space. The forward harmonic transform of function $f(\boldsymbol{n})$ to harmonic coefficients $f_{\ell m}$ is

$$f_{\ell m} = \int_{S^2} d\Omega(\boldsymbol{n}) f(\boldsymbol{n}) Y^*_{\ell m}(\boldsymbol{n}), \tag{3.3.1}$$

where $\boldsymbol{n}$ denotes the angles (θ, φ) on the sphere , $\mathrm{d}\Omega(\boldsymbol{n}) = \sin\theta \mathrm{d}\theta \mathrm{d}\varphi$ and $Y_{\ell m}(\boldsymbol{n})$ are the spherical harmonic functions. The inverse harmonic transform of the harmonic coefficients $f_{\ell m}$ to a function $f(\boldsymbol{n})$ performed on the sphere is given as

$$f(\boldsymbol{n}) = \sum_{\ell=0}^{\infty} \sum_{m=-\ell}^{\ell} f_{\ell m} Y_{\ell m}(\boldsymbol{n}). \tag{3.3.2}$$

We consider only the values of $\ell < L$, where L is the bandlimit set in the analysis.

In harmonic space, we can formulate the harmonic pseudo-estimator of the E- and B-modes, denoted as $\widetilde{E}^{\mathrm{harm}}$ and $\widetilde{B}^{\mathrm{harm}}$, as [Kim, 2011]

$$\begin{aligned} \widetilde{E}^{\mathrm{harm}}_{\ell m} &=_0 \mathcal{E}_{\ell m}, \\ \widetilde{B}^{\mathrm{harm}}_{\ell m} &=_0 \mathcal{B}_{\ell m}, \end{aligned} \tag{3.3.3}$$

where in general we define

$$
\begin{aligned}
{}_s\mathcal{E}_{\ell m} &= -\frac{1}{2}({}_s\widetilde{\gamma}_{\ell m} + {}_{-s}\widetilde{\gamma}_{\ell m}),\\
{}_s\mathcal{B}_{\ell m} &= \frac{\mathrm{i}}{2}({}_s\widetilde{\gamma}_{\ell m} + {}_{-s}\widetilde{\gamma}_{\ell m}),
\end{aligned}
\tag{3.3.4}
$$

where ${}_{\pm s}\widetilde{\gamma}_{\ell m}$ represent the harmonic transforms of the shear field multiplied by spin-0, spin-1 and spin-2 masks defined as

$$
{}_{\pm 2}\widetilde{\gamma}(\boldsymbol{n}) = {}_0\, M(\boldsymbol{n})\,{}_{\pm 2}\gamma(\boldsymbol{n}), \quad {}_{\pm 1}\widetilde{\gamma}(\boldsymbol{n}) = {}_{\mp 1}\, M(\boldsymbol{n})\,{}_{\pm 2}\gamma(\boldsymbol{n}), \quad {}_0\widetilde{\gamma}(\boldsymbol{n}) = {}_{\mp 2}\, M(\boldsymbol{n})\,{}_{\pm 2}\gamma(\boldsymbol{n}),
\tag{3.3.5}
$$

where the mask M and its derivatives using the spin-raising and spin-lowering operators (see Eq. 1.2.13) are denoted by

$$
{}_0M(\boldsymbol{n}) = M(\boldsymbol{n}), \quad {}_{\pm 1}M(\boldsymbol{n}) = \eth_{\pm} M(\boldsymbol{n}), \quad {}_{\pm 2}M(\boldsymbol{n}) = \eth^2_{\pm} M(\boldsymbol{n}).
\tag{3.3.6}
$$

The harmonic pseudo-estimator does not account for ambiguous modes caused by masking, leading to the leakage of the E- and B-modes. Hence, we extend Eq. 3.3.3 to the harmonic pure estimator by introducing additional terms to cancel out the ambiguous modes and reduce leakage with

$$
\begin{aligned}
\widetilde{E}^{\mathrm{harm}}_{\ell m} &= \quad {}_2\mathcal{E}_{\ell m} + 2N_{\ell,-2}N_{\ell,1}[{}_1\mathcal{E}_{\ell m}] + N_{\ell,-2}[{}_0\mathcal{E}_{\ell m}],\\
\widetilde{B}^{\mathrm{harm}}_{\ell m} &= \quad {}_2\mathcal{B}_{\ell m} + 2N_{\ell,-2}N_{\ell,1}[{}_1\mathcal{B}_{\ell m}] + N_{\ell,-2}[{}_0\mathcal{B}_{\ell m}],
\end{aligned}
\tag{3.3.7}
$$

where we make the assumption that the mask and derivatives vanish at the mask boundaries, thus satisfying the Dirichlet and Neumann boundary conditions. The Dirichlet boundary condition imposes a restriction on the value of the function at the boundary, while the Neumann boundary condition imposes a restriction on the derivative of the function at the boundary. For spin s the $N_{\ell,s}$ represents the factor

$$
N_{\ell,s} = \sqrt{\frac{(\ell+s)!}{(\ell-s)!}}.
\tag{3.3.8}
$$

As discussed in Leistedt et al. [2017], the power spectra of these estimators, $\widetilde{C}^E_\ell$ and $\widetilde{C}^B_\ell$, can be related to the power spectra of the true E- and B-modes on the full sky, C^E_ℓ and C^E_ℓ, using the coupling matrix $\widetilde{M}^{\pm}_{\ell\ell'}$, contains the angular power spectrum of the mask, denoted $W_{\ell''}$, through the following relation

$$\begin{pmatrix} \widetilde{C}_\ell^E \\ \widetilde{C}_\ell^B \end{pmatrix} = \sum_{\ell'} \begin{pmatrix} \widetilde{M}^+_{\ell\ell'} & \widetilde{M}^-_{\ell\ell'} \\ \widetilde{M}^-_{\ell\ell'} & \widetilde{M}^+_{\ell\ell'} \end{pmatrix} \begin{pmatrix} C_\ell^E \\ C_\ell^B \end{pmatrix}, \tag{3.3.9}$$

where

$$\widetilde{M}^\pm_{\ell\ell'} = \frac{2\ell'+1}{16\pi} \sum_{\ell''} (2l''+1) W_{\ell''} J_0^\pm(\ell,\ell',\ell''), \tag{3.3.10}$$

with

$$J_s^\pm(\ell,\ell',\ell'') = \begin{pmatrix} \ell & \ell' & \ell'' \\ s-2 & 2 & -s \end{pmatrix} \pm \begin{pmatrix} \ell & \ell' & \ell'' \\ 2-s & -2 & s \end{pmatrix}. \tag{3.3.11}$$

Using this relationship, one can obtain the E-modes and B-modes and their power spectra. The pseudo estimator method has mode mixing that is indicated by the off-diagonal elements $\widetilde{M}^-_{ll'}$. In order to fix this, the pure harmonic estimators given in Eq. 3.3.7 have additional terms that cancel the ambiguous modes and therefore remove the E-B mode leakage. The relationship of the power spectra of the true E- and B-modes and the power spectra of the pure estimators is the same as Eq. 3.3.9, but the coupling matrix is now

$$\begin{aligned} \widetilde{M}^\pm_{\ell\ell'} = \frac{2\ell'+1}{16\pi} \sum_{\ell''} (2\ell''+1) W_{\ell''} \big(& N_{\ell,-2} N_{\ell'',2} J_2^\pm(\ell,\ell',\ell'') \\ & + 2 N_{\ell,1} N_{\ell,-2} N_{\ell'',1} J_1^\pm(\ell,\ell',\ell'') + J_0^\pm(\ell,\ell',\ell'') \big), \end{aligned} \tag{3.3.12}$$

which cancels the ambiguous modes when the true E-modes and B-modes are recovered from the estimators.

3.3.2 The wavelet pseudo estimator

We use the wavelet pure estimator method used in Leistedt et al. [2017] for the CMB, adapted for weak lensing. We will start the discussion of the wavelet pure estimator by first covering the wavelet pseudo estimator. The use of scale-discretised wavelets allows the structure of the map to be preserved at each relevant angular scale, allowing extraction of greater detail than the harmonic method in the presence of masks. For the purpose of this analysis, a spin scale-discretised directional wavelet

is used; this allows for the localised capture of information in both real and harmonic space. Further details of the construction of these wavelets are given in McEwen et al. [2015], McEwen et al. [2018] and Leistedt et al. [2017].

Restating Eq. 1.4.5, the wavelet transform of function ${}_sf(\boldsymbol{n})$ with spin s is the convolution of ${}_sf(\boldsymbol{n})$ with the wavelet ${}_s\Psi^j(\boldsymbol{n})$ and a scaling function ${}_s\Phi(\boldsymbol{n})$ as follows

$$\begin{aligned} W_{sf}^{s\Psi^j}(\rho) &= \int_{S^2} d\Omega(\boldsymbol{n}) {}_sf(\boldsymbol{n}) [\mathcal{R}_\rho {}_s\Psi^j]^*(\boldsymbol{n}), \\ W_{sf}^{s\Phi}(\boldsymbol{n}') &= \int_{S^2} d\Omega(\boldsymbol{n}) {}_sf(\boldsymbol{n}) [\mathcal{R}_{\boldsymbol{n}'} {}_s\Phi]^*(\boldsymbol{n}), \end{aligned} \tag{3.3.13}$$

where $W_{sf}^{s\Psi^j}(\rho)$ denotes the wavelet coefficient of the wavelet ${}_s\Psi^j$ at a discrete scale $j = J_0, J_1, ..., J$, where J_0 and J are the minimum and maximum wavelet scales respectively, and $W_{sf}^{s\Phi}(\boldsymbol{n}')$ denotes the wavelet coefficient of the scaling function ${}_s\Phi$, which captures the information on the largest scale. The integration is defined over the surface of the sphere S^2 where $\mathrm{d}\Omega(\boldsymbol{n}) = \sin\theta \mathrm{d}\varphi \mathrm{d}\theta$. The rotation operators with domain on rotation group $SO(3)$ and on the sphere S^2 are denoted by $\mathcal{R}_\rho$ and $\mathcal{R}_{\boldsymbol{n}'}$ respectively, with $\boldsymbol{n} = (\theta, \varphi) \in S^2$ and $\rho \in SO(3)$ parameterised by the Euler angles (α, β, ξ).

Similarly, restating Eq. 1.4.6 here, the inverse wavlet transform is used to reconstruct the original function ${}_sf(\boldsymbol{n})$ from the wavelet and scaling function and the corresponding coefficients as

$$\begin{aligned} {}_sf(\boldsymbol{n}) &= \int_{S^2} d\Omega(\boldsymbol{n}') W_{sf}^{s\Phi}(\boldsymbol{n}') [\mathcal{R}_{\boldsymbol{n}'} {}_s\Phi](\boldsymbol{n}), \\ &+ \sum_{j=J_0}^{J} \int_{SO(3)} d\mu(\rho) W_{sf}^{s\Psi^j}(\rho) [\mathcal{R}_\rho {}_s\Psi^j](\boldsymbol{n}), \end{aligned} \tag{3.3.14}$$

where $\mathrm{d}\mu(\rho) = \sin\beta \mathrm{d}\alpha \mathrm{d}\beta \mathrm{d}\xi$ denotes integration over the Euler angles. The maximum wavelet scale J is defined as $\lceil \log_\lambda(L-1) \rceil$, where λ is the wavelet scaling factor, and the minimum wavelet scale J_0 can be freely selected provided that the scaling function ${}_s\Phi(\boldsymbol{n})$ covers the signal at low ℓ-mode. Further information on the construction of spin scale-discretised wavelets is found in McEwen et al. [2015]; McEwen et al. [2018].

For the transform to be invertible, the harmonic coefficients of the wavelets

${}_s\Psi^j(\boldsymbol{n})$ and scaling function ${}_s\Phi(\boldsymbol{n})$ must fulfil the wavelet conditions in Eq. 1.4.7.

From these preliminaries we can now obtain the E-mode $\widetilde{W}_\epsilon^{0\,\Psi^j}(\rho)$ and B-mode $\widetilde{W}_\beta^{0\,\Psi^j}(\rho)$ wavelet pseudo-estimators, for a shear field ${}_{\pm2}\gamma$ as [Leistedt et al., 2017]

$$\begin{aligned}\widetilde{W}_\epsilon^{0\,\Psi^j}(\rho) &= -\mathrm{Re}\left[W_{{}_{\pm2}\widetilde{\gamma}}^{\pm2\,\Psi^j}(\rho)\right],\\ \widetilde{W}_\beta^{0\,\Psi^j}(\rho) &= \mp\mathrm{Im}\left[W_{{}_{\pm2}\widetilde{\gamma}}^{\pm2\,\Psi^j}(\rho)\right],\end{aligned} \tag{3.3.15}$$

where maps can be obtained via an inverse wavelet transform. ϵ and β in this case denote the E and B fields rescaled with $\epsilon_{\ell m} = N_{\ell,2}E_{\ell m}$ and $\beta_{\ell m} = N_{\ell,2}B_{\ell m}$ (where $E_{\ell m}$ and $B_{\ell m}$ are defined in Eq. 1.2.23, and $N_{\ell,2}$ in Eq. 3.3.8).

3.3.3 The wavelet pure estimator

Now we consider the pure mode estimator. In the presence of a mask, the mode leakage necessitates the addition of further terms to Eq. 3.3.15 to accommodate the E-B leakage.

Considering the scalar wavelet transform of the masked underlying E and B fields, which by definition are pure modes, and performing integration by parts to move the action of the spin raising/lowering operator to a masked wavelet, we recover

$$\begin{aligned}W_\epsilon^{0\,\Psi^j}(\rho) &= -\mathrm{Re}\int_{S^2} d\Omega(\boldsymbol{n})\,{}_{\pm2}\gamma(\boldsymbol{n})\eth_\mp^2\left[M(\boldsymbol{n})(\mathcal{R}_{\rho0}\Psi^j)(\boldsymbol{n})\right],\\ W_\beta^{0\,\Psi^j}(\rho) &= \mathrm{Im}\int_{S^2} d\Omega(\boldsymbol{n})\,{}_{\pm2}\gamma(\boldsymbol{n})\eth_\mp^2\left[M(\boldsymbol{n})(\mathcal{R}_{\rho0}\Psi^j)(\boldsymbol{n})\right],\end{aligned} \tag{3.3.16}$$

where the masked term can be expanded to

$$\begin{aligned}&\eth_\pm^2\left[M(\boldsymbol{n})(\mathcal{R}_{\rho0}\Psi^j)(\boldsymbol{n})\right] =\\ &{}_0M(\boldsymbol{n})(\mathcal{R}_{\rho\pm2}\mathrm{Y}^j)(\boldsymbol{n}) + 2{}_{\pm1}M(\boldsymbol{n})(\mathcal{R}_{\rho\pm1}\mathrm{Y}^j)(\boldsymbol{n}) +{}_{\pm2}M(\boldsymbol{n})(\mathcal{R}_{\rho0}\mathrm{Y}^j)(\boldsymbol{n}),\end{aligned} \tag{3.3.17}$$

where ${}_{\pm s}\mathrm{Y}^j(\boldsymbol{n}) = \eth_\pm^s[{}_0\Psi^j(\boldsymbol{n})]$. In harmonic space

$${}_2\Psi^j = \frac{{}_{\pm2}\mathrm{Y}^j_{\ell m}}{N_{\ell,2}} = \frac{{}_{\pm1}\mathrm{Y}^j_{\ell m}}{N_{\ell,1}} ={}_0\,\mathrm{Y}^j_{\ell m}. \tag{3.3.18}$$

From this, the wavelet pure estimators can be written in a compact form as

$$\begin{aligned}\hat{W}_{\epsilon}^{0\,\Psi^j}(\rho) = &\quad -\mathrm{Re}\Big[W_{\pm2\widetilde{\gamma}}^{\pm2\,\mathrm{Y}^j}(\rho) + 2W_{\pm1\widetilde{\gamma}}^{\pm1\,\mathrm{Y}^j}(\rho) + W_{0\widetilde{\gamma}}^{0\,\mathrm{Y}^j}(\rho)\Big],\\ \hat{W}_{\beta}^{0\,\Psi^j}(\rho) = &\quad \mp\mathrm{Im}\Big[W_{\pm2\widetilde{\gamma}}^{\pm2\,\mathrm{Y}^j}(\rho) + 2W_{\pm1\widetilde{\gamma}}^{\pm1\,\mathrm{Y}^j}(\rho) + W_{0\widetilde{\gamma}}^{0\,\mathrm{Y}^j}(\rho)\Big],\end{aligned} \tag{3.3.19}$$

where

$$W_{\pm s\widetilde{\gamma}}^{s\,\mathrm{Y}^j}(\rho) = \int_{S^2} d\Omega(\boldsymbol{n})\,{}_{\pm s}\widetilde{\gamma}(\boldsymbol{n})[\mathcal{R}_{\rho s}\mathrm{Y}^j]^*(\boldsymbol{n}), \tag{3.3.20}$$

and ${}_{\pm s}\widetilde{\gamma}(\boldsymbol{n})$ are defined in Eq. 3.3.5.

Similarly to the harmonic pure estimator, the first term in Eq. 3.3.19 behaves as the pseudo-estimator while the additional two terms cancel the ambiguous modes to minimise E-B leakage. From these pure estimator wavelet coefficients, one can use the inverse wavelet transform to reconstruct the E- and B-mode maps.

An advantage of a wavelet analysis is the ability to apply the mask at each angular scale discretely, taking advantage of the localisation of wavelets in both real and harmonic space. Additionally, the use of directional wavelets allows the mask to be applied at different orientations examined by the wavelets. From the original mask M a set of masks, that are both scale-dependent and orientation-dependent, denoted $M^{jn}(\boldsymbol{n}) = M^j(\varphi,\theta,\xi_n)$, can be derived where M^j are the scale-dependent masks over the range $J_0 < j < J$ and ξ_n denotes the orientation of the wavelet coefficients over range $\xi_1,...,\xi_N$, where N is the number of directions probed. The equations remain the same, with $M^{jn}(\boldsymbol{n})$ replacing $M(\boldsymbol{n})$ and the scale- and orientation-dependent masked $\widetilde{\gamma}^{jn}(\boldsymbol{n})$ replacing $\widetilde{\gamma}(\boldsymbol{n})$.

3.4 Method

We apply the previously outlined method to simulations, as this allows us to control the parameters generating the initial map, and to have access to the initial convergence map κ with which to compare the reconstructed convergence maps $\kappa_{\rm rec}$. We consider reconstruction by E-B separation using both the pure harmonic and wavelet techniques. The initial cosmic shear power spectrum $C_\ell^{\rm in}$ used to generate the simulated shear field uses `CosmoSIS` [Zuntz et al., 2015] with a ΛCDM [Ade et al., 2016b] cosmology in high redshift bin $1 < z < 2$ with a uniform number density distribution.

Over N iterations, a Gaussian random field shear map γ_i is generated using the `ebsep` code [Leistedt et al., 2017], with additional noise for $i = 1, \ldots, N$, a mask is applied to the shear map, and the three methods of reconstruction are applied: the pure harmonic E-B separation, the pure wavelet E-B separation and the smoothed Kaiser-Squires reconstruction (recalling the KS estimator is the harmonic pseudo estimator that ignores the mask). The mask we use is a simplified approximation of a *Euclid*-like mask [Laureijs et al., 2011] based on the mask used in Taylor et al. [2019], where we include a galactic plane cut and an ecliptic plane cut. In the wavelet case the mask is transformed into a set of scale-dependent masks applied to the map at each wavelet scale during reconstruction. Fig. 3.1 and Fig. 3.2 illustrate the application of the mask in angular space, and wavelet masks for each wavelet scale, where the angular mask is used as $M(\boldsymbol{n})$ and the wavelet masks on each scale are $M^{jn}(\boldsymbol{n})$, using $n = 1$ as we do not probe directionality in this case.

We select the relevant wavelets to have a scaling factor $\lambda = 2$, a minimum wavelet scale $J_{\rm min} = 5$, a maximum wavelet scale $J = 9$ and directionality of 1. These parameters are selected in order to give a reasonable number of wavelet scales that can probe the a reasonable number of scales that cover the relevant shape information of the data map and mask. As can be seen in Fig. 3.2, these parameters analyse 5 different scales, in addition to the scaling function, that cover the full range of detail for the mask and hence the data map. The directionality is set to be 1 as while probing the directional features of the spin-2 shear data is of value, the key aim of this chapter is to examine the basic performance of the wavelet

Figure 3.1: Angular simulated *Euclid*-like [Laureijs et al., 2011] mask. The map is displayed at maximum bandlimit $L = 512$, and therefore has dimensions of 512×1023 using MW-sampled pixels.

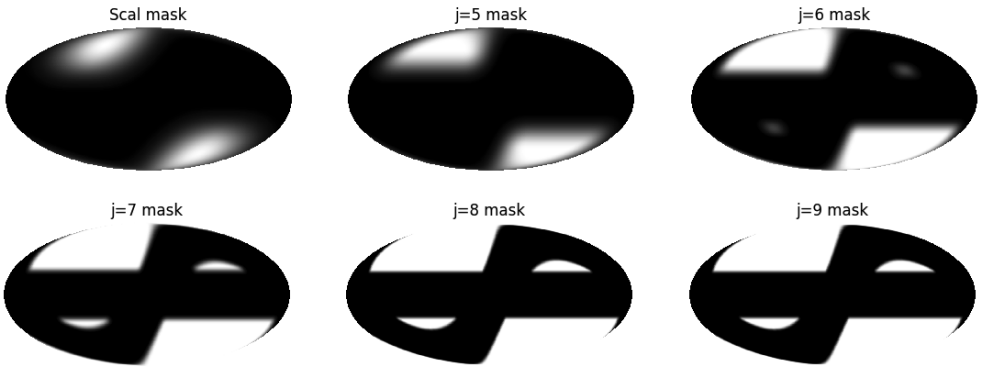

Figure 3.2: Wavelet form of the simulated *Euclid*-like [Laureijs et al., 2011] mask used in wavelet E-B separation, separated by wavelet scale j. Maps displayed with dimensions 512×1023 using MW-sampled pixels, set by maximum bandlimit $L = 512$, and wavelet scaling factor $\lambda = 2$, and therefore minimum wavelet scale $J_0 = 5$ and maximum wavelet scale $J = 9$.

pure estimator, hence it was decided to keep the directional properties simple. For each simulation, the E- and B-modes are reconstructed with the KS method, pure harmonic E-B separation method and pure wavelet E-B separation method. We evaluate the residual differences between the reconstructed convergence maps and the masked true convergence map, for each iteration. From each residual map power spectra are also calculated for each iteration. The reconstructed maps display a degree of leakage into the masked area, hence when calculating the residual maps and subsequent power spectra this leakage is neglected by removing the masked area from evaluation.

Due to the use of spin-2, spin-1 and spin-0 wavelet transforms in Eq. 3.3.19, we use the spin directional wavelets on the sphere [2]. However, we do not probe directionality for this study, hence we use axisymmetric wavelets, and set the directionality parameter to 1. The scale-discretised wavelets we use in harmonic space fulfill Eq. 1.4.7 and are detailed in McEwen et al. [2015]. For the simulated maps and subsequent reconstruction, we work in the sampling scheme in [McEwen and Wiaux, 2011a], where we select bandlimit $L = 512$.

The initial convergence map is generated in harmonic space from the input power spectrum C_ℓ^{in}, which is generated using `CosmoSIS` [Zuntz et al., 2015], and an initial Gaussian smoothing is applied to the $\kappa_{\ell m}$ with Full-Width Half-Maximum (FWHM) $\sigma = \frac{\pi}{10L}$. We transform this $\kappa_{\ell m}$ to real space and consider this the true convergence map. From $\kappa_{\ell m}$, we obtain the shear in harmonic space, $\gamma_{\ell m}$. Following this, both $\kappa_{\ell m}$ and $\gamma_{\ell m}$ undergo the inverse spherical harmonic transform to obtain the convergence ${}_0\kappa(\boldsymbol{n})$ and shear ${}_2\gamma(\boldsymbol{n})$ in real/angular space using the Kaiser-Squires equation as shown in Eq. 1.2.39. We opt to perform reconstruction without added noise, in order to evaluate the effect caused solely by leakage.

When considering the power spectra of the residual maps, we evaluate the KS reconstruction with smoothing applied during the reconstruction step, where the smoothing is $\sigma_s = \frac{20\times\pi}{60\times180\times2.355}$ and 2.355 is the Half-Width Half-Maximum conversion factor which corresponds to a smoothing size of 20 arcmin on the sphere, chosen to match Vikram et al. [2015] and Wallis et al. [2017]. We also evaluate the KS

[2] We use the code `S2LET` to perform the transform using the spin directional wavelets on the sphere. Details of these wavelets can be found in McEwen et al. [2015]

reconstruction without smoothing, to more closely match the E-B separation method which does not apply smoothing.

One final note is that while the resulting maps are displayed in the Mollweide projection (see Section 2.2.2), the analysis is all performed on the spherical setting and these projections are used solely to illustrate the results.

3.5 Results

In Fig. 3.3 we show the mean of the residual convergence maps over 100 realisations of the simulations, where the residuals for each reconstruction method are calculated by subtracting the reconstructed convergence map from the true convergence map with the corresponding masking method applied. The harmonic residual maps show clear differences on the largest scales, caused by the inability of the harmonic approach to cancel E-B leakage on these scales. The scale of the biases is approximately that of the largest masked areas. The wavelet approach shows a clear advantage over the harmonic approach with consistently smaller residuals and a lack of large-scale biases. This is due to the wavelet approach allowing correction of the E-B leakage on individual scales.

The most prominent difference between the KS and wavelet cases is the handling of the mask boundaries, resulting in distinctly lower residuals for the wavelet case in the regions at or close to the mask boundary. In the areas of the map far from the mask boundary we observe little difference between the KS and wavelet cases, but this effect is pronounced in the smaller unmasked regions, where the boundary effect is noticeable and significantly reduced in the wavelet case compared to the KS case. The KS reconstruction is also limited in the same manner that the harmonic is when compared with the wavelet method, being unable to probe the data on different scales and directions, and requires smoothing to account for the noise.

We note the size of the mean root-mean-square (RMS, see Eq. 1.3.5 in Section 1.3.1) values of the reconstructed convergence maps in comparison to the mean RMS of the true convergence maps as a measure of evaluating the size of the reconstructions in comparison to the original map. The same is shown for the ratio of the residuals to reconstructed maps, to demonstrate the relative size of the residual maps. The ratios are shown in Table. 3.1, where we observe that for the E-modes the reconstructed and residual ratios both show the pure wavelet estimator is superior to other the approaches used.

In Fig. 3.4, the wavelet residuals for the E-mode and B-mode maps are displayed on a smaller scale in order to show the details that cannot be distinguished on the scale of Fig. 3.3. It can be seen that there are some distinct errors with the wavelet

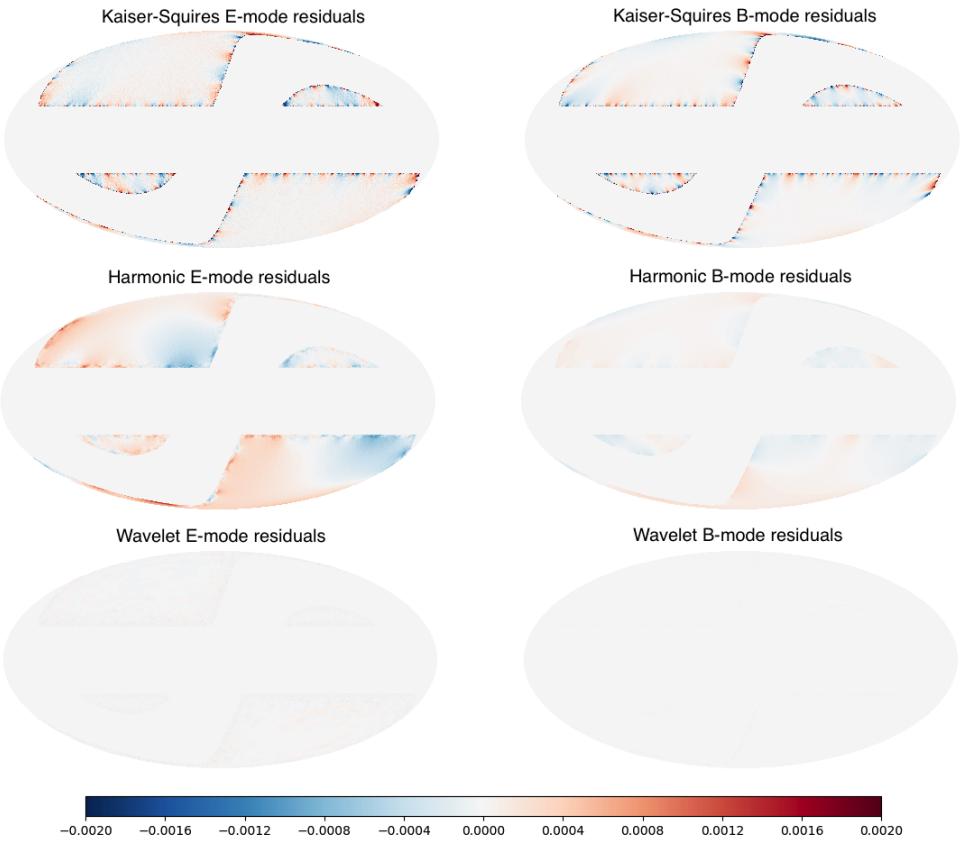

Figure 3.3: Maps of the E-mode and B-mode residuals for the smoothed KS reconstruction, pure harmonic E-B separation reconstruction and pure wavelet E-B separation reconstruction. These residuals are calculated as the mean of the true map with corresponding masking applied minus the reconstructed masked map over 100 realisations for maps with $L = 512$.

E-mode RMS ratio	Reconstruction	Residual
KS	0.9868	0.0966
Pure Harmonic	1.0836	0.3624
Pure Wavelet	1.0025	0.04425

Table 3.1: Table displaying the ratios of the mean RMS value of reconstructed convergence map to the mean RMS value of the true map, and of the RMS of the residual map to the RMS of the reconstructed convergence map, over $N = 100$ iterations for bandlimit $L = 512$. The RMS values for the reconstruction ratio are defined $\langle \kappa^2_{\text{rec}} \rangle^{\frac{1}{2}} / \langle \kappa^2_{\text{true}} \rangle^{\frac{1}{2}}$ and for the residual ratio as $\langle (\kappa_{\text{true}} - \kappa_{\text{rec}})^2 \rangle^{\frac{1}{2}} / \langle \kappa^2_{\text{rec}} \rangle^{\frac{1}{2}}$, where the relevant mask is applied to both κ maps. Ideal values are 1 and 0 respectively. Only the ratios for the E-modes are displayed, the B-mode ratios are not displayed as the generated convergence map has B-mode set to zero.

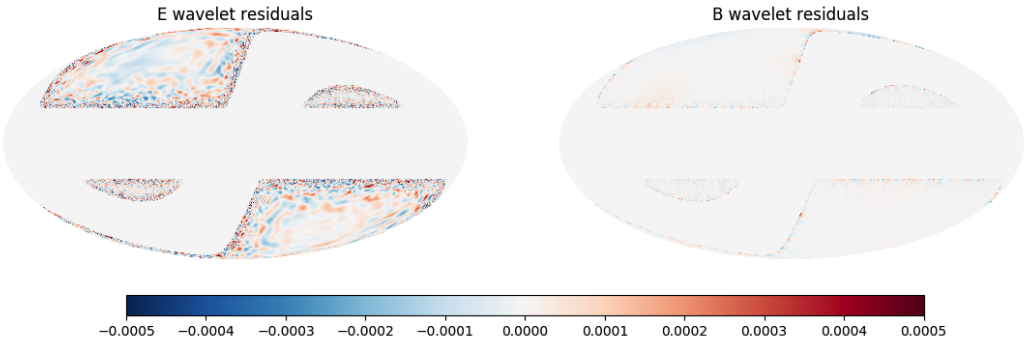

Figure 3.4: Maps of the E-mode and B-mode residuals over 100 iterations for maps with $L = 512$, for the pure wavelet E-B separation reconstruction, set on a different colour map scale to Fig. 3.3.

method, such as some slight apodisation at the mask boundaries, but these only become noticeable on scales much smaller than for the KS and harmonic pure cases. However this becomes more prominent in the work done in chapter 4, which is why here we illustrate the difference between the wavelet pure estimator reconstructed maps and the true maps.

Fig. 3.5 displays the standard deviation maps corresponding to each residual map computed across the 100 iterations. The KS error maps are relatively flat with slight increase at the mask boundary. The harmonic errors display a slight but noticeable increase along the boundaries of the mask in the E-mode case, which is

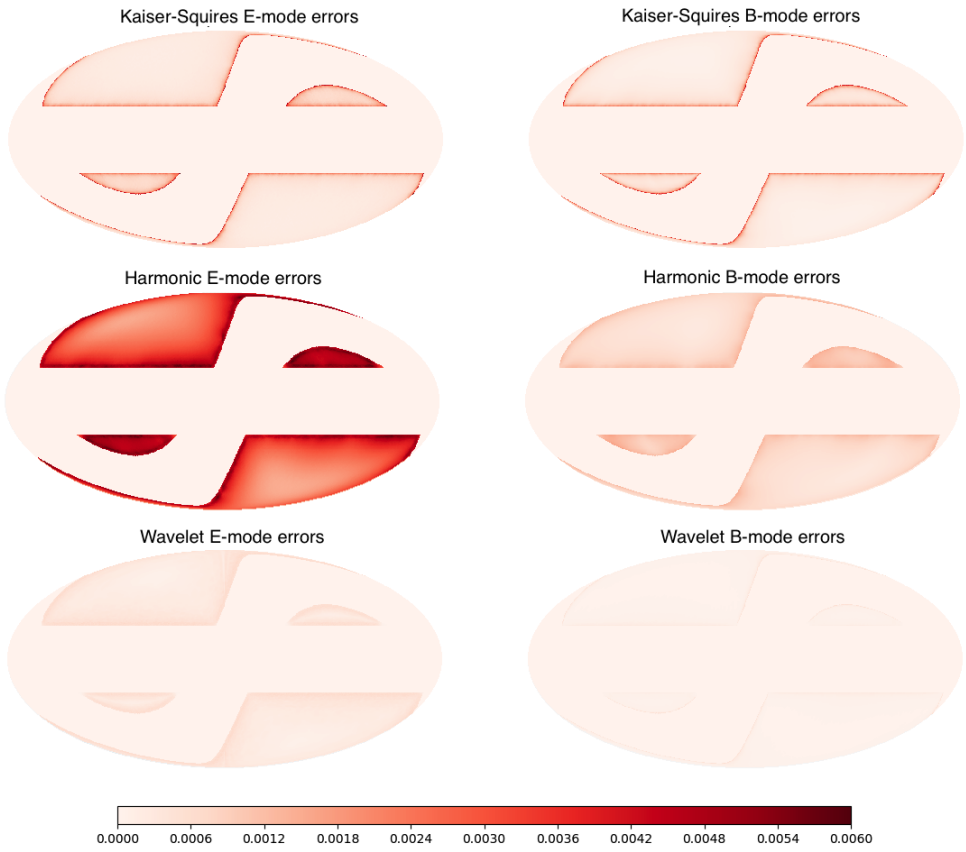

Figure 3.5: Maps of the standard deviation of the E-mode and B-mode residuals over 100 iterations for maps with $L = 512$, for the smoothed KS reconstruction, pure harmonic E-B separation reconstruction and pure wavelet E-B separation reconstruction.

avoided in the wavelet case due to scale-dependent masking allowing the detail at the boundary the mask to be more finely preserved.

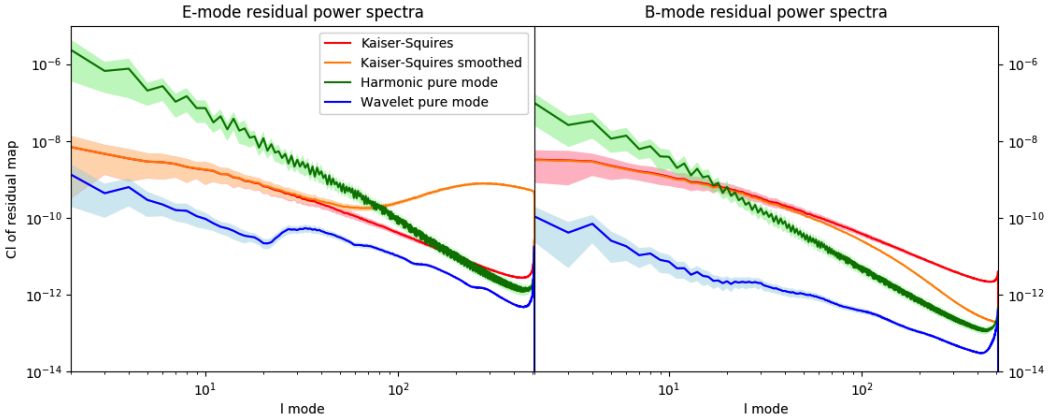

Figure 3.6: Power spectra of the residuals of the E-mode and B-mode reconstructions, displaying on which scales the power of the residuals is concentrated. Solid lines indicate the mean value across 100 iterations, and filled area denotes the standard deviation.

In Fig. 3.6 we display the angular power spectra of the residuals of the KS reconstructions, including both with and without additional smoothing during the reconstruction, and the pure mode reconstructions. This allows a measure of how the reconstruction method affects different scales. The weakness of the harmonic method to capture the large scale information is further demonstrated here, along with the wavelet method's distinct advantage at low and intermediate ℓ-modes.

At high ℓ-modes we observe that the power spectra of residuals of the pure E-B separated E-modes are consistently lower than the residual power spectra of the KS reconstruction method, with the wavelet case consistently producing the lowest residual power. For comparison, we also include the KS case with smoothing applied during the reconstruction step, where the smoothing is $\sigma_s = 20\frac{\pi}{60\times180\times2.355}$ and 2.355 is the Full-Width Half-Maximum, which corresponds to a smoothing size of 20 arcminutes on the sphere. It should be noted that the effect of smoothing on the KS residuals leads to distinctly different effects between the E-mode and B-mode residual power spectra, due to smoothing removing some of the information at high ℓ. This only applies at high ℓ-modes and is a consequence of the smoothing scale used rather than an indicator of the performance of the KS method itself. There is

a distinct difference between the power spectra of harmonic and wavelet methods on large scales, while they become more similar on smaller scales; this is expected as the masks considered for harmonic pure estimators are most effective for small scales.

3.6 Conclusion

One of the main contributors to errors in the field of convergence (mass) mapping are ambiguous modes introduced by masks. These ambiguous modes may contribute to either the E-mode or B-mode fields, causing E-B mixing and contaminating the pure E- and B-modes. Being able to isolate the E- and B-modes entirely would present an important new technique in the field of weak lensing analysis.

We use a pure mode wavelet-based method of separating the E- and B-modes through cancellation of ambiguous modes in wavelet space, previously evaluated on CMB simulations [Leistedt et al., 2017], and apply this to the weak lensing case. We compare E-B separation using harmonic and wavelet transforms, and compare both to the KS reconstruction method which is the standard convergence mapping method.

While the KS case performs better than the harmonic case on larger scales far from the mask boundary, the harmonic pure case performs better than the KS case on smaller scales, and the wavelet case shows an improvement over all scales. The primary cause of the difference between the harmonic and wavelet pure estimator cases is the use of scale-dependent masks used in the wavelet method, that allows the wavelet method to probe and mask each scale separately, leading to more accurate reconstructions. It can be clearly seen in both residual maps and power spectra of the residuals that the harmonic method results in distinct large scale residuals, and both the harmonic and KS cases display larger errors along the boundaries of the mask. This effect does not appear when using the wavelet method due to the ability to mask each evaluated scale independently.

One potential avenue for future analysis would be to make use of the directionality of the wavelets in order to capture directional information during reconstruction. Using different masking schemes, on both smaller and larger scales, could also provide insight into the comparative performance of different methods, given the differences in reconstructions on different scales.

Using wavelet-based E-B separation for mass mapping demonstrates a promising method for weak lensing analysis, as it shows a clear improvement over the KS reconstruction used previously, and pure harmonic E-B separation methods,

being able to more effectively cancel ambiguous modes at each scale. The pure wavelet-based method consistently performs better than the pure harmonic method at large scales and the KS method at all scales.

CHAPTER 4

The application of E-B pure mode separation using wavelets to DES Y1 data

4.1 Introduction

Of the many available observables for cosmological analysis, cosmic shear is a flexible and robust one, which provides many possible approaches to extracting cosmological information from it. Cosmic shear is the cumulative weak lensing effect of perturbations in the gravitational field caused by large-scale structure (LSS) in the Universe. The distribution of the LSS can be computed from cosmic shear observations, and by using galaxy redshift as an indicator of age of source galaxies this can be extended to studying the evolution of the LSS over time. This can be used to place constraints on cosmological parameters [Refregier, 2003], calculate or map the total matter content of galaxy clusters [Broadhurst et al., 1995; Taylor et al., 2004], and to directly construct maps of the convergence itself [Kaiser and Squires, 1993].

These convergence maps themselves provide a useful tool for cosmological research, as they trace the mass distribution of the Universe and can be used to probe certain cosmological parameters [Bergé et al., 2010a; Pielorz et al., 2010a; Pires et al., 2010a; Takada and Jain, 2009b]. Convergence maps are observed 2D fields with their own topological properties that can be used to probe non-Gaussian features of the cosmic shear, such as Minkowski functionals [Mecke et al., 1994b] and peak statistics [Lin and Kilbinger, 2015a,b]. Convergence map data can also be used to compliment other cosmological methods such as CMB lensing and galaxy clustering observations through cross-correlations [Delabrouille et al., 2018; Hu and Okamoto, 2002; Vikram et al., 2015].

The shear is a spin-2 signal that can be decomposed into a curl-free E-mode signal and a divergence-free B-mode signal. Weak lensing only produces an E-mode signal, hence a B-mode signal detected from the shear arises either from systematic effects during observation, or is a potential indicator of new physics [Barreiro et al., 1997; Barreiro and Hobson, 2001; Davis and Kibble, 2005; Durrer et al., 1999; Feeney et al., 2011; Hobson et al., 1999; Namikawa et al., 2012; Schneider et al., 2010].

Straightforward reconstructions of convergence maps can be done in a number of different ways, such as the harmonic transforms in the most commonly used Kaiser-Squires method [Kaiser and Squires, 1993], sparsity-based methods [Leonard

et al., 2014] and through the use of Bayesian modelling [Jullo et al., 2007]. The weak lensing signal is comparatively low signal-to-noise and susceptible to contamination from systematic effects, hence when performing reconstruction of the convergence maps from cosmic shear the method used should ideally be precise and aim to accommodate these problems. The major sources of contamination are noise (often dealt with through smoothing or sparsity-based methods), and mode mixing.

The presence of masks induces mode mixing through the introduction of ambiguous modes that cannot be clearly identified as either E-mode or B-mode. This mode mixing produces contamination of the E-mode and B-mode signals, leading to inaccurate results for both statistics derived from the shear signal and direct reconstruction of convergence maps. Methods for mitigating the effect of this mode mixing have been applied both to statistics such as the correlation function or power spectrum [Becker and Rozo, 2016; Chon et al., 2004; Hikage et al., 2011; Hivon et al., 2002; Lewis et al., 2002; Pen et al., 2002; Schneider et al., 2010] and CMB polarisation analysis [Bunn and Wandelt, 2017; Smith and Zaldarriaga, 2007]. Such methods typically do this through the application of weighting to reduce the ambiguous modes while separating the pure mode to obtain estimators for the E-mode and B-mode signals for reconstruction. The use of these pure estimators have been applied to successfully to the analogous CMB data [Bunn et al., 2003; F. Gruetjen and P. S. Shellard, 2012; Ferté et al., 2013; Kim, 2011; Leistedt et al., 2017; Lewis, 2003; Smith, 2006a,b; Smith and Zaldarriaga, 2007]. One extension to this pure mode estimator approach is to use scale-discretised wavelet transforms instead of harmonic transforms [Leistedt et al., 2017], that we applied to simulations of weak lensing data in chapter 3.

Masking arises from sky surveys containing incomplete or contaminated data, where unusable sections are removed from the map or weighted to zero. While future weak lensing surveys strive towards greater sky coverage with improved observation techniques to minimise sections of unusable data, it is improbable that an observed survey will be entirely without masking and current weak lensing surveys contain a wealth of cosmological information that should not be ignored, hence the importance of developing methods that can accurately account for the

mask. Upcoming wide field surveys (including *Euclid*[1] [Laureijs et al., 2011], the Large Synoptic Survey Telescope [LSST Science Collaboration et al., 2009] and the Wide Field Infrared Survey Telescope [Spergel et al., 2013]) cover large areas that require the curved sky geometry to be considered during the reconstruction, as the flat-sky approximations do not apply and projections to the plane are inadequate [Vallis et al., 2018; Wallis et al., 2017].

This chapter focuses on extending the work in chapter 3 to the application to real data. The aim in chapter 3 was to provide a measure of the accuracy of the reconstruction methods, made possible by using simulations that allowed access to the true convergence map that the shear is observed from. When working with real data, it is desired that the values derived from the observations are as similar as possible to the true values, hence the need for a high accuracy in the method, but the true underlying field in inaccessible. Referring to the comparison between the KS, harmonic pure mode and wavelet pure mode reconstruction methods done in chapter 3, the wavelet pure mode is expected to provide a reasonably accurate reconstruction of the convergence map comparable to, if not superior to, the KS case. We use the shear data from the DES Y1 data release [Abbott et al., 2018], which has sufficiently large sky coverage to necessitate using the curved sky reconstruction methods [Wallis et al., 2017]. Mass maps have been obtained for the DES Y1 observations in Chang et al. [2017] using the KS method applied to the curved sky setting, and it is our intention to provide a complementary analysis of the DES Y1 galaxy data using the wavelet pure mode estimator approach. In this chapter we will assess the topology and the extent to which the constructed fields are well approximated by a Gaussian field by measuring the Minkowski Functionals from the data.

This chapter will first detail the background of the research and outline the method used. As much of the background and science behind this chapter is shared with chapter 3, the background and method sections will refer back to previous sections where relevant while introducing any new concepts and equations relevant only to this chapter. The results will be divided into a discussion of the convergence maps themselves and a section on the various statistics derived from these convergence maps, including the Minkowski Functionals.

[1] http://euclid-ec.org

4.2 Background

The background on cosmic shear and its use in cosmology are detailed in chapter 1, with the key sections being Section 1.2.3. The projections used in this chapter are the Mollweide and stereographic projections, which are detailed further in Section 2.2.2. To summarise the relevant information, observations of galaxy ellipticities can be used to construct a map of the cosmic shear in the observed area. Cosmic shear is the weak lensing signal induced by the intervening matter between the observed galaxy and the observer. From this cosmic shear data, one can reconstruct the convergence map and in the process separate the E-modes and B-modes (see Section 1.2.6). These convergence maps trace the distribution of mass in the universe, including both visible matter and dark matter.

Weak lensing is expected to produce only an E-mode signal and B-mode signals are expected to arise from systematic effects, hence, once these systematic effects are accounted for, the study of the B-mode signal can provide insight into potential new physics. However, issues arise during the observation of the cosmic shear, most prominently in the form of masking. Masking occurs when the data cannot be obtained, is incomplete or unusable due to contamination, and therefore this part of the map is masked out. Masking leads to mode mixing and the creation of ambiguous modes that contaminate the reconstructed E-mode and B-mode fields. Therefore it is desirable to remove the consequences of masking and therefore mode mixing. Methods attempting to do so are detailed in Section 3.3, and in this chapter we focus on the use of the wavelet pure mode estimator as covered in Section 3.3.3 in chapter 3.

We also note that while the harmonic pure mode estimator is a possible alternative to the wavelet pure mode estimator for E-B separation, its performance is sub-par when compared to using wavelets. These drawbacks are outlined in chapter 3 and are why we opt to focus on only the KS method and the wavelet-based pure mode method.

DES Y1 data discussion

The Dark Energy Survey (DES) [Abbott et al., 2018] is an international large scale survey covering the southern hemisphere and gathering data from galaxies,

supernovae and other astronomical objects, from the beginning of its operation in 2013 to 2019. The purpose of DES is to provide accurate observations suited to analysis of dark energy through studies of supernovae, weak lensing [Chang et al., 2017], galaxy clustering [Elvin-Poole et al., 2018] and baryon acoustic oscillations, across a wide and deep field spanning a wide area of 5000 square degrees. DES has seen three releases of survey data, the Science Verification (SV) data release [Jarvis et al., 2016], the first public data release (DR1) [Abbott et al., 2018] and the year 1 data release (DES Y1) [Zuntz et al., 2018]. The DES Y1 data catalogue is the focus of this chapter as it contains weak lensing relevant data in the galaxy shapes, ellipticities and redshifts across a wide field of ~ 1500 square degrees. Mass maps have been produced of the DES Y1 data in Chang et al. [2017], performing harmonic KS reconstruction on the curved sky geometry and additionally providing cross-correlation of the mass maps to light distribution and evaluating the peaks and voids present in the mass maps. These mass maps have seen use in research of weak lensing ratios [Prat et al., 2018] and constraining cosmological parameters [Troxel et al., 2018].

We use the DES Y1 data downloaded from here `http://desdr-server.ncsa.illinois.edu/despublic/y1a1_files/shear_catalogs/`. From these catalogues we extract RA, dec, e1 and e2 the two coefficients of the elipticity of a galaxy, mcorr (the multiplicative bias correction), c1 and c2 (the additive bias corrections for e1 and e2), weight, and signal-to-noise. We also extract imerror and imflag that flag poor regions of the data. We use the `im3shape` DES Y1 catalogue, since this was also the one used in Chang et al. [2017]. For redshifts we use the Gold BPZ redshifts provided at the same address.

We make selections of this data based on Table I of [Jarvis et al., 2016], using the "conservative additive" cuts. This results in small additive systematic uncertainties, and it is hoped that moderate multiplicative systematic uncertainties are mitigated. For `im3shape`, this removes galaxies with signal-to-noise < 15. We also select all galaxies in the redshift range $0.6 < z < 1.2$, and remove any galaxies with imerror and imflag equal to zero.

To construct the ellipticity maps – from which the mass maps are constructed for each `HealPix` pixels we find all galaxies within the pixel and compute the

average like

$$\langle e_i \rangle_{\text{pix}} = \frac{\sum_{g \in \text{pix}} W_g (e_{1,g} - c_{i,g})}{\sum W_g (1 + m_g)} \tag{4.2.1}$$

where $i = (1,2)$, W_g is the weight, $e_{i,g}$ are the measured ellipticities of each galaxy, $c_{i,g}$ are the additive corrections, and m_g are the multiplicative corrections. This is the same approach taken in [Jarvis et al., 2016] and Chang et al. [2017]. In the following we will use γ and e interchangeably since we assume that $\langle e_i \rangle \approx \gamma_i$.

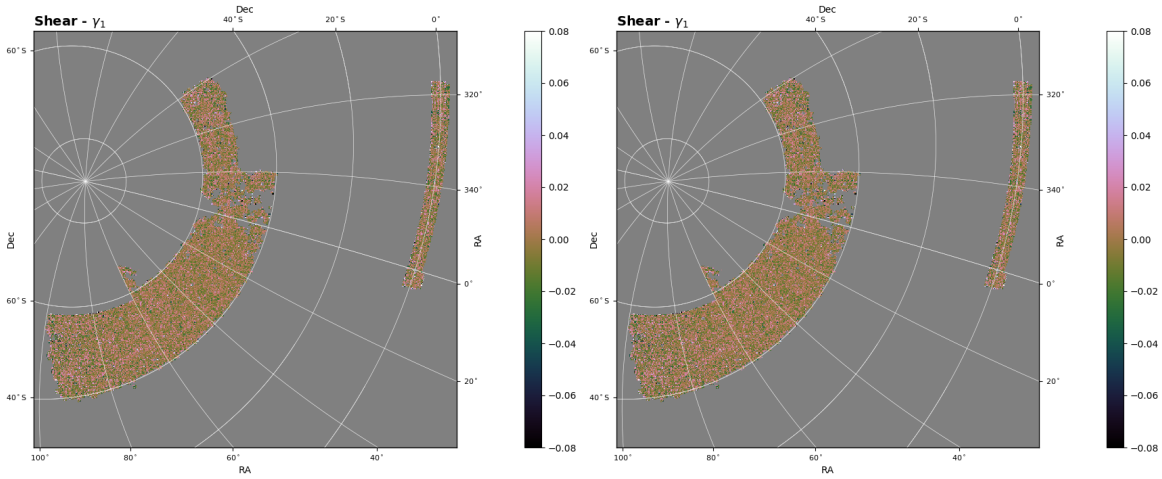

Figure 4.1: DES Y1 shear data displayed in MW pixelisation scheme for L=1024. Images have been zoomed in on the relevant region with the stereographic projection.

Both Fig. 4.1 and Fig. 4.2 display the DES Y1 shear data $\gamma = \gamma_1 + i\gamma_2$ converted to the MW pixelisation scheme used in this project. Fig. 4.2 illustrates the position of DES Y1 observations on the full sky; this wide field coverage of ~ 1500 square degrees is significant enough that the spherical geometry of they sky must be accounted for. The E-B separation and analysis will be performed natively on this curved spherical geometry, but for the purposes of illustrating our results in a straightforward manner we opt to display our reconstructions in the stereographic projection in the manner shown in Fig. 4.1.

Minkowski Functionals

In the interest of evaluating the Gaussianity of a 2D field, one may evaluate associated Minkowski Functionals, as given by Eq. 1.3.14, Eq. 1.3.15 and Eq. 1.3.16, and calculated as described in Section 2.2.4. As discussed in this earlier section, MFs can be used as a probe of the non-Gaussian information contained weak lensing

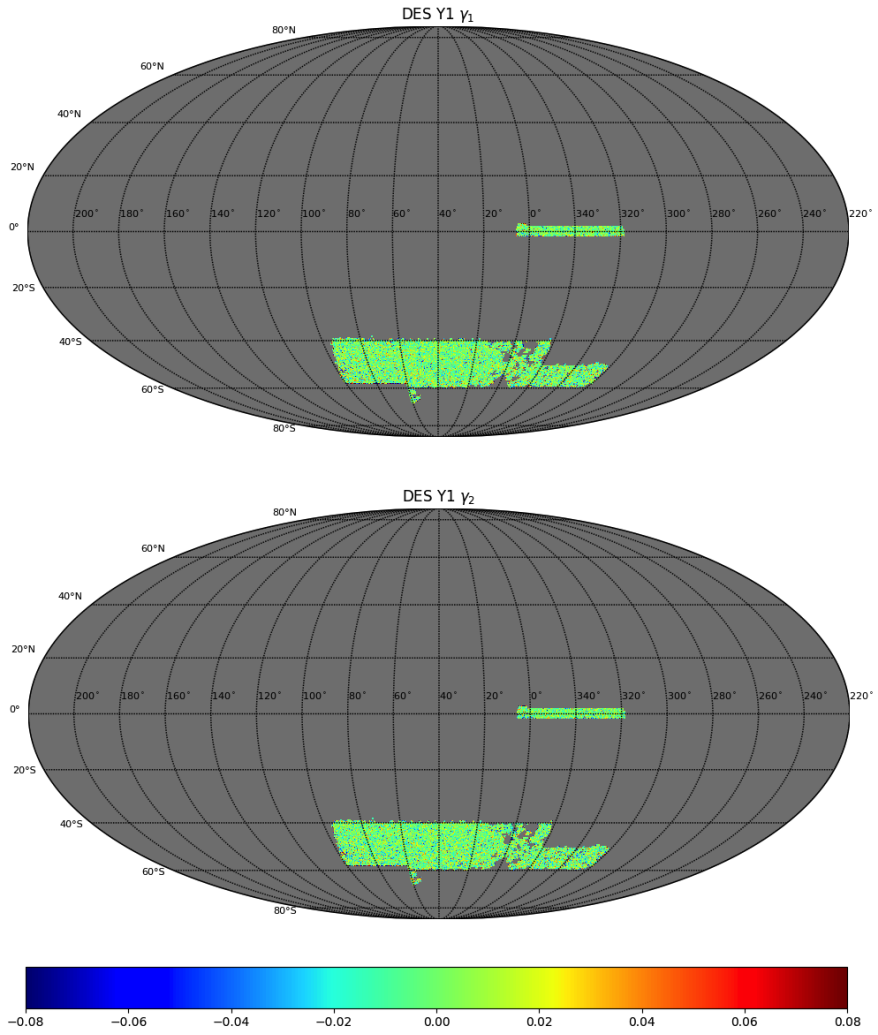

Figure 4.2: DES Y1 shear data displayed in MW pixelisation scheme for L=1024. Displayed on the full sky with Mollweide projection.

fields, with non-Gaussian features being more pronounced on smaller scales. The convergence field κ is converted to the signal-to-noise ratio (SNR) field ν, defined as $\nu = \frac{\kappa - \overline{\kappa}}{\sigma_\kappa}$. The MFs describe the topological features of the field as a function of given SNR threshold ν_0, where V_0 describes the area above the threshold, V_1 describes the boundary length at the threshold, and V_2 describes the Euler characteristic.

The analytic form of the MFs for a Gaussian random field is not given in Section 2.2.3, hence will be detailed here. The analytic form for the MF of a 2D field f is given as [Matsubara, 2003]

$$V_k(\nu_0) = \frac{1}{(2\pi)^{(k+1)/2}} \frac{\omega_2}{\omega_2 - k\omega_k} \left(\frac{\sigma_1}{\sqrt{2}\sigma} \right) e^{-\nu_0^2/2} v_k(\nu_0), \tag{4.2.2}$$

where $\nu = \frac{f-\overline{f}}{\sigma_0}$ is the SNR field of the field under consideration f, ν_0 denotes the SNR threshold across the examined range, $\sigma_0 = \langle f^2 \rangle^{\frac{1}{2}}$ and $\sigma_1 = \langle (\nabla f)^2 \rangle^{\frac{1}{2}}$, and $\omega_k = \frac{\pi^{k/2}}{\Gamma(k/2+1}$ denotes the volume of the unit ball in k dimensions, hence $\omega_0 = 1$, $\omega_1 = 2$, $\omega_2 = \pi$. For a Gaussian random field, Tomita's formula [Tomita, 1986] is used to define $v_k(\nu_0)$

$$v_k(\nu_0) = H_{k-1}(\nu), \tag{4.2.3}$$

where H_n denotes the Hermite polynomials,

$$H_n(\nu_0) = e^{\nu_0^2/2} \left(- \frac{d}{d\nu_0} \right)^n e^{-\nu_0/2}; \tag{4.2.4}$$

and for the instance of $k = 0$, we use

$$H_{-1}(\nu_0) = \sqrt{\frac{\pi}{2}} e^{\nu_0/2} \operatorname{erfc}\left(\frac{\nu}{\sqrt{2}} \right), \tag{4.2.5}$$

where $\operatorname{erfc}(x)$ denotes the complimentary error function. This will also allow us to compare the measured MFs with the expectation from a Gaussian random field.

4.3 Method

The reconstruction is performed using the code `EBsep` which implements the pseudo and pure E- and B-mode estimators as outlined in Section 3.3. In order to keep the evaluations consistent, we obtain the KS reconstructions with the same method as the wavelet pure estimators, including the method of smoothing. We focus on reconstruction using KS and the wavelet pure mode estimator, both with and without smoothing. The reconstructions are performed on the 2D surface of the 3D sphere as outlined in Section chapter 2.

Each galaxy from the catalogue is sorted into the pixel corresponding to its position on the sky. The shear map ${}_2\gamma = \gamma_1 + i\gamma_2$ is constructed with each pixel containing the mean of the component γ_1 and γ_2, for all galaxies falling within the pixel, as defined in Eq. (4.2.1). The reconstruction method is performed using the McEwen-Wiaux sampling scheme [McEwen and Wiaux, 2011b], hence the full sky map is constructed to fit the required parameters, having dimensions of $L \times (2L-1)$, where L is the bandlimit which governs both the pixelisation scheme and resolution of the map, and the maximum harmonic and wavelet modes used. The shear map is constructed on the full sky and the reconstruction is applied to the full map on the sphere, but the DES Y1 observational data is only obtained for a small section of the sky. The reconstruction method requires taking into account the full sky geometry and cannot be focused solely on this relevant area, hence it is necessary to maximise L as it determines the pixelisation resolution of the full sky map used. The bandlimit is selected to be $L = 1024$, giving high resolution for the reconstructed maps while keeping computation time reasonable, as increasing the bandlimit beyond $L = 1024$ provides diminishing returns to improvements to the quality of results.

The shear map is reconstructed through the KS method, as given on the sphere by Eq. 1.2.39, and the E-B separation via pure mode estimators, as given by Eq. 3.3.19. Further details for the method of reconstruction using the KS estimator are found in Section 1.2.10 and for the E-B mode separation Section 3.3.

The wavelet parameters used, as detailed in Section 1.4, are wavelet scaling factor $\lambda = 2$ and minimum wavelet scale $J_{min} = 5$, which for $L = 1024$ gives maximum wavelet scale $J_{max} = 10$. We do not use directional wavelets in this study, so the

directionality of the wavelets is set to 1 to use axisymmetric wavelets. In order to probe the possibility of using more wavelets for greater accuracy, we performed reconstructions with $B = 1.5$, however the differences did not prove significant enough to justify using the smaller wavelet scale factor.

Smoothing

In order to apply smoothing to reduce the impact of noise from the final reconstructions the signal is smoothed once before the reconstruction method is applied. The smoothing is applied by convolving the signal with the Gaussian kernel $G_\ell = e^{\ell^2\sigma_s^2}$, where σ_s is used to denote the smoothing factor. This smoothing factor is selected to correspond to the Half-Width at Half-Maximum of 20 arcmin as used by Vikram et al. [2015] and Wallis et al. [2017], hence $\sigma_s = \frac{2\times\pi}{60\times180\times2.355} \times 20$ arcmin. This smoothing is applied to the shear map before the reconstruction, to mitigate the effect of noise on the shear data. It would be possible to further smooth the data post-reconstruction, but this was found to be unnecessary as the initial smoothing step removed most of the influence of the noise.

Masking

The key purpose of using wavelet pure estimators over the standard KS is to accommodate the mask and the resulting mode mixing. In the previous project in chapter 3, it was necessary to approximate a mask appropriate for the simulated data. In this chapter we have access to observational data and we can construct the sky mask from the data itself. A pixel mask is constructed with same dimensions as the data map by simply evaluating at each pixel the presence or absence of galaxy data (where if the number of galaxies $N_{\mathrm{gal,pix}} < 1$ we label this as a masked pixel). The resulting pixel mask is displayed on the full sky in Fig. 4.3.

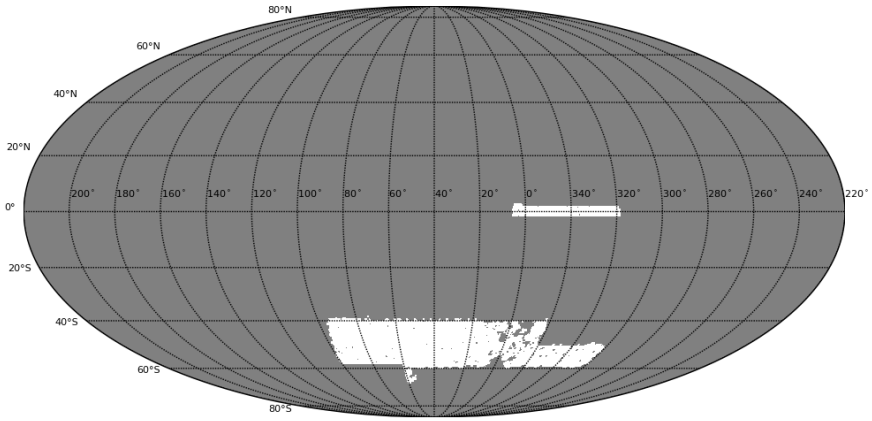

Figure 4.3: Pixel mask for the DES Y1 data as shown in Mollweide projection.

4.4 Results

4.4.1 Reconstructed convergence maps

In this section we display and discuss the convergence maps reconstructed from the DES Y1 shear data. Discussion of statistical analysis of these maps is found in Section 4.4.2. The convergence maps are displayed in the stereographic projection rotated to centre on the relevant area, but the E-B separation itself is performed on the sphere. Reconstruction both with and without smoothing are considered, but the noise contamination in the data necessitates smoothing and hence conclusions drawn from the smoothed data should be prioritised. While it is certainly possible to perform analysis on the unsmoothed data, it is heavily noise-dominated and this must be taken into consideration. The unsmoothed results are also examined for the purpose of comparison, but are to be considered less accurate due to the unaccounted for noise. The results are displayed with the observation mask applied over the convergence reconstructions to remove any leakage of the reconstructed data in the masked areas. Drawing comparison between prior mass mapping performed in Chang et al. [2017] and our mass maps obtained with the wavelet pure mode estimators, we observe that the same features of the convergence maps are present in both.

First we consider the unsmoothed case, as displayed in Fig. 4.4 and Fig. 4.5, for the KS method and wavelet pure estimator methods respectively. The most prominent difference between the two is this distinct apodisation effect at the mask boundary found in the wavelet case but not the KS case. The KS method does not consider the mask during the reconstruction, hence there is no apodisation at the mask boundaries, although not accommodating the mask introduces other problems in the reconstruction.. The resulting convergence map can be seen to be uninfluenced by the mask. In contrast, the purpose of the pure mode estimator is to remove the effect of mode mixing induced by the mask, hence the mask influences the reconstruction as shown. The difference between the reconstructions is more directly displayed in Fig. 4.6, which shows the difference between the two convergence maps at each pixel. Aside from the apodisation at the mask boundary, the two convergence maps display the same features, which are more evident in the

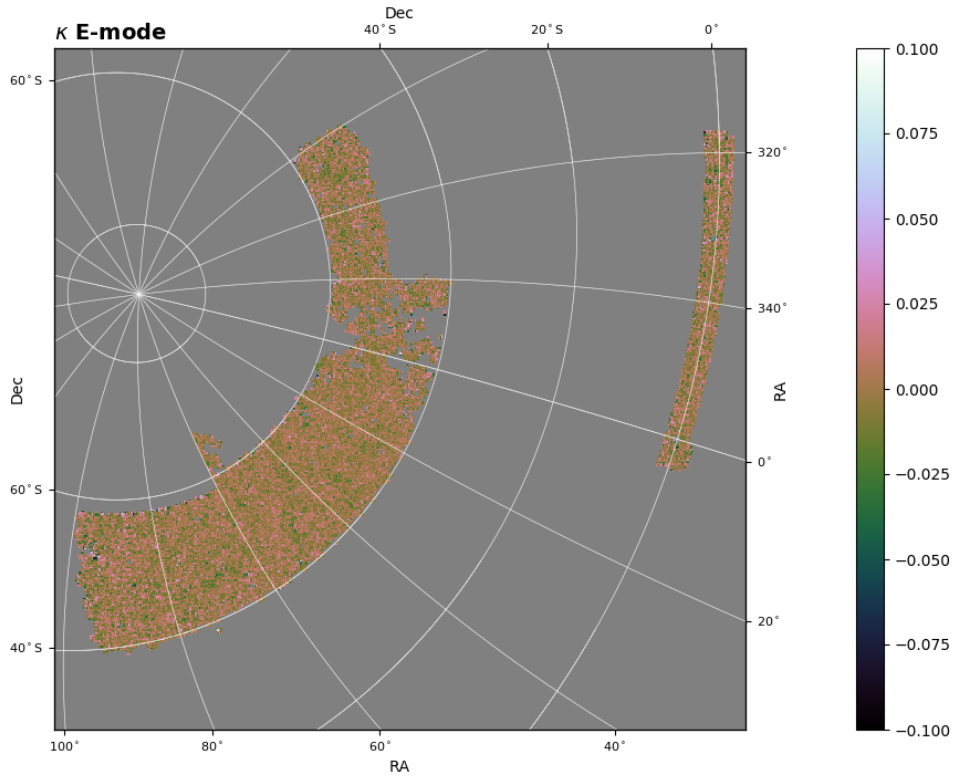

(a)

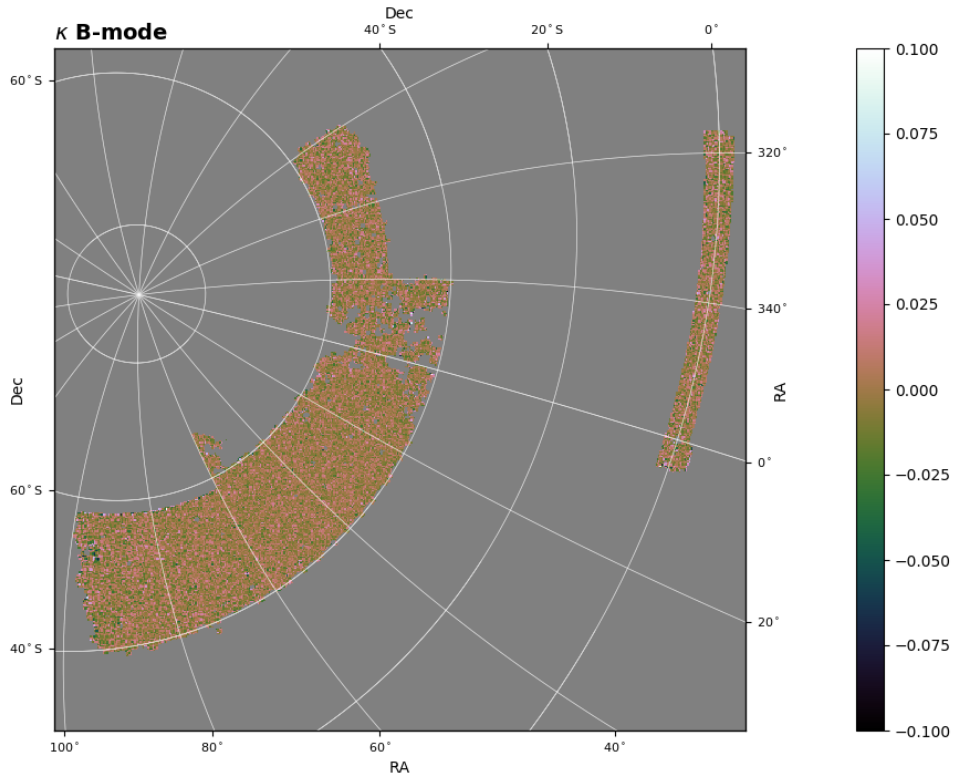

(b)

Figure 4.4: Reconstruction of convergence maps using the KS method from DES Y1 shear data. No smoothing is applied. Displayed in stereographic projection rotated to centre on the area shown.

subfloat[]

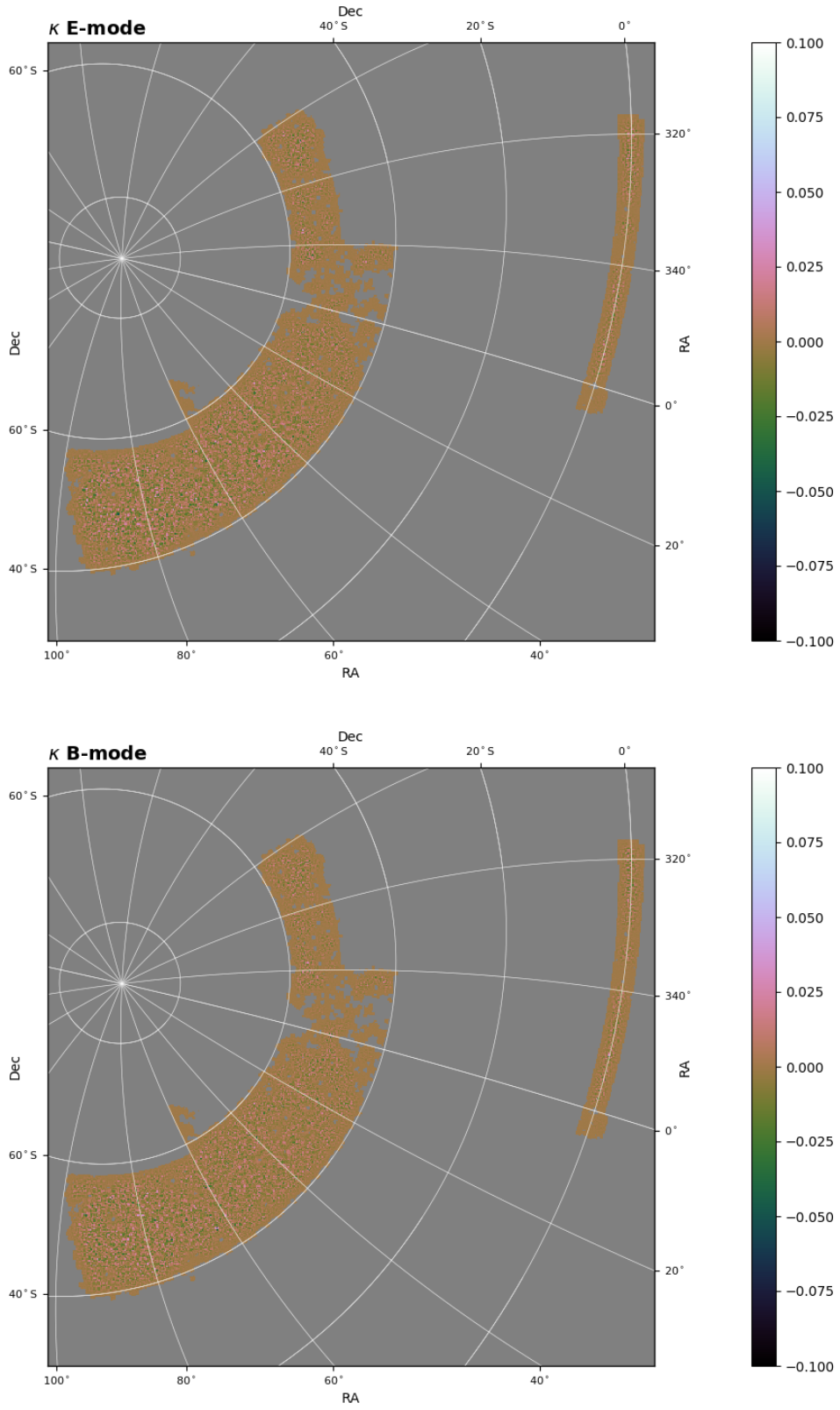

(a)

Figure 4.5: Reconstruction of convergence maps using the wavelet pure mode separation method from DES Y1 shear data. No smoothing is applied. Displayed in stereographic projection rotated to centre on the area shown.

reconstructed maps where smoothing is applied, displayed in Fig. 4.7 and Fig. 4.8. There is a very slight difference in the exact values of the convergence for the same features, but this is relatively minor compared to either the overall amplitude of the maps, or the differences caused by the apodisation effect.

In Fig. 4.7 and Fig. 4.8 we now compare the smoothed case. It can be seen that the same observations hold as for the unsmoothed case, albeit in a more obvious manner due to the removal of noise. Compare to the unsmoothed case it, can seen that the convergence maps of each method share the same features indicating the same underlying mass distribution. There are some large differences in the amplitudes of the maps, as can be observed in Fig. 4.9, and these differences are proportionately larger compared to the unsmoothed case. Observing Fig. 4.7 and Fig. 4.9 more closely, it can be seen that the differences in the central regions, not caused by apodisation, closely mirror the features of the smoothed KS convergence map, hence most of the differences are caused by the smaller overall amplitude of the wavelet convergence map, although the same features are preserved. Another side effect of the smoothing is the increase in the extent of apodisation at the mask boundaries, leading to further loss of information as more of the convergence map is obscured by this apodisation. This proves especially problematic for the parts of the observed sky that are smaller in area, as the apodisation obscures most of the convergence map information in these regions.

Most of this apodisation effect occurs at the boundary between the main area of observation and the large masked part of the sky, and does not appear to apply for very small masked areas, such as small areas in the larger body of the observed area. This suggests that the presence of small masked areas within the observed area does not significantly impact the reconstructed convergence maps or the E-B mode mixing.

This apodisation effect at the mask boundaries remains relatively consistent in extent for the same wavelet parameters, regardless of mask size and shape, so for a larger unmasked area it can be expected that the proportion of the map unaffected by this apodisation will increase (i.e. the boundary effects should decrease). Future surveys with improved sky coverage should produce data covering significantly larger areas and hence smaller masked areas, and so should see greater benefit

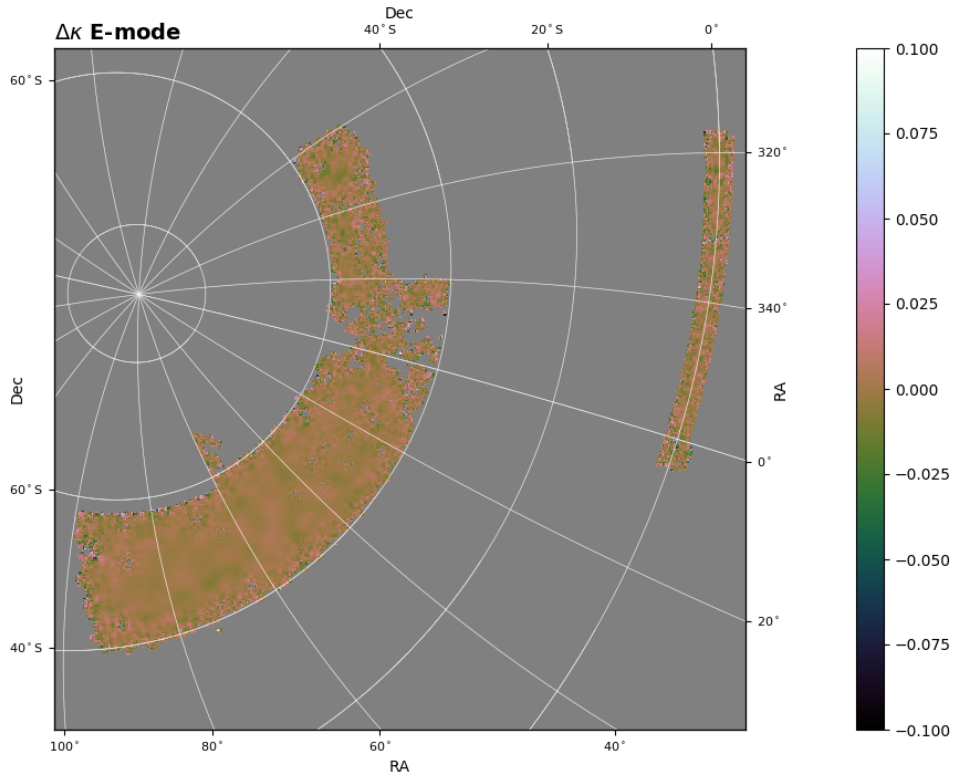

(a)

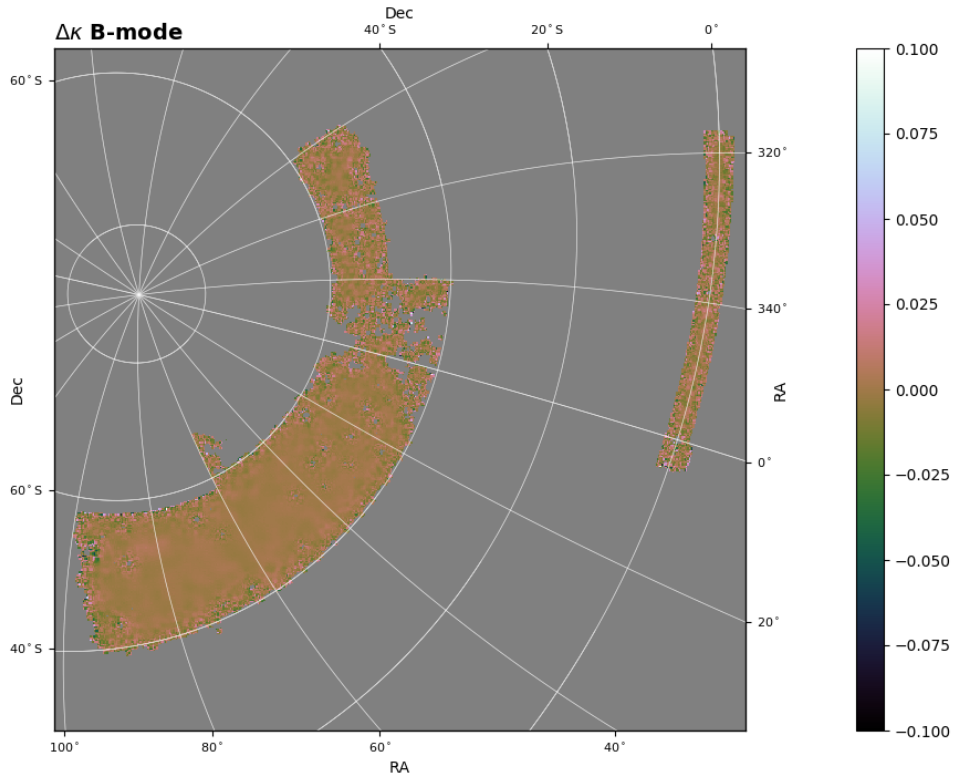

(b)

Figure 4.6: Difference between the reconstructed convergence maps displayed in Fig. 4.4 and Fig. 4.5 from DES Y1 shear data. Defined as $\Delta = \kappa_{KS} - \kappa_{wav}$. No smoothing is applied. Displayed in stereographic projection rotated to centre on the area shown.

from the wavelet method as the apodisation effect will be a comparatively smaller downside. Referring back to chapter 3, we observe this to be the case where effects at the masked boundary are proportionately smaller and the main body of observed data is minimally affected. However, it is still of importance to attempt to mitigate this effect in order to apply this method of wavelet pure mode E-B separation to current data such as the DES Y1 observations here.

From both the smoothed and unsmoothed cases, we observe the two main differences are the apodisation effect at the mask boundary and the slightly lower values across the entire map for the wavelet method convergence map in comparison to the KS method convergence map. While the loss in information at the mask boundaries is a distinct drawback to using wavelet-based E-B mode separation techniques, it must be balanced against the advantages in removing mask-induced mode-mixing through the use of pure mode estimators to fully separate the E-modes and B-modes by removing ambiguous modes. The primary alternative to the wavelet pure mode estimator is to use the harmonic pure mode estimator, the problems of which are discussed in chapter 3.

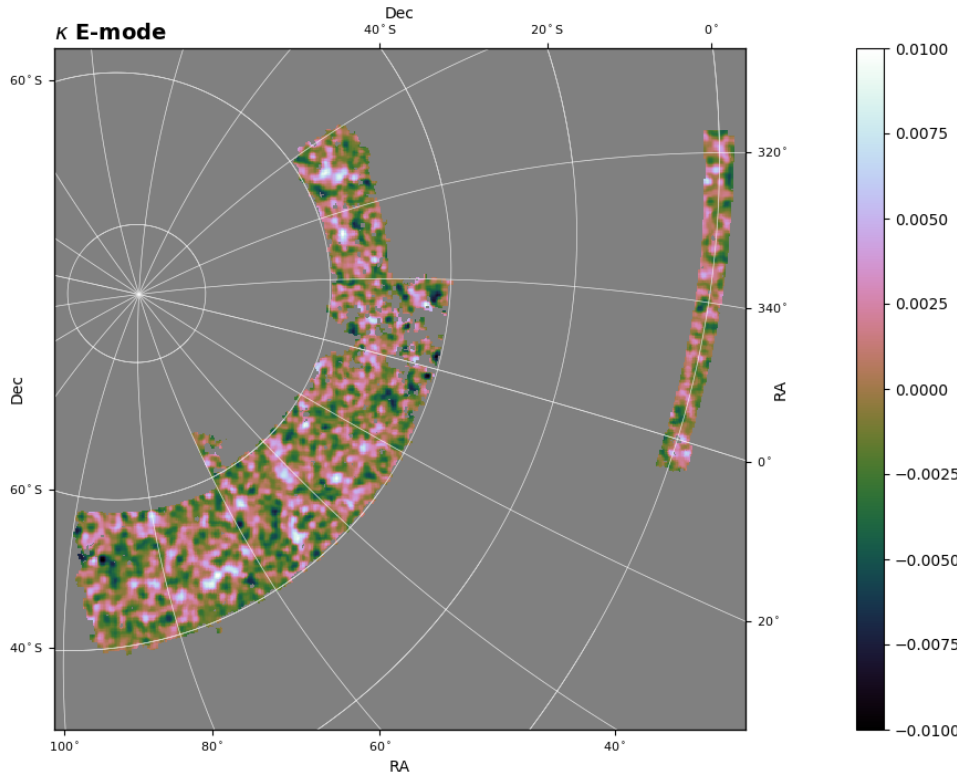

(a)

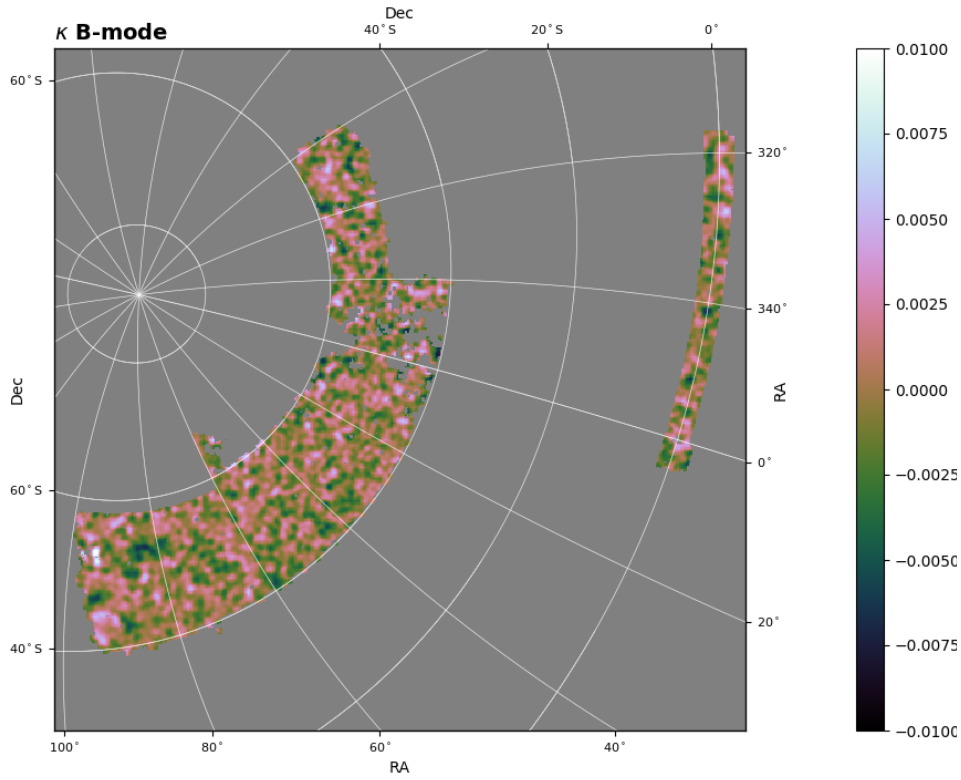

(b)

Figure 4.7: Reconstruction of convergence maps using the KS method from DES Y1 shear data. Smoothing is applied to the shear map in the form of a Gaussian kernel before the reconstruction is performed. Displayed in stereographic projection rotated to centre on the area shown.

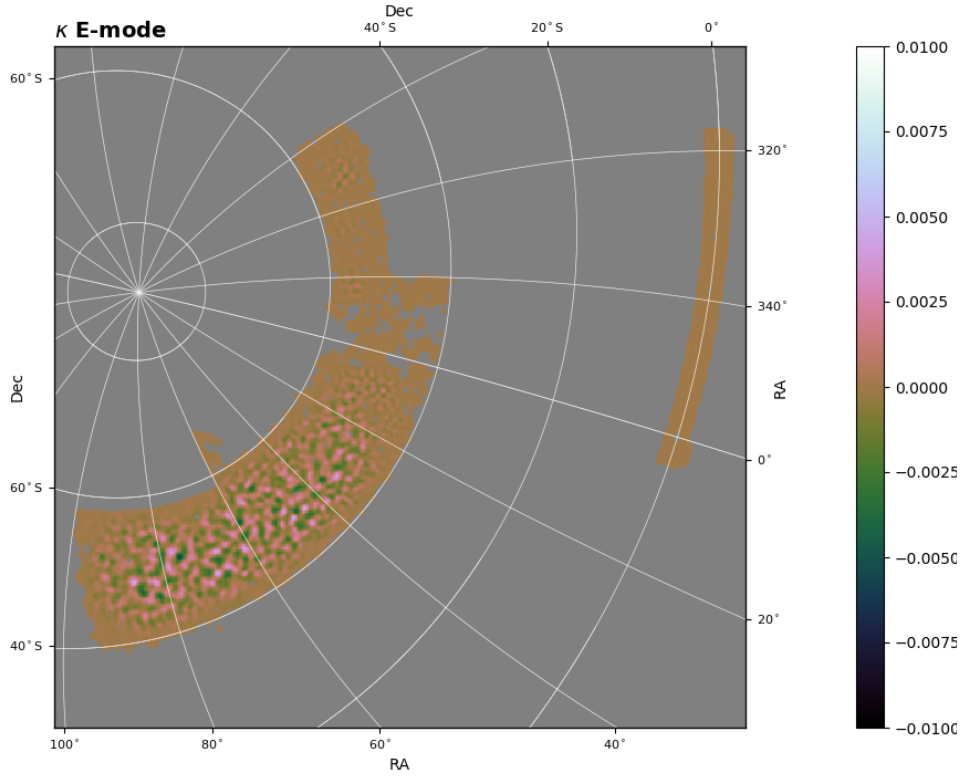

(a)

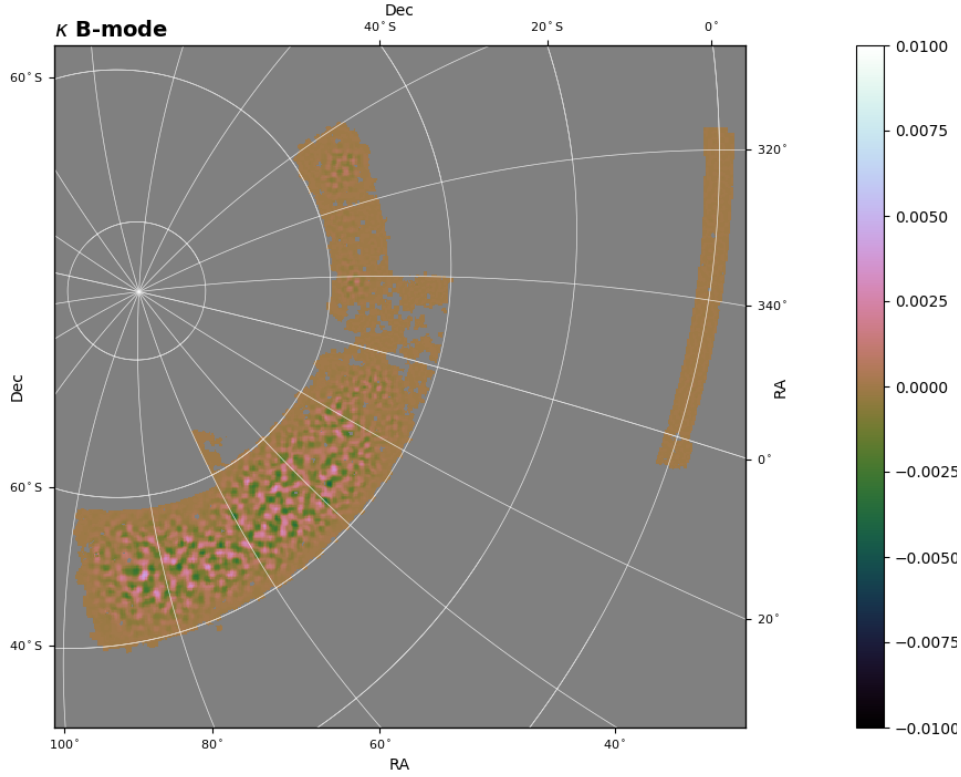

(b)

Figure 4.8: Reconstruction of convergence maps using the wavelet pure mode separation method from DES Y1 shear data. Smoothing is applied to the shear map in the form of a Gaussian kernel before the reconstruction is performed. Displayed in stereographic projection rotated to centre on the area shown.

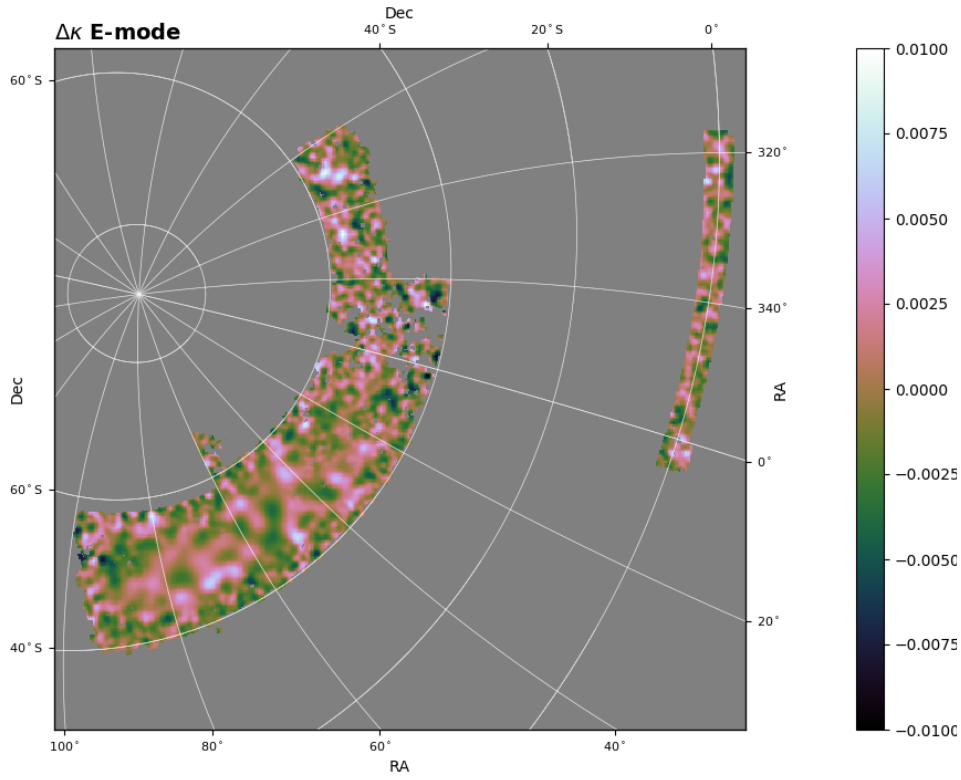

(a)

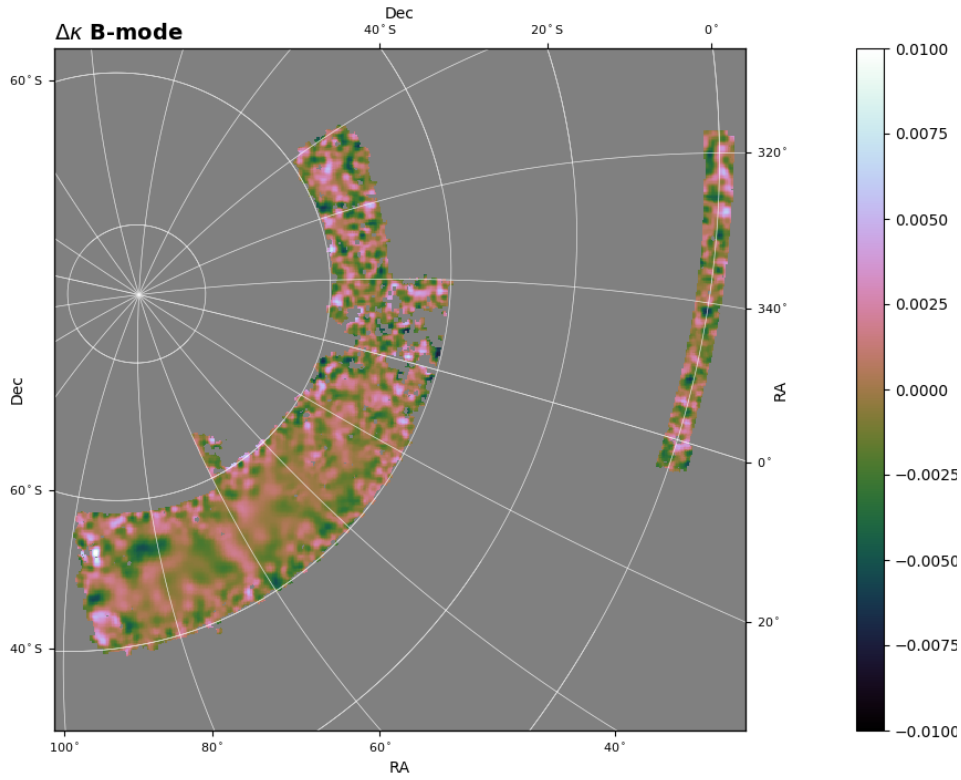

(b)

Figure 4.9: Difference between the reconstructed convergence maps displayed in Fig. 4.7 and Fig. 4.8 from DES Y1 shear data. Defined as $\Delta = \kappa_{KS} - \kappa_{wav}$. Smoothing is applied. Displayed in stereographic projection rotated to centre on the area shown.

4.4.2 Analysis of the convergence maps

We now discuss the various statistics derived from the convergence maps in Section 4.4. While we have derived the power spectra of maps in chapter 3, we opt not to do this here, as we do not know the true power spectra of the maps to draw comparison to.

Mean, standard deviation and RMS

First we consider the most straightforward statistics that can be derived from the given field: the mean in Table 4.1, standard deviation in Table 4.2 and root mean square (RMS) in Table 4.3. The statistics used are defined in Section 1.3.1 for clarity. For these statistics, we consider only the unmasked data.

As expected, the means are found to be close to 0, showing no significant bias in mean of the reconstructed maps, and the standard deviation and RMS values are very similar, which is to be expected if the mean of the field is close to 0. The standard deviation and RMS are of the field itself and provide a measure of the fluctuations present in the field. The lower standard deviation and RMS of the wavelet cases is expected due to both the apodisation effect and the decreased amplitude of the values of the convergence maps in comparison with the KS case.

Reconstruction Method	E-mode mean	B-mode mean
KS	1.4473×10^{-5}	-9.3939×10^{-5}
Smoothed KS	3.8503×10^{-5}	1.0446×10^{-4}
Wavelet EBsep	-1.4093×10^{-6}	-1.0873×10^{-6}
Smoothed Wavelet EBsep	4.2751×10^{-7}	6.3675×10^{-7}

Table 4.1: Table displaying the mean values of the reconstructed fields.

Minkowski Functionals

The MFs derived from the convergence fields reconstructed from the DES Y1 data are displayed for various cases: the unsmoothed KS case in Fig. 4.10, the smoothed KS case in Fig. 4.11, the unsmoothed wavelet pure mode case in Fig. 4.12, and the smoothed wavelet pure mode case in Fig. 4.13. For comparison, the analytic form of the MFs is calculated with Eq. 4.2.2 for each convergence map reconstruction,

Reconstruction Method	E-mode s.d.	B-mode s.d.
KS	0.01451	0.01401
Smoothed KS	0.00250	0.00194
Wavelet EBsep	0.00869	0.00833
Smoothed Wavelet EBsep	0.00076	0.00062

Table 4.2: Table displaying the standard deviation values of the reconstructed fields.

Reconstruction Method	E-mode RMS	B-mode RMS
KS	0.01451	0.01401
Smoothed KS	0.00250	0.00194
Wavelet EBsep	0.00869	0.00832
Smoothed Wavelet EBsep	0.00076	0.00062

Table 4.3: Table displaying the RMS values of the reconstructed field.

with the properties of each analytic MF adjusted to match each convergence map. These analytic MFs are the form expected of a Gaussian random field and provide a benchmark to test against which the Gaussianity of the reconstructed convergence fields can be tested.

Considering first the unsmoothed KS case MFs, as shown in Fig. 4.10, it is observed that the shape of the MFs adheres closely to the analytic form, although differing in size at the peaks and troughs for V_1 and V_2. This is likely caused by the presence of noise, as the smoothed case, displayed in Fig. 4.11, shows significantly less difference in the size of the MFs compared to the analytic form. Though the MFs of the smoothed KS adhere closely to the analytic form, there are slight differences that could potentially indicate non-Gaussianity, although influence from the KS reconstruction method would also have to be considered.

Now considering the MFs of the convergence maps reconstructed using the wavelet pure mode estimator, there is a distinct difference not only in size of the MFs but also the shapes. This difference is clear across all MFs and is much more significant in the smoothed case. Comparing the unsmoothed case to the KS method

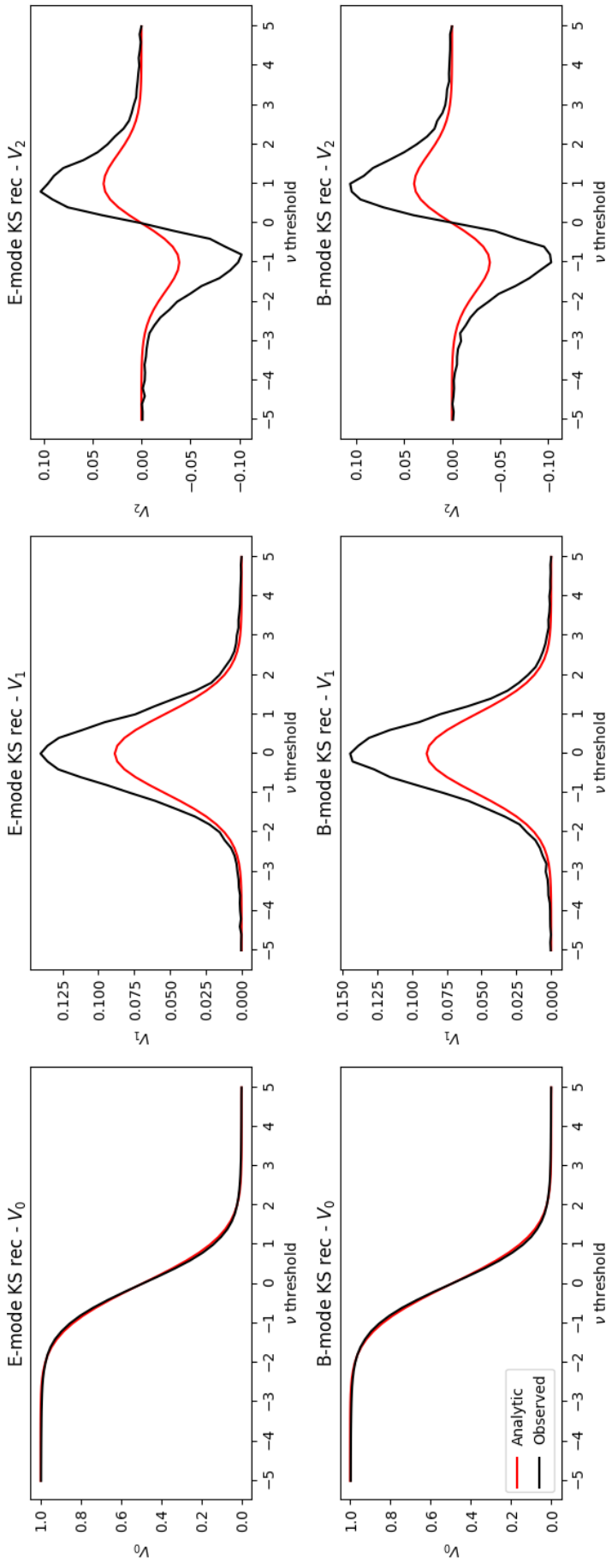

Figure 4.10: Minkowski Functionals of unsmoothed convergence maps reconstructed with the KS method, as shown in Fig. 4.4.

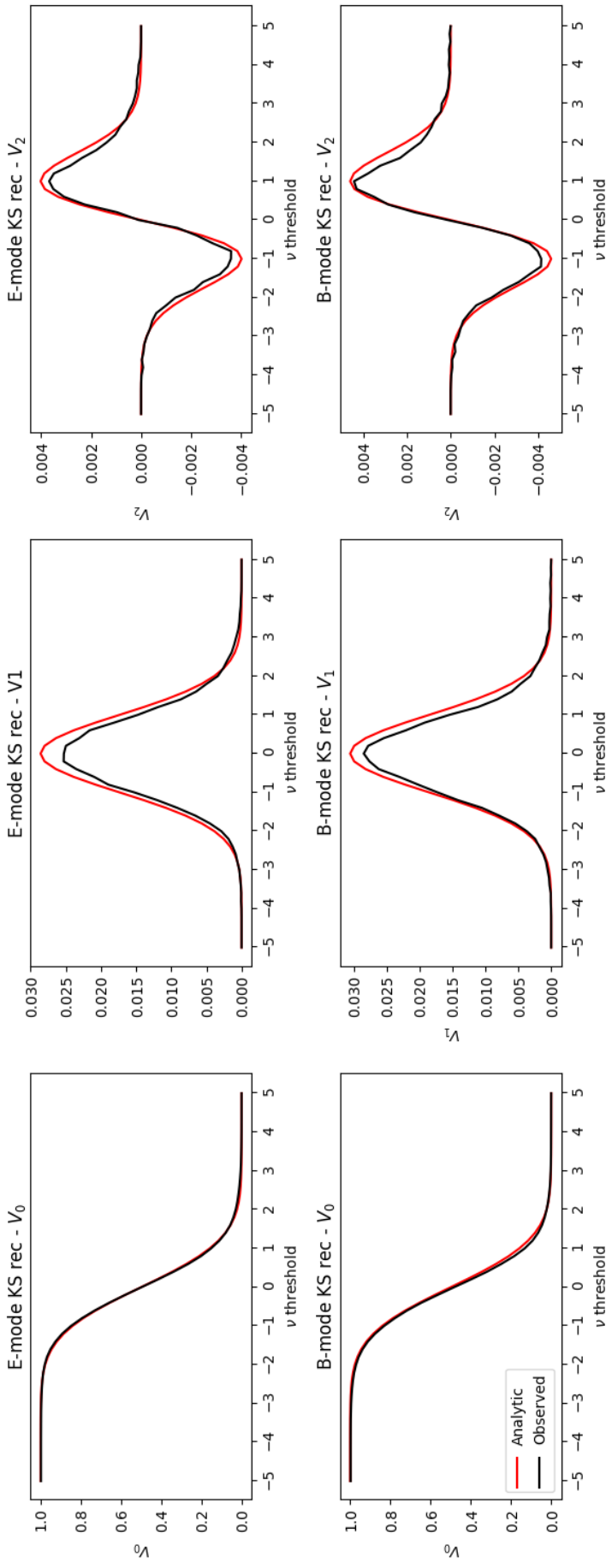

Figure 4.11: Minkowski Functionals of smoothed convergence maps reconstructed with the KS method, as shown in Fig. 4.7.

MFs, the unsmoothed wavelet MFs similarly display the increased amplitude over the analytic forms caused by noise. However, smoothing results in an increase in the divergence from the analytic case, the opposite of what is found with the KS method. Examining the convergence maps themselves, in Fig. 4.5 and Fig. 4.8, it is observed that the extent of the apodisation is increased and thus is likely to be the cause of the observed features of the MFs for the smoothed wavelet case.

From this MF comparison, we observe that the wavelet pure mode reconstruction is significantly non-Gaussian, with the source of this non-Gaussianity easily traced to the apodisation effect at the mask boundary, which is absent in the KS case. While the wavelet method has the advantage of producing cleaner maps with mode-mixing eliminated, the mask boundary apodisation is a significant drawback that results in a loss in information. This becomes especially problematic when the areas under consideration are small enough such that a significant proportion is affected by the apodisation, as can be seen in the DES Y1 reconstructed convergence maps. While useful information may still be obtained from the larger unmasked sections of the map, the smaller unmasked areas are almost entirely reduced to zero due to this effect.

While it is necessary to apply smoothing to reduce influence from the noise, post-recostruction smoothing has the adverse effect of increasing the extent of the apodisation at the mask boundary.

Removing the apodisation at mask boundaries

In order to better isolate the effect of the boundary apodisation on the MFs, we create an altered version of the original mask $M_{\rm old}$. This altered mask $M_{\rm new}$ is constructed to remove additional pixels close to the original masked area that fall below a certain absolute threshold and to be considered excessively apodised. This new altered mask is displayed in Fig. 4.14, with Fig. 4.15 illustrating the difference between the original mask and the altered mask. The altered mask is based on the smoothed wavelet pure mode reconstructed convergence maps as these display increased apodisation over the corresponding unsmoothed maps.

The construction of the altered mask is performed by evaluating each pixel in a wavelet pure mode reconstructed convergence map κ. Each pixel is evaluated to

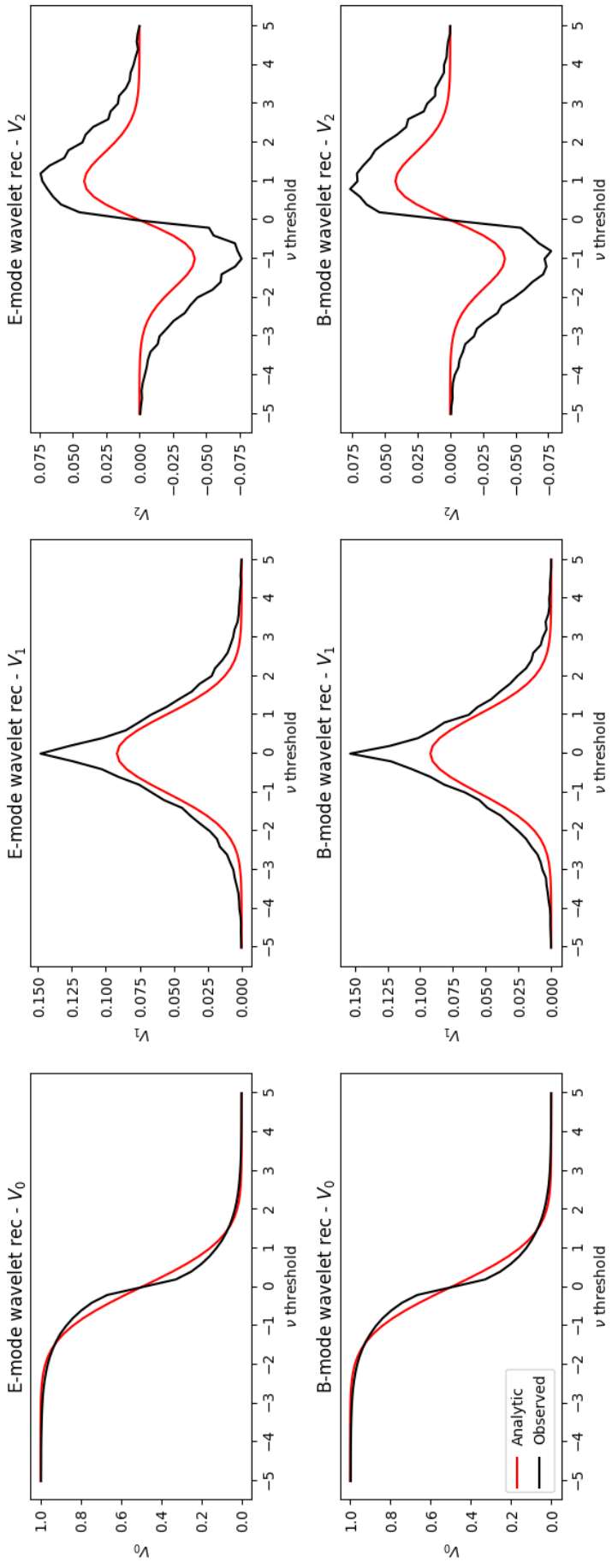

Figure 4.12: Minkowski Functionals of unsmoothed convergence maps reconstructed with wavelet pure estimators, as shown in Fig. 4.5.

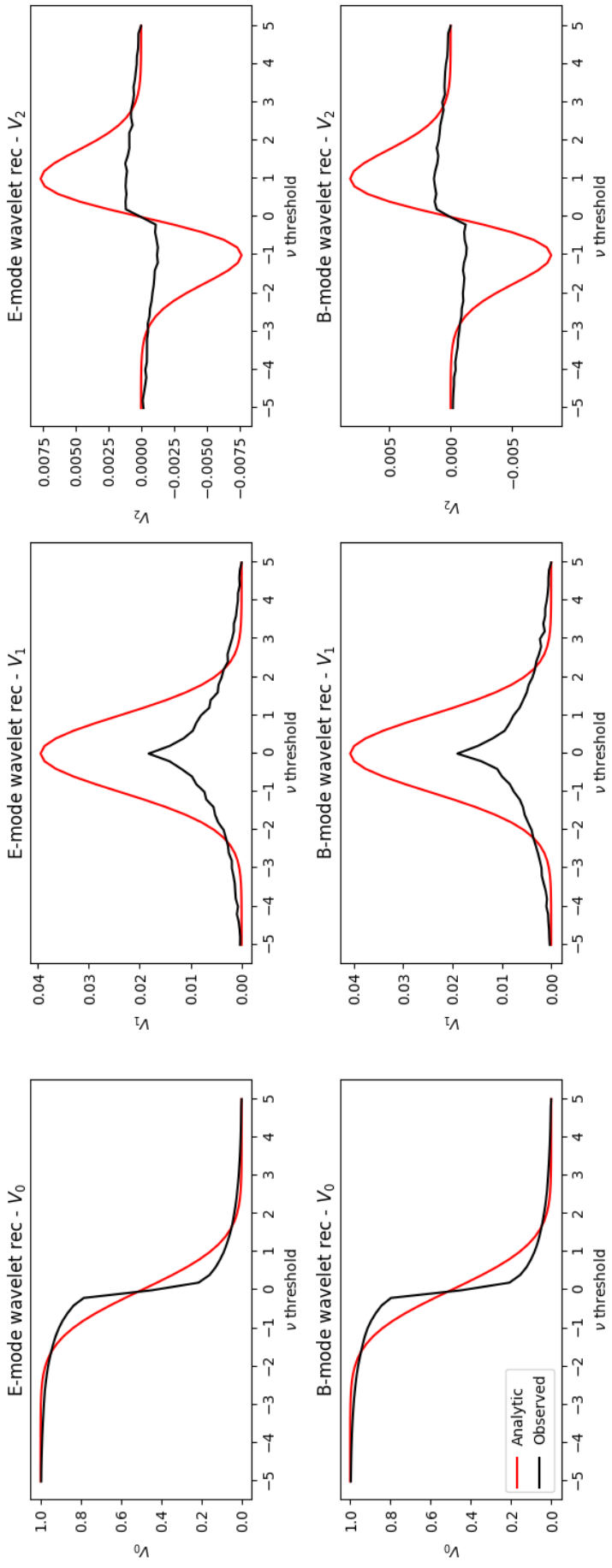

Figure 4.13: Minkowski Functionals of smoothed convergence maps reconstructed with wavelet pure estimators, as shown in Fig. 4.8.

check if it fulfils two conditions:

- The value of the convergence in this pixel falls below threshold κ_0,
- The pixel is within range D of a pixel that is part of the original mask M_{old}.

The first condition identifies pixels that are potentially apodised, while the second condition rules out pixels that have low convergence value but are not apodised due to not being in range of the mask boundary. For the second condition we must consider the distinction between the main continuous masked body at the boundary of which significant apodisation is observed, and small masked areas of a few pixels within the main body of unmasked data. These small masked areas do not produce noticeable apodisation like at the boundaries of the continuous masked area, hence they are neglected for the second condition and pixels within range of these are not counted as potentially apodised. This is done analytically, but the two parameters, the threshold κ_0 and pixel range D, are to be adjusted to appropriately match the value range of the convergence map and the pixel dimensions of the map respectively, and were selected to be $\kappa_0 = 0.01$ and $D = 20$

Observing the smoothed convergence map in Fig. 4.16 it can be seen that most of the apodisation is removed, at the expense of the removal of some sections of the data. Comparison between this unapodised area with the corresponding part of the KS convergence map shows little difference in key features.

The effect of apodisation at the mask boundary on the Minkwoski functionals is most clearly illustrated through comparing Fig. 4.13, corresponding to the convergence map in Fig. 4.8, and Fig. 4.17, corresponding to the convergence map in Fig. 4.16. With the removal of the apodised sections of the maps, the MFs show an increase in resemblance to the analytic Gaussian random field MFs, while still retaining the differences characterising the wavelet-based reconstruction. This marked difference to the MFs of the smoothed wavelet case without adjusting for the apodisation as shown in Fig. 4.13 suggest that it is preferable to remove the apodisation this way if seeking to analyse the topology of the convergence field under such circumstances. While this accounts for the loss of information caused by the apodisation that results in inaccurate results, this method is impractical to apply to observational data covering smaller areas as in such cases removing the apodised area may

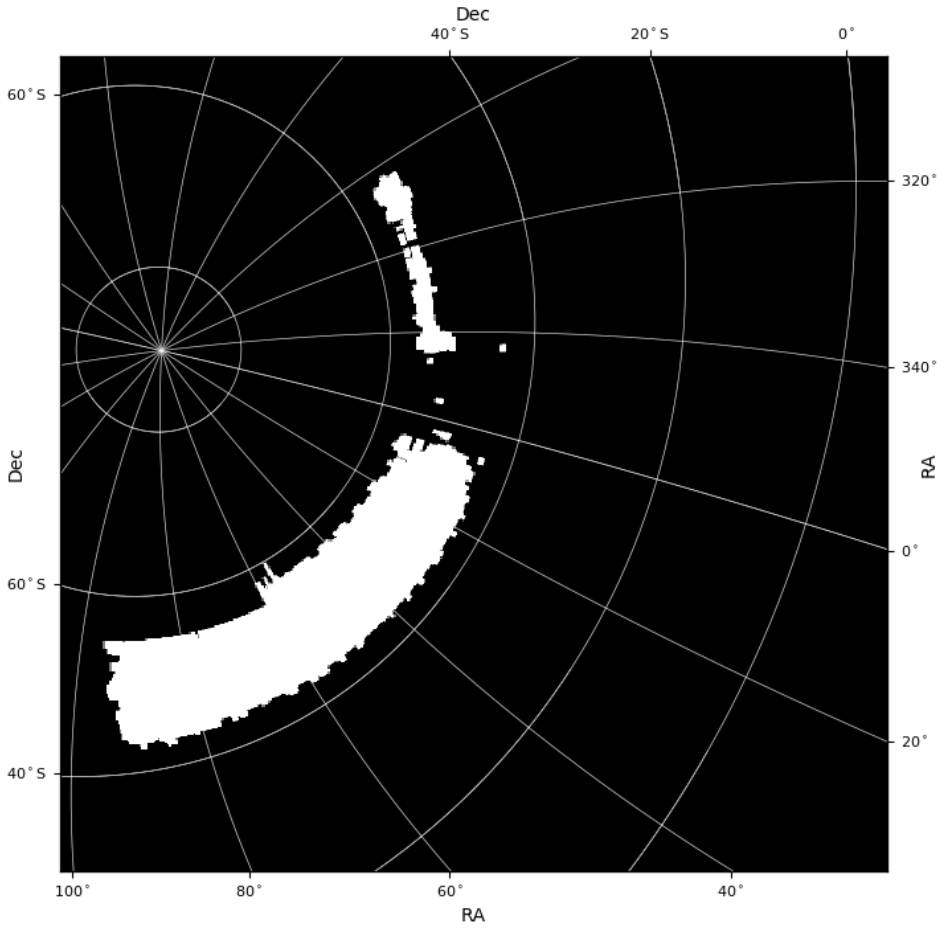

Figure 4.14: The new mask altered to remove the pixels affected by the boundary apodisation. This is constructed based on the apodisation found in the wavelet pure mode smoothed convergence maps. The masked area is indicated in black, the observed area is indicated in white.

remove too large a proportion of the data. Additionally, it is difficult to precisely determine the extent of the apodisation as it does not apply in a way that can be easily determined through an analytic formula, hence one must make a judgement on how much to remove until the new map is deemed acceptably free from the mask boundary apodisation.

Returning to the earlier derived statistics of the mean, standard deviation and RMS, the values of these statistics for the smoothed wavelet pure mode convergence map with the altered mask applied are given by Table 4.4. The new values display a slight increase over the smoothed wavelet convergence maps with the unaltered mask, as expected, but are still consistently below the corresponding values for the

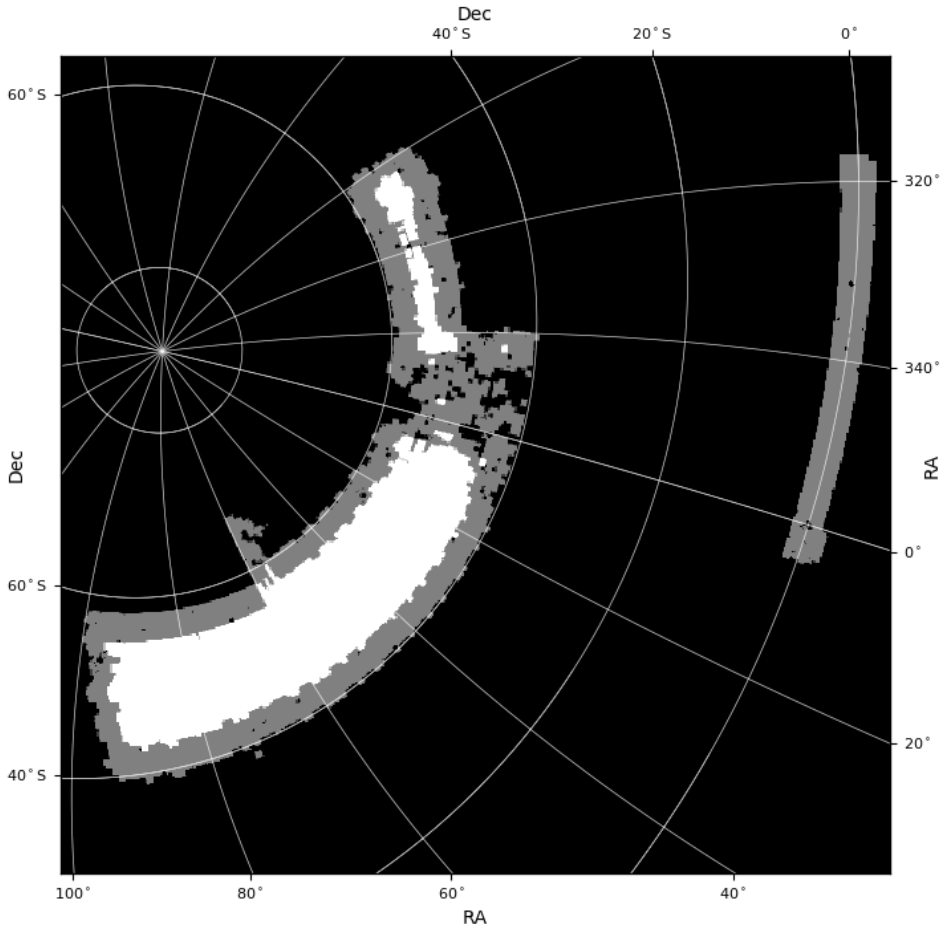

Figure 4.15: Comparison between original mask of DES Y1 shear data and new altered mask constructed by deleting apodised pixels near the boundary. The altered mask is constructed from data of the wavelet pure mode smoothed convergence maps. The masked area is indicated in black, the observed area is indicated in white and the grey area indicates removed pixels.

smoothed KS convergence maps. This indicates that apodisation influenced these statistics, but is not enough to account for the entire difference with the KS map statistics.

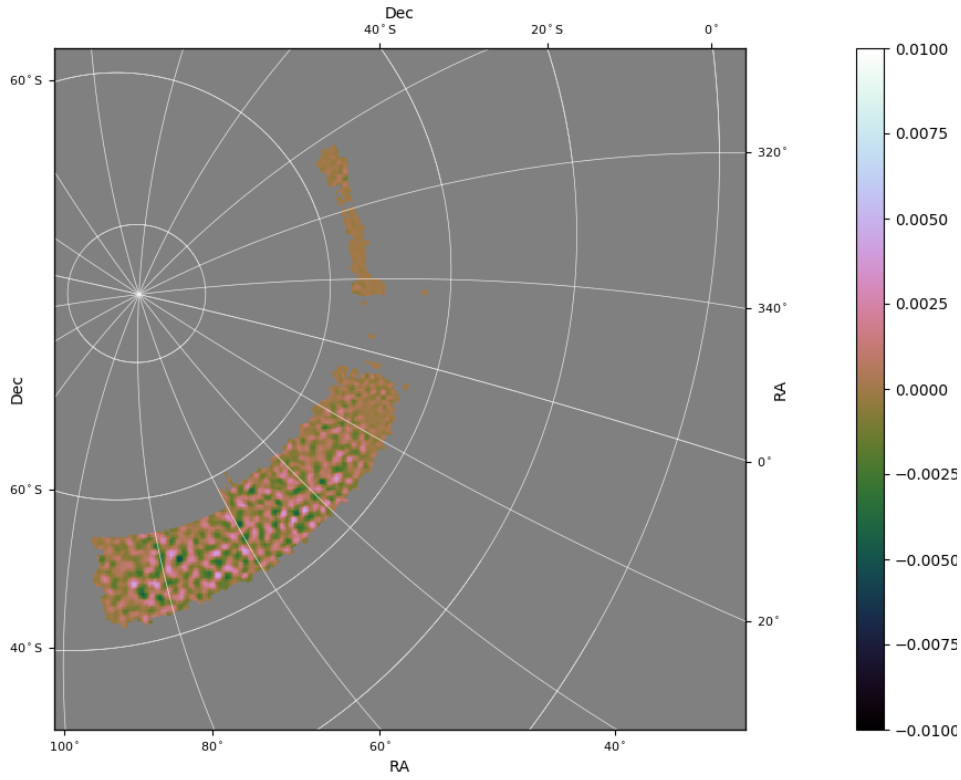

(a)

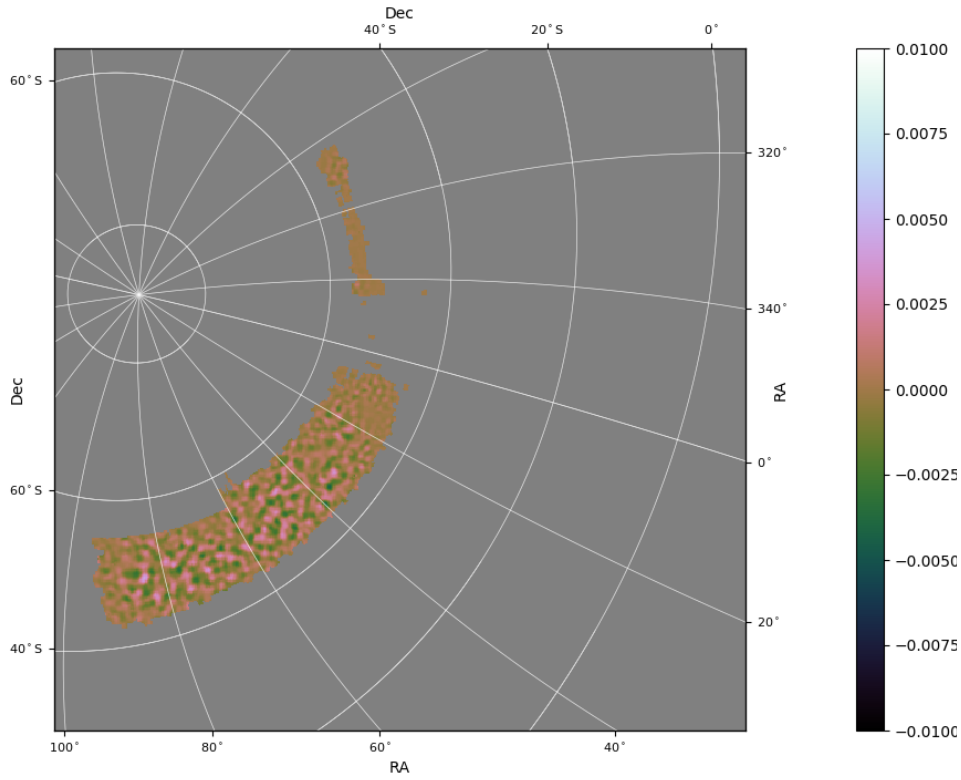

(b)

Figure 4.16: Reconstruction of convergence maps using the KS method from DES Y1 shear data, with additional new mask applied. This new altered mask is constructed to remove the apodised pixels. Smoothing is applied in the form of a Gaussian kernel. Displayed in stereographic projection rotated to centre on the area shown.

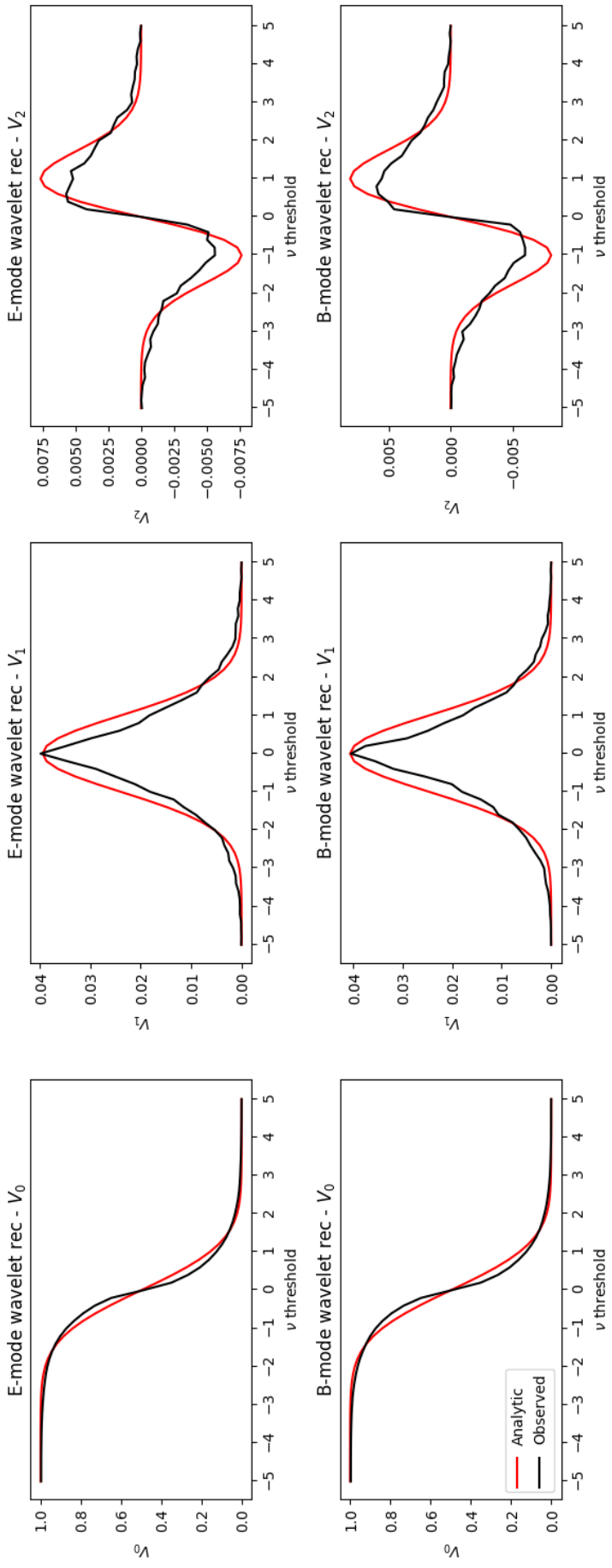

Figure 4.17: Minkowski Functionals of smoothed convergence maps reconstructed with wavelet pure estimators, as shown in Fig. 4.16, with additional masking to remove apodised area at boundary of original mask.

	E-mode	B-mode
Mean	7.12751×10^{-6}	4.28727×10^{-6}
Standard deviation	0.00110	0.00091
RMS	0.00110	0.00091

Table 4.4: Table displaying the mean values of the reconstructed field.

4.5 Conclusion

The use of the wavelet pure mode estimator for removing mode-mixing errors in the convergence map reconstruction has been previously demonstrated in chapter 3. The E-B mode separation is performed by applying a weighting function to remove ambiguous modes, and the use of scale-discretised wavelets allows this to be performed on different scales, alongside scale-dependent masking. Here we demonstrate its application to existing data in the form of the DES Y1 weak lensing catalogue. We find agreement between the wavelet pure mode estimator convergence maps and mass maps obtained in Chang et al. [2017], with significant map features matching and keeping in mind differences caused by the apodisation effect at mask boundaries.

The most significant difference is the introduction of this apodisation effect at mask boundaries, arising from the method of separating the E- and B-modes with scale-dependent masking. While the KS convergence maps do not have this apodisation, the KS case also neglects to account for masking and does not attempt to remove ambiguous modes. However, the corresponding harmonic pure mode estimator that accounts for the mask is poor at accurate reconstruction on the largest scales as previously discussed in chapter 3. The apodisation effect can be seen in chapter 3 through the pure wavelet residual maps showing greater difference along the mask boundaries, although it is not as noticeable due to the much broader masks used. It is probable that this apodisation is due to the wavelet pure estimator, however similar issues arise from the harmonic pure mode estimator, as seen in chapter 3, implying that this is an issue inherent to E-B estimators that incorporate masking rather than neglecting the mask as the KS estimator.

The mean, standard deviation and root mean square of the convergence fields are as expected, with means close to 0 and for all three the statistics for the wavelet case are lower than for the KS case. In addition, we obtain Minkowski Functionals for the convergence maps and observe close adherence to the analytic functions with minor differences for the KS case, but more significant deviations for the wavelet case. We apply further masking to the wavelet case maps to remove most of the apodisation at the mask boundary, and see an improvement in the MFs, with the

amplitudes of the MFs now being comparable to the analytic forms but retaining some differences in shape that could provide further investigation.

While the use of wavelet pure mode estimators for E-B separation holds promise, the apodisation effect at the mask boundary proves a challenge for data of large enough sky coverage to demand reconstruction on the sphere and small enough that the apodisation affects a significant proportion of the total area. This effect was not as noticeable in chapter 3 due to the much larger unmasked areas used, and the apodisation extent remains relatively constant independent of the mask. The most straightforward method of dealing with this would be to increase sky coverage, but in the interest of applying this method to existing data, it is also of interest to reduce the apodisation at the mask boundary. It would be useful for future research to further investigate the cause of this apodisation and potential methods of removing or reducing it, using simulations in order to compare the original and reconstructed E-modes and B-modes. In addition, future research could be performed for finding the MFs of the E- and B-modes under such circumstances, to evaluate how probable it is that the findings in this chapter indicate a potential deviation from the Gaussian random field MFs.

Conclusion

The aim of this thesis is to explore and evaluate new experimental techniques in the field of weak lensing, with focus on the curved sky setting that will be increasingly applicable to newer surveys as sky coverage increases. In this thesis we have discussed the advantages and disadvantages of various techniques used in extracting cosmological information from cosmic shear data. The results found in chapter 2 favour performing peak count and MF analysis on the sphere when sky coverage is significant enough to consider the spherical geometry of the data. In chapter 3 we evaluate the wavelet pure mode estimator as a method of mass map reconstruction and compare it with the KS estimator and the harmonic pure mode estimator. In chapter 4, the use of the wavelet pure mode estimator is demonstrated through application to DES Y1 data.

In chapter 2, we discussed how the act of projection from the sphere to the plane distorts the topography of the data and analysed how this impacts the peak count statistic and Minkowski functionals (MFs). Five planar projections were examined: the Mercator, sinusoidal, stereographic, orthographic and gnomonic. The weak lensing shear data used was simulated from the weak lensing power spectrum using standard cosmology, across a set number of iterations. The analysis was performed for the spherical and projected cases for each iteration of the map, using the variance across these iterations to evaluate the error on the maps. The shear

maps are constructed with additional noise in order to represent realistic conditions. The reconstruction on the plane uses the standard Kaiser-Squires (KS) estimator for each projected case. For the spherical case, the KS estimator is extended via spherical harmonics to the geometry of the surface of the sphere at fixed radius. The mask used has the full sphere masked except a simple circular area left unmasked, with the size of this unmasked area being quantified by the opening angle on the sphere. Smoothing is applied to the data at two stages - first during the generation of the simulated data and then during the KS reconstruction to mitigate the effect of noise. The degree of smoothing in the reconstruction step has a significant impact on the convergence maps, and thus the peak counts and MFs.

Both the full sky and partial sky case are studied, with the partial sky case being defined as the data with the mask applied. Both the opening angle for this mask and the degree of smoothing during reconstruction are examined as variables, as it is found that the projections perform better under different parameters for masking and smoothing. The peak count statistic of a convergence map is the number of detected peaks as a function of the signal-to-noise ratio (SNR) of the map. The peak counts used are the density of detected SNR peaks over the area of sky examined. Detection of the peaks is performed on the planar reconstructed maps for the projected cases and on the sphere for the spherical case. Likewise, the MFs are evaluated on the plane and sphere for the projected and spherical cases respectively.

It is found that for the peak counts in the full sky case, the number of peaks are overestimated for the projected cases in comparison to the spherical case. This is more significant at low SNR values and with less smoothing, indicating that this effect is most likely caused by the detection of false peaks induced by the noise. At higher SNR values, the peak counts converge for the cases, indicating that the number of true peaks of the highest mass densities are less affected. However, at high SNR there are very few peaks detected, leading to increased error. Peaks at medium SNR values provide the most useful range of data for evaluation, lacking the significant noise contamination at low SNR and high error due to low peak count at high SNR. Increasing the smoothing brings the projected peak counts better in line with the spherical case, although the Mercator projection still consistently overestimates peak counts and excessive smoothing leads to underestimation in

the gnomonic case. With an appropriate degree of smoothing, it is found that the sinusoidal, stereographic and orthographic projections display a reasonable approximation of the spherical case for peak counts for the full sky setting. The gnomonic case is especially unsuited for the full sky setting due to tending to infinity at the equator and significant distortion further from the projected poles.

The partial sky case examines only a circular area at the centre of the projection, with the rest of the map being masked. The size of the unmasked circle is determined by the opening angle as observed from the centre of the sphere. The projected maps exhibit less shape and angular distortion closer to the centre of the projection, therefore it is expected that for smaller opening angles the projections and spherical map will have a closer resemblance. With appropriate smoothing, on the smaller opening angles examined, the peak counts of the gnomonic and orthographic projections most closely match the spherical case. Comparing this with the figures in Section 2.2.2, the stereographic projection compresses the area focused on the north pole more than the orthographic or gnomonic projections, implying a loss in information. However, as the opening angle increases, provided the smoothing is kept the same, the gnomonic projection becomes less accurate.

Considering now the MFs, V_0, V_1 and V_2, there are visible, although minor, differences between the cases for V_0, which is reasonable as this corresponds to the area at different SNR thresholds. The differences are more pronounced with V_1 and V_2, measures of the boundary length and Euler characteristic respectively, with error increasing for smaller opening angles examined. It was found that this difference was caused by the influence of noise impacting the boundary lengths and Euler characteristic of the maps, corresponding to V_1 and V_2 respectively. In addition, the act of projection amplifies noise and performing reconstruction on the plane applies uneven smoothing when compared to reconstruction on the sphere.

In an attempt to accommodate this, we tested using projection-dependent smoothing. This evaluates maxima and minima of V_1 and V_2 for small opening angles, where the projected MFs are expected to more closely match the spherical MFs, and find the values of smoothing for which the MFs match across the examined cases. This reduces the noise to an appropriate degree and decreases the differences between the MFs on smaller opening angles. At larger opening angles and for the

full sky case, the impact of noise should be reduced and therefore the differences in MFs seen are expected to be caused by shape distortions due to the projections themselves, rather than caused by the noise.

The differences between the projected cases and spherical cases for peak counts and MFs can be mitigated through appropriate use of smoothing to reduce problems such as noise effects being amplified in the projection. However this approach does not deal with the underlying problems inherent to projection to the plane, especially in the full sky setting. Hence when the sky coverage of the data is sufficient that the spherical geometry must be considered, it is preferable to perform analysis on the sphere rather than projecting to the planar setting.

The examination of the partial sky case used simple masks with a single circular unmasked area, which do not accurately portray a realistic situation. While this is suitable for the work done in chapter 2, further investigation into projection effects using more realistic masks would be insightful, as non-circular masks would also undergo shape distortion during projection.

The peak count statistic and MFs were selected for analysis due to probing the non-Gaussianity and their clear dependence on the topology of the convergence field. Investigating the effect of projection on two-point statistics (such as the correlation function and power spectrum), genus statistics and higher-order spectra and comparison between the spherical case and different projected cases could provide a potential avenue for future study.

In chapter 3, we focus on reconstructing mass maps through E-B separation using wavelet pure estimators. The presence of a mask induces ambiguous modes which cannot be easily distinguished as E-modes or B-modes, leading to mode-mixing and inaccuracies in recovered convergence maps. We explore the use of wavelet pure estimators to separate E- and B-modes, drawing comparison with the KS estimator (equivalent to a harmonic pseudo estimator which neglects the mask) and harmonic pure estimator. The pure mode estimators work by applying a weighting function to remove ambiguous modes, with the addition of the wavelet estimator using scale-discretised wavelets allowing this, and the masking, to be performed separately on distinct scales to allow greater precision. The harmonic

pure and wavelet pure estimators incorporate data masking, while the KS does not. Residual maps are constructed by taking the difference between the true convergence map and the reconstructed convergence map at each pixel, with both maps being appropriately masked. It is found that the KS residuals appear smaller on larger scales, while the harmonic pure estimator residuals perform better on smaller scales such as at mask boundaries, but display distinct bias on large scales. In comparison to these, the wavelet pure estimator has significantly smaller residuals, hence less difference between the true E- and B-modes and the reconstructed E- and B-modes. Considering the mean ratios of the residuals to the reconstructed maps, the wavelet pure estimator has the best performance, followed by the KS estimator. Despite its apparent accuracy, the KS estimator neglects the mask and does not remove the ambiguous modes correctly.

Possible avenues for future investigation would include using directional wavelets and masks of different complexity and scale, in order to probe the key features of the wavelet pure estimator, the use of scale-discretised wavelets with scale-dependent masking.

The next step in the application of wavelet pure estimators is to apply them to real data, which is done in chapter 4. We used the DES Y1 weak lensing data due it being an example of a wide field survey with large sky coverage that techniques such as the wavelet pure estimator is expected to be applied to. In terms of visible features and mass distribution of the convergence map, we find good agreement between reconstruction performed through other methods [Chang et al., 2017] and our method using pure wavelet estimator E-B separation. However we find a distinct drawback to the wavelet-based method in the form of apodisation at the mask boundaries, which results in the loss of data in pixels close to the mask boundaries. This can also be seen in the pure wavelet residual maps in chapter 3, suggesting that this is inherent to the wavelet-based method. However, we have seen that the harmonic pure estimator also has distinct drawbacks and its own slight degree of apodisation, suggesting that such problems are inherent to estimators attempting to accommodate the mask. This was not noticed in chapter 3 due to the much larger area of analysis, in comparison to the smaller sky coverage for the DES Y1 data. The extent of the apodisation was found to be consistent throughout

a range of varied wavelet parameters and is most likely to be independent of the mask or wavelets used.

The mean, standard deviation and RMS of the convergence fields are as expected and indicate no significant bias. The MFs are also examined to compare the topology of the wavelet pure estimator E-modes and B-modes to the Gaussian random field case, displaying distinct deviation. However, it is almost certain that this deviation is due to the aforementioned apodisation, making it unsuitable for analysis. We applied an altered version of the mask to remove the apodised region and subsequently analysed this smaller area with reduced apodisation. This gives more reasonable MFs and with the adpodisation reduced it is more probable that the difference to the Gaussian random field MFs is either caused by the reconstruction method or indicates non-Gaussianity of the convergence field.

The use of wavelet pure estimators on data proved successful in that the recovered fields agree with other reconstructed methods and have reduced contamination due to mode-mixing. However, the mask boundary apodisation presents a major problem and future work on the wavelet pure estimators as an E-B separation technique should focus on understanding the cause of this apodisation and reducing the effect. As the range of the area apodised appears to be constant and unaffected by altering the wavelet parameters, it is expected to perform better on surveys with larger continuous sky coverage, but it is still of interest to find a way to reduce the apodisation so the method can be applied to surveys of smaller sizes.

This thesis has investigated the application of various techniques for reconstructing the convergence map from cosmic shear, with focus on performing this reconstruction in the curved sky setting. Our findings support moving from performing reconstruction on the 2D plane to performing reconstruction on the spherical setting in cases where the sky coverage is too large for flat-sky approximations to hold. We demonstrated the application of the wavelet pure estimator as a means of E-B separation to both simulated shear data and the DES Y1 shear data. While its performance is good with the simulated data on the full sky with a broad mask mimicking the Euclid mask, on smaller scales, such as for DES Y1, a distinct apodisation around the mask boundary is observed and dealing with this will be necessary if the wavelet pure estimator is to be applied to such data. Despite these drawbacks,

the wavelet pure estimator still holds promise as an analysis tool for weak lensing and should prove useful for upcoming large sky surveys.

Appendix

A Einstein Notation

When summing over tensors, the Einstein summation convention is often used as shorthand. For two tensors $x_i = (x_1, x_2, ..., x_N)$ and $y^i = (y^1, y^2, ..., y^N)$, the summation over the index i can be written as

$$x_i y^i = \sum_i^N x_i y^i = x_1 y^1 + x_2 y^2 + ... + x_N y^N. \tag{A.1}$$

B The Fourier Transform

Fourier analysis allows a given signal to be decomposed into a series of eigenfunctions in Fourier space. The Fourier transform of signal $f(x)$ is denoted as $\widetilde{(k)}$ where k is the Fourier coefficient of coordinate x, and is given by

$$\widetilde{f}(k) = \int f(x) e^{-2\pi i x k} dx \tag{B.1}$$

and the corresponding inverse Fourier transform is

$$f(x) = \int \widetilde{f}(x) e^{2\pi i x k} dk. \tag{B.2}$$

C The Spherical Harmonic Transform

The weak lensing signal exists natively on the curved sky geometry, hence transformations of the signal between real and harmonic space should use spherical coordinates. Extending the Fourier transform to the spherical setting involves separating the angular coordinates (θ, ϕ) and radial coordinate r respectively. Subsequent work in later chapters makes use of the spherical harmonic transform due to the need to perform tasks on the data in both real and harmonic space.

A scalar signal on the sphere $f(\theta, \phi)$ can be expanded into spherical harmonic representation as

$$f(\theta, \phi) = \sum_{\ell=0}^{\inf} \sum_{m=-\ell}^{l} f_{\ell m} Y_{\ell m}(\theta, \phi), \tag{C.1}$$

where $f_{\ell m}$ are the spherical coefficients representing the signal in harmonic space,

ℓ and m are the harmonic coefficients corresponding to θ and ϕ respectively, and $Y_{\ell m}(\theta,\phi)$ are the scalar spherical harmonic functions given by

$$Y_{\ell m}(\theta,\phi) = \sqrt{\frac{2l+1}{4\pi}\frac{(\ell-m)!}{(\ell+m)!}} P_l^m(\cos\theta) e^{im\phi}, \tag{C.2}$$

where $P_l^m(x)$ are the Legendre polynomials. The harmonic coefficients $f_{\ell m}$ are obtained through forward spherical harmonic transform with

$$f_{\ell m} = \int_{\phi=0}^{2\pi}\int_{\theta=0}^{\pi} f(\theta,\phi) Y^*_{\ell m}(\theta,\phi)\sin\theta d\theta d\phi. \tag{C.3}$$

It can be seen from inserting Eq. C.2 into Eq. C.3 that the integration over ϕ is the Fourier transform, hence Eq. C.3 becomes a Legendre transform as

$$f_{\ell m} = \int_{\theta=0}^{\pi} f_m(\theta) P_l^m(\cos\theta)\sin\theta d\theta. \tag{C.4}$$

D The Fourier-Bessel Transform

Introducing the Fourier-Bessel transform allows representation in harmonic space, with ℓ and m representing angular Fourier-Bessel coefficients and k representing the radial Fourier-Bessel coefficients. The Fourier-Bessel transform applied to the sphere is

$$f_{\ell m}(k) = \int_{S^2} d\Omega(\boldsymbol{n}) \sqrt{\frac{2}{\pi}} \int_{\mathbb{R}^+} dr r^2 f(\boldsymbol{n},r) Y^*_{\ell m}(\boldsymbol{n}) j_l^*(kr) \tag{D.1}$$

where $\boldsymbol{n} = (\theta,\phi)$ denotes the angular position, $d\Omega(\boldsymbol{n}) = \sin(\theta)d\theta d\phi$ denotes integrating over the sphere S^2, $\mathbb{R}^+$ denotes all positive real numbers, $Y^*_{\ell m}$ denotes the spin spherical harmonics and $j_l(kr)$ denotes the spherical Bessel function. Applying the Fourier-Bessel transform to Equation 1.2.4 allows the representation of the Newtonian potential in Fourier-Bessel space as

$$\Phi_{\ell m}(k;r) = \frac{3\Omega_M H_0^2}{2k^2 a(r)} \delta_{\ell m}(k;r). \tag{D.2}$$

For reference, the inverse Fourier-Bessel transform is

$$f(\boldsymbol{n},r) = \sum_{\ell m}\sqrt{\frac{2}{\pi}}\int_{\mathbb{R}^+} dk k^2 f_{\ell m}(k) Y_{\ell m}(\boldsymbol{n}) j_l(kr) \tag{D.3}$$

E The Limber Approximation

The Limber approximation (see Lemos et al. [2017]; Limber [1953]; LoVerde and Afshordi [2008] for greater detail) is to simplify calculations of properties of a 3D homogeneous isotropic random field (e.g. the convergence or mass overdensity fields) by relating said properties to those of the field's 2D projection. Derived originally in Limber [1953] for the 3D field representing counts of extragalactic nebulae, it has been adapted to other fields of astrophysical research, including weak lensing analysis. The approximation is usually used for computation of correlation functions such as the power spectrum. The Limber approximation substitutes Bessel functions with the following Dirac delta, δ^D, as ℓ tends towards infinity, [Kitching et al., 2011]

$$\lim_{\ell\to\infty} j_\ell(kr) \to \sqrt{\frac{\pi}{2(\ell+\frac{1}{2})}}\left(kr - \left(\ell+\frac{1}{2}\right)\right) \tag{E.1}$$

where r is the comoving radial distance coordinate, k is the harmonic coefficient of r and ℓ is the harmonic coefficient of anglular position θ. Application of the Limber approximation requires the integration be performed over small angular scales and that the quantities being integrated vary at different rates, such that some of said quantities vary slower than others.

Bibliography

Alexandra Abate et al. Large Synoptic Survey Telescope: Dark Energy Science Collaboration. ., 2012. (Cited at page 19)

T. Abbott et al. The dark energy survey. ., 2005. (Cited at page 19)

T. M. C. Abbott et al. The Dark Energy Survey Data Release 1. *Astrophys. J. Suppl.*, 239(2):18, 2018. doi: 10.3847/1538-4365/aae9f0. (Cited at pages 134, 135 e 136)

P. A. R. Ade et al. Planck 2015 results. XVI. Isotropy and statistics of the CMB. *Astron. Astrophys.*, 594:A16, 2016a. doi: 10.1051/0004-6361/201526681. (Cited at page 25)

P. A. R. Ade et al. Planck 2015 results. XIII. Cosmological parameters. *Astron. Astrophys.*, 594:A13, 2016b. doi: 10.1051/0004-6361/201525830. (Cited at pages 25 e 119)

N. Aghanim et al. Planck 2018 results. VI. Cosmological parameters. 2018. (Cited at pages 23, 24 e 32)

R. A. Alpher, H. Bethe, and G. Gamow. The origin of chemical elements. *Phys. Rev.*, 73:803–804, Apr 1948. doi: 10.1103/PhysRev.73.803. URL https://link.aps.org/doi/10.1103/PhysRev.73.803. (Cited at page 25)

Adam Amara and Tom Kitching. E and b modes. http://gravitationallensing.pbworks.com/w/page/15553245/Cosmic%20Lensing, 2016. Accessed: 30/10/2016. (Cited at pages 46 e 47)

L. Amendola, S. Appleby, D. Bacon, T. Baker, M. Baldi, N. Bartolo, A. Blanchard, C. Bonvin, S. Borgani, E. Branchini, C. Burrage, S. Camera, C. Carbone, L. Casarini, M. Cropper, C. de Rham, C. Di Porto, A. Ealet, P. G. Ferreira, F. Finelli, J. García-Bellido, T. Giannantonio, L. Guzzo, A. Heavens, L. Heisenberg, C. Heymans, H. Hoekstra, L. Hollenstein, R. Holmes, O. Horst, K. Jahnke, T. D. Kitching, T. Koivisto, M. Kunz, G. La Vacca, M. March, E. Majerotto, K. Markovic, D. Marsh, F. Marulli, R. Massey, Y. Mellier, D. F. Mota, N. J. Nunes, W. Percival, V. Pettorino, C. Porciani, C. Quercellini, J. Read, M. Rinaldi, D. Sapone, R. Scaramella, C. Skordis, F. Simpson, A. Taylor, S. Thomas, R. Trotta, L. Verde, F. Vernizzi, A. Vollmer, Y. Wang, J. Weller, and T. Zlosnik. Cosmology and Fundamental Physics with the Euclid Satellite. *Living Reviews in Relativity*, 16:6, September 2013. doi: 10.12942/lrr-2013-6. (Cited at page 73)

Luca Amendola et al. Cosmology and fundamental physics with the Euclid satellite. *Living Rev. Rel.*, 16:6, 2013. doi: 10.12942/lrr-2013-6. (Cited at pages 18 e 19)

Jean-Pierre Antoine, Romain Murenzi, Pierre Vandergheynst, and Syed Twareque Ali. *Two-dimensional wavelets and their relatives*. Cambridge University Press, 2008. (Cited at page 65)

D. J. Bacon and A. N. Taylor. Mapping the 3D dark matter potential with weak shear. *Monthly Notices of the Royal Astronomical Society*, 344:1307–1326, October 2003. doi: 10.1046/j.1365-8711.2003.06922.x. (Cited at page 72)

R. B. Barreiro, J. L. Sanz, E. Martinez-Gonzalez, L. Cayon, and Joseph Silk. Peaks in the cosmic microwave background: Flat versus open models. *Astrophys. J.*, 478:1, 1997. doi: 10.1086/303793. (Cited at pages 108 e 132)

R. Belen Barreiro and M. P. Hobson. The Discriminating power of wavelets to detect non-Gaussianity in the CMB. *Mon. Not. Roy. Astron. Soc.*, 327:813, 2001. doi: 10.1046/j.1365-8711.2001.04806.x. (Cited at pages 108 e 132)

Matthias Bartelmann and Peter Schneider. Weak gravitational lensing. *Phys. Rept.*, 340:291–472, 2001. doi: 10.1016/S0370-1573(00)00082-X. (Cited at pages 40, 46 e 49)

Daniel Baumann. Inflation. In *Physics of the large and the small, TASI 09, proceedings of the Theoretical Advanced Study Institute in Elementary Particle Physics, Boulder, Colorado, USA, 1-26 June 2009*, pages 523–686, 2011. doi: 10.1142/9789814327183_0010. (Cited at page 25)

Matthew R. Becker and Eduardo Rozo. Fourier Band-Power E/B-mode Estimators for Cosmic Shear. *Mon. Not. Roy. Astron. Soc.*, 457(1):304–312, 2016. doi: 10.1093/mnras/stv3018. (Cited at pages 109 e 133)

Narciso Benitez. Bayesian photometric redshift estimation. *Astrophys. J.*, 536:571–583, 2000. doi: 10.1086/308947. (Cited at page 51)

D. P. Bennett et al. The MACHO project dark matter search. *ASP Conf. Ser.*, 88:95, 1996. (Cited at page 24)

J. Bergé, A. Amara, and A. Réfrégier. Optimal Capture of Non-Gaussianity in Weak-Lensing Surveys: Power Spectrum, Bispectrum, and Halo Counts. *The Astrophysical Journal*, 712:992–1002, April 2010a. doi: 10.1088/0004-637X/712/2/992. (Cited at pages 108 e 132)

J. Bergé, A. Amara, and A. Réfrégier. Optimal Capture of Non-Gaussianity in Weak-Lensing Surveys: Power Spectrum, Bispectrum, and Halo Counts. *The Astrophysical Journal*, 712:992–1002, April 2010b. doi: 10.1088/0004-637X/712/2/992. (Cited at page 71)

Lars Bergstrom. Dark Matter Candidates. *New J. Phys.*, 11:105006, 2009. doi: 10.1088/1367-2630/11/10/105006. (Cited at page 24)

Francis Bernardeau, Cyril Pitrou, and Jean-Philippe Uzan. CMB spectra and bispectra calculations: making the flat-sky approximation rigorous. *JCAP*, 1102:015, 2011. doi: 10.1088/1475-7516/2011/02/015. (Cited at page 51)

Gianfranco Bertone and M. P. Tait, Tim. A new era in the search for dark matter. *Nature*, 562(7725):51–56, 2018. doi: 10.1038/s41586-018-0542-z. (Cited at page 24)

Micol Bolzonella, Joan-Marc Miralles, and Roser Pello'. Photometric redshifts based on standard SED fitting procedures. *Astron. Astrophys.*, 363:476–492, 2000. (Cited at page 51)

Jude Bowyer and Andrew H. Jaffe. Improved Method for Detecting Local Discontinuities in CMB data by Finite Differencing. *Phys. Rev.*, D83:023503, 2011. doi: 10.1103/PhysRevD.83.023503. (Cited at page 109)

Jude Bowyer, Andrew H. Jaffe, and Dmitri I. Novikov. MasQU: Finite Differences on Masked Irregular Stokes Q,U Grids. *ArXiv e-prints*, 2011. (Cited at page 109)

A. Boyarsky, M. Drewes, T. Lasserre, S. Mertens, and O. Ruchayskiy. Sterile Neutrino Dark Matter. *Prog. Part. Nucl. Phys.*, 104:1–45, 2019. doi: 10.1016/j.ppnp.2018.07.004. (Cited at page 24)

Thomas J. Broadhurst, A. N. Taylor, and J. A. Peacock. Mapping cluster mass distributions via gravitational lensing of background galaxies. *Astrophys. J.*, 438:49, 1995. doi: 10.1086/175053. (Cited at pages 108 e 132)

E. F. Bunn and B. Wandelt. Pure E and B polarization maps via Wiener filtering. *Physical Review D*, 96(4):043523, August 2017. doi: 10.1103/PhysRevD.96.043523. (Cited at pages 109 e 133)

Emory F. Bunn, Matias Zaldarriaga, Max Tegmark, and Angelica de Oliveira-Costa. E/B decomposition of finite pixelized CMB maps. *Phys. Rev.*, D67:023501, 2003. doi: 10.1103/PhysRevD.67.023501. (Cited at pages 109, 110 e 133)

Laurent Canetti, Marco Drewes, and Mikhail Shaposhnikov. Matter and Antimatter in the Universe. *New J. Phys.*, 14:095012, 2012. doi: 10.1088/1367-2630/14/9/095012. (Cited at page 25)

Sean M. Carroll. The cosmological constant. *Living Reviews in Relativity*, 4(1):1, Feb 2001. ISSN 1433-8351. doi: 10.12942/lrr-2001-1. URL https://doi.org/10.12942/lrr-2001-1. (Cited at page 35)

Patricia G. Castro, A. F. Heavens, and T. D. Kitching. Weak lensing analysis in three dimensions. *Phys. Rev.*, D72:023516, 2005. doi: 10.1103/PhysRevD.72.023516. (Cited at page 47)

C. Chang, V. Vikram, B. Jain, D. Bacon, A. Amara, M. R. Becker, G. Bernstein, C. Bonnett, S. Bridle, D. Brout, M. Busha, J. Frieman, E. Gaztanaga, W. Hartley, M. Jarvis, T. Kacprzak, A. Kovács, O. Lahav, H. Lin, P. Melchior, H. Peiris, E. Rozo,

E. Rykoff, C. Sánchez, E. Sheldon, M. A. Troxel, R. Wechsler, J. Zuntz, T. Abbott, F. B. Abdalla, S. Allam, J. Annis, A. H. Bauer, A. Benoit-Lévy, D. Brooks, E. Buckley-Geer, D. L. Burke, D. Capozzi, A. Carnero Rosell, M. Carrasco Kind, F. J. Castander, M. Crocce, C. B. D'Andrea, S. Desai, H. T. Diehl, J. P. Dietrich, P. Doel, T. F. Eifler, A. E. Evrard, A. Fausti Neto, B. Flaugher, P. Fosalba, D. Gruen, R. A. Gruendl, G. Gutierrez, K. Honscheid, D. James, S. Kent, K. Kuehn, N. Kuropatkin, M. A. G. Maia, M. March, P. Martini, K. W. Merritt, C. J. Miller, R. Miquel, E. Neilsen, R. C. Nichol, R. Ogando, A. A. Plazas, A. K. Romer, A. Roodman, M. Sako, E. Sanchez, I. Sevilla, R. C. Smith, M. Soares-Santos, F. Sobreira, E. Suchyta, G. Tarle, J. Thaler, D. Thomas, D. Tucker, and A. R. Walker. Wide-Field Lensing Mass Maps from Dark Energy Survey Science Verification Data. *Physical Review Letters*, 115(5): 051301, July 2015. doi: 10.1103/PhysRevLett.115.051301. (Cited at page 72)

C. Chang, A. Pujol, B. Mawdsley, D. Bacon, J. Elvin-Poole, P. Melchior, A. Kovács, B. Jain, B. Leistedt, T. Giannantonio, A. Alarcon, E. Baxter, K. Bechtol, M. R. Becker, A. Benoit-Lévy, G. M. Bernstein, C. Bonnett, M. T. Busha, A. Carnero Rosell, F. J. Castander, R. Cawthon, L. N. da Costa, C. Davis, J. De Vicente, J. DeRose, A. Drlica-Wagner, P. Fosalba, M. Gatti, E. Gaztanaga, D. Gruen, J. Gschwend, W. G. Hartley, B. Hoyle, E. M. Huff, M. Jarvis, N. Jeffrey, T. Kacprzak, H. Lin, N. MacCrann, M. A. G. Maia, R. L. C. Ogando, J. Prat, M. M. Rau, R. P. Rollins, A. Roodman, E. Rozo, E. S. Rykoff, S. Samuroff, C. Sánchez, I. Sevilla-Noarbe, E. Sheldon, M. A. Troxel, T. N. Varga, P. Vielzeuf, V. Vikram, R. H. Wechsler, J. Zuntz, T. M. C. Abbott, F. B. Abdalla, S. Allam, J. Annis, E. Bertin, D. Brooks, E. Buckley-Geer, D. L. Burke, M. Carrasco Kind, J. Carretero, M. Crocce, C. E. Cunha, C. B. D'Andrea, S. Desai, H. T. Diehl, J. P. Dietrich, P. Doel, J. Estrada, A. Fausti Neto, E. Fernandez, B. Flaugher, J. Frieman, J. García-Bellido, R. A. Gruendl, G. Gutierrez, K. Honscheid, D. J. James, T. Jeltema, M. W. G. Johnson, M. D. Johnson, S. Kent, D. Kirk, E. Krause, K. Kuehn, S. Kuhlmann, O. Lahav, T. S. Li, M. Lima, M. March, P. Martini, F. Menanteau, R. Miquel, J. J. Mohr, E. Neilsen, R. C. Nichol, D. Petravick, A. A. Plazas, A. K. Romer, M. Sako, E. Sanchez, V. Scarpine, M. Schubnell, M. Smith, R. C. Smith, M. Soares-Santos, F. Sobreira, E. Suchyta, G. Tarle, D. Thomas, D. L. Tucker, A. R. Walker, W. Wester, and Y. Zhang. Dark Energy Survey Year 1 Results: Curved-Sky Weak Lensing Mass Map. *ArXiv e-prints*, August 2017. doi:

10.1093/mnras/stx3363. (Cited at pages 61, 72, 134, 136, 137, 143, 165 e 171)

Gayoung Chon, Anthony Challinor, Simon Prunet, Eric Hivon, and Istvan Szapudi. Fast estimation of polarization power spectra using correlation functions. *Mon. Not. Roy. Astron. Soc.*, 350:914, 2004. doi: 10.1111/j.1365-2966.2004.07737.x. (Cited at pages 109 e 133)

Timothy Clifton, Pedro G. Ferreira, Antonio Padilla, and Constantinos Skordis. Modified Gravity and Cosmology. *Phys. Rept.*, 513:1–189, 2012. doi: 10.1016/j.physrep.2012.01.001. (Cited at page 35)

Asantha Cooray and Wayne Hu. Power spectrum covariance of weak gravitational lensing. *Astrophys. J.*, 554:56–66, 2001. doi: 10.1086/321376. (Cited at page 61)

A. C. Davis and T. W. B. Kibble. Fundamental cosmic strings. *Contemp. Phys.*, 46:313–322, 2005. doi: 10.1080/00107510500165204. (Cited at pages 108 e 132)

J. T. A. de Jong, G. A. Verdoes Kleijn, K. H. Kuijken, and E. A. Valentijn. The Kilo-Degree Survey. *Experimental Astronomy*, 35:25–44, January 2013. doi: 10.1007/s10686-012-9306-1. (Cited at pages 19 e 70)

J. Delabrouille et al. Exploring cosmic origins with CORE: Survey requirements and mission design. *JCAP*, 1804(04):014, 2018. doi: 10.1088/1475-7516/2018/04/014. (Cited at pages 108 e 132)

J. P. Dietrich and J. Hartlap. Cosmology with the shear-peak statistics. *Monthly Notices of the Royal Astronomical Society*, 402:1049–1058, February 2010. doi: 10.1111/j.1365-2966.2009.15948.x. (Cited at pages 85 e 86)

R. Durrer, M. Kunz, and A. Melchiorri. Cosmic microwave background anisotropies from scaling seeds: Global defect models. *Phys. Rev.*, D59:123005, 1999. doi: 10.1103/PhysRevD.59.123005. (Cited at pages 108 e 132)

J. Elvin-Poole, M. Crocce, A. J. Ross, T. Giannantonio, E. Rozo, E. S. Rykoff, S. Avila, N. Banik, J. Blazek, S. L. Bridle, R. Cawthon, A. Drlica-Wagner, O. Friedrich, N. Kokron, E. Krause, N. MacCrann, J. Prat, C. Sánchez, L. F. Secco, I. Sevilla-Noarbe, M. A. Troxel, T. M. C. Abbott, F. B. Abdalla, S. Allam, J. Annis, J. Asorey, K. Bechtol, M. R. Becker, A. Benoit-Lévy, G. M. Bernstein, E. Bertin, D. Brooks,

E. Buckley-Geer, D. L. Burke, A. Carnero Rosell, D. Carollo, M. Carrasco Kind, J. Carretero, F. J. Castander, C. E. Cunha, C. B. D'Andrea, L. N. da Costa, T. M. Davis, C. Davis, S. Desai, H. T. Diehl, J. P. Dietrich, S. Dodelson, P. Doel, T. F. Eifler, A. E. Evrard, E. Fernandez, B. Flaugher, P. Fosalba, J. Frieman, J. García-Bellido, E. Gaztanaga, D. W. Gerdes, K. Glazebrook, D. Gruen, R. A. Gruendl, J. Gschwend, G. Gutierrez, W. G. Hartley, S. R. Hinton, K. Honscheid, J. K. Hoormann, B. Jain, D. J. James, M. Jarvis, T. Jeltema, M. W. G. Johnson, M. D. Johnson, A. King, K. Kuehn, S. Kuhlmann, N. Kuropatkin, O. Lahav, G. Lewis, T. S. Li, C. Lidman, M. Lima, H. Lin, E. Macaulay, M. March, J. L. Marshall, P. Martini, P. Melchior, F. Menanteau, R. Miquel, J. J. Mohr, A. Möller, R. C. Nichol, B. Nord, C. R. O'Neill, W. J. Percival, D. Petravick, A. A. Plazas, A. K. Romer, M. Sako, E. Sanchez, V. Scarpine, R. Schindler, M. Schubnell, E. Sheldon, M. Smith, R. C. Smith, M. Soares-Santos, F. Sobreira, N. E. Sommer, E. Suchyta, M. E. C. Swanson, G. Tarle, D. Thomas, B. E. Tucker, D. L. Tucker, S. A. Uddin, V. Vikram, A. R. Walker, R. H. Wechsler, J. Weller, W. Wester, R. C. Wolf, F. Yuan, B. Zhang, and J. Zuntz. Dark energy survey year 1 results: Galaxy clustering for combined probes. *Phys. Rev. D*, 98:042006, Aug 2018. doi: 10.1103/PhysRevD.98.042006. URL https://link.aps.org/doi/10.1103/PhysRevD.98.042006. (Cited at page 136)

T. Erben, H. Hildebrandt, L. Miller, L. van Waerbeke, C. Heymans, H. Hoekstra, T. D. Kitching, Y. Mellier, J. Benjamin, C. Blake, C. Bonnett, O. Cordes, J. Coupon, L. Fu, R. Gavazzi, B. Gillis, E. Grocutt, S. D. J. Gwyn, K. Holhjem, M. J. Hudson, M. Kilbinger, K. Kuijken, M. Milkeraitis, B. T. P. Rowe, T. Schrabback, E. Semboloni, P. Simon, M. Smit, O. Toader, S. Vafaei, E. van Uitert, and M. Velander. CFHTLenS: the Canada-France-Hawaii Telescope Lensing Survey - imaging data and catalogue products. *Monthly Notices of the Royal Astronomical Society*, 433: 2545–2563, August 2013a. doi: 10.1093/mnras/stt928. (Cited at page 19)

T. Erben, H. Hildebrandt, L. Miller, L. van Waerbeke, C. Heymans, H. Hoekstra, T. D. Kitching, Y. Mellier, J. Benjamin, C. Blake, C. Bonnett, O. Cordes, J. Coupon, L. Fu, R. Gavazzi, B. Gillis, E. Grocutt, S. D. J. Gwyn, K. Holhjem, M. J. Hudson, M. Kilbinger, K. Kuijken, M. Milkeraitis, B. T. P. Rowe, T. Schrabback, E. Semboloni, P. Simon, M. Smit, O. Toader, S. Vafaei, E. van Uitert, and M. Velander.

CFHTLenS: the Canada-France-Hawaii Telescope Lensing Survey - imaging data and catalogue products. *Monthly Notices of the Royal Astronomical Society*, 433: 2545–2563, August 2013b. doi: 10.1093/mnras/stt928. (Cited at page 73)

H F. Gruetjen and E P. S. Shellard. Towards efficient and optimal analysis of cmb anisotropies on a masked sky. *Physical Review D*, 89, 12 2012. doi: 10.1103/PhysRevD.89.063008. (Cited at pages 109 e 133)

Zuhui Fan, Huanyuan Shan, and Jiayi Liu. Noisy Weak-lensing Convergence Peak Statistics Near Clusters of Galaxies and Beyond. *The Astrophysical Journal*, 719: 1408–1420, Aug 2010. doi: 10.1088/0004-637X/719/2/1408. (Cited at pages 71 e 85)

Stephen M. Feeney, Matthew C. Johnson, Daniel J. Mortlock, and Hiranya V. Peiris. First Observational Tests of Eternal Inflation: Analysis Methods and WMAP 7-Year Results. *Phys. Rev.*, D84:043507, 2011. doi: 10.1103/PhysRevD.84.043507. (Cited at pages 108 e 132)

A. Ferté, J. Grain, M. Tristram, and R. Stompor. Efficiency of pseudospectrum methods for estimation of the cosmic microwave background B-mode power spectrum. *Phys. Rev.*, D88(2):023524, 2013. doi: 10.1103/PhysRevD.88.023524. (Cited at pages 109 e 133)

B. Flaugher, H. T. Diehl, K. Honscheid, T. M. C. Abbott, O. Alvarez, R. Angstadt, J. T. Annis, M. Antonik, O. Ballester, L. Beaufore, G. M. Bernstein, R. A. Bernstein, B. Bigelow, M. Bonati, D. Boprie, D. Brooks, E. J. Buckley-Geer, J. Campa, L. Cardiel-Sas, F. J. Castander, J. Castilla, H. Cease, J. M. Cela-Ruiz, S. Chappa, E. Chi, C. Cooper, L. N. da Costa, E. Dede, G. Derylo, D. L. DePoy, J. de Vicente, P. Doel, A. Drlica-Wagner, J. Eiting, A. E. Elliott, J. Emes, J. Estrada, A. Fausti Neto, D. A. Finley, R. Flores, J. Frieman, D. Gerdes, M. D. Gladders, B. Gregory, G. R. Gutierrez, J. Hao, S. E. Holland, S. Holm, D. Huffman, C. Jackson, D. J. James, M. Jonas, A. Karcher, I. Karliner, S. Kent, R. Kessler, M. Kozlovsky, R. G. Kron, D. Kubik, K. Kuehn, S. Kuhlmann, K. Kuk, O. Lahav, A. Lathrop, J. Lee, M. E. Levi, P. Lewis, T. S. Li, I. Mandrichenko, J. L. Marshall, G. Martinez, K. W. Merritt, R. Miquel, F. Muñoz, E. H. Neilsen, R. C. Nichol, B. Nord, R. Ogando, J. Olsen,

N. Palaio, K. Patton, J. Peoples, A. A. Plazas, J. Rauch, K. Reil, J.-P. Rheault, N. A. Roe, H. Rogers, A. Roodman, E. Sanchez, V. Scarpine, R. H. Schindler, R. Schmidt, R. Schmitt, M. Schubnell, K. Schultz, P. Schurter, L. Scott, S. Serrano, T. M. Shaw, R. C. Smith, M. Soares-Santos, A. Stefanik, W. Stuermer, E. Suchyta, A. Sypniewski, G. Tarle, J. Thaler, R. Tighe, C. Tran, D. Tucker, A. R. Walker, G. Wang, M. Watson, C. Weaverdyck, W. Wester, R. Woods, B. Yanny, and DES Collaboration. The Dark Energy Camera. 150:150, November 2015. doi: 10.1088/0004-6256/150/5/150. (Cited at page 72)

K. M. Górski, E. Hivon, A. J. Banday, B. D. Wandelt, F. K. Hansen, M. Reinecke, and M. Bartelmann. HEALPix: A Framework for High-Resolution Discretization and Fast Analysis of Data Distributed on the Sphere. *The Astrophysical Journal*, 622: 759–771, April 2005. doi: 10.1086/427976. (Cited at pages 64 e 88)

Amara Graps. An introduction to wavelets. *Computational Science & Engineering, IEEE*, 2(2):50–61, 1995. (Cited at page 65)

A. F. Heavens, Thomas D. Kitching, and A. N. Taylor. Measuring dark energy properties with 3D cosmic shear. *Mon. Not. Roy. Astron. Soc.*, 373:105–120, 2006. doi: 10.1111/j.1365-2966.2006.11006.x. (Cited at page 18)

C. Heymans, L. Van Waerbeke, L. Miller, T. Erben, H. Hildebrandt, H. Hoekstra, T. D. Kitching, Y. Mellier, P. Simon, C. Bonnett, J. Coupon, L. Fu, J. Harnois Déraps, M. J. Hudson, M. Kilbinger, K. Kuijken, B. Rowe, T. Schrabback, E. Semboloni, E. van Uitert, S. Vafaei, and M. Velander. CFHTLenS: the Canada-France-Hawaii Telescope Lensing Survey. 427:146–166, November 2012. doi: 10.1111/j.1365-2966.2012.21952.x. (Cited at page 72)

C. Hikage, M. Takada, T. Hamana, and D. Spergel. Shear power spectrum reconstruction using the pseudo-spectrum method. *Monthly Notices of the Royal Astronomical Society*, 412:65–74, March 2011. doi: 10.1111/j.1365-2966.2010.17886.x. (Cited at pages 52, 109 e 133)

E. Hivon, K. M. Gorski, C. B. Netterfield, B. P. Crill, S. Prunet, and F. Hansen. Master of the cosmic microwave background anisotropy power spectrum: a fast method

for statistical analysis of large and complex cosmic microwave background data sets. *Astrophys. J.*, 567:2, 2002. doi: 10.1086/338126. (Cited at pages 109 e 133)

MP Hobson, AW Jones, and AN Lasenby. Wavelet analysis and the detection of non-gaussianity in the cmb. *Mon. Not. Roy. Astron. Soc.*, 309:125, 1999. doi: 10.1046/j.1365-8711.1999.02824.x. (Cited at pages 108 e 132)

Wayne Hu and Takemi Okamoto. Mass reconstruction with cmb polarization. *Astrophys. J.*, 574:566–574, 2002. doi: 10.1086/341110. (Cited at pages 108 e 132)

Wayne Hu and Martin J. White. Power spectra estimation for weak lensing. *Astrophys. J.*, 554:67–73, 2001. doi: 10.1086/321380. (Cited at page 61)

J. D. Hunter. Matplotlib: A 2d graphics environment. *Computing In Science & Engineering*, 9(3):90–95, 2007. doi: 10.1109/MCSE.2007.55. (Cited at pages 76, 77, 78, 79, 80 e 81)

Bhuvnesh Jain and Ludovic Van Van Waerbeke. Statistics of dark matter halos from gravitational lensing. *Astrophys. J.*, 530:L1, 2000. doi: 10.1086/312480. (Cited at page 84)

M. Jarvis, E. Sheldon, J. Zuntz, T. Kacprzak, S. L. Bridle, A. Amara, R. Armstrong, M. R. Becker, G. M. Bernstein, C. Bonnett, C. Chang, R. Das, J. P. Dietrich, A. Drlica-Wagner, T. F. Eifler, C. Gangkofner, D. Gruen, M. Hirsch, E. M. Huff, B. Jain, S. Kent, D. Kirk, N. MacCrann, P. Melchior, A. A. Plazas, A. Refregier, B. Rowe, E. S. Rykoff, S. Samuroff, C. Sánchez, E. Suchyta, M. A. Troxel, V. Vikram, T. Abbott, F. B. Abdalla, S. Allam, J. Annis, A. Benoit-Lévy, E. Bertin, D. Brooks, E. Buckley-Geer, D. L. Burke, D. Capozzi, A. Carnero Rosell, M. Carrasco Kind, J. Carretero, F. J. Castander, J. Clampitt, M. Crocce, C. E. Cunha, C. B. D'Andrea, L. N. da Costa, D. L. DePoy, S. Desai, H. T. Diehl, P. Doel, A. Fausti Neto, B. Flaugher, P. Fosalba, J. Frieman, E. Gaztanaga, D. W. Gerdes, R. A. Gruendl, G. Gutierrez, K. Honscheid, D. J. James, K. Kuehn, N. Kuropatkin, O. Lahav, T. S. Li, M. Lima, M. March, P. Martini, R. Miquel, J. J. Mohr, E. Neilsen, B. Nord, R. Ogando, K. Reil, A. K. Romer, A. Roodman, M. Sako, E. Sanchez, V. Scarpine, M. Schubnell, I. Sevilla-Noarbe, R. C. Smith, M. Soares-Santos, F. Sobreira, M. E. C. Swanson, G. Tarle, J. Thaler, D. Thomas, A. R. Walker, and R. H. Wechsler. The DES

Science Verification weak lensing shear catalogues. *Monthly Notices of the Royal Astronomical Society*, 460:2245–2281, August 2016. doi: 10.1093/mnras/stw990. (Cited at pages 136 e 137)

B. Joachimi and S. L. Bridle. Simultaneous measurement of cosmology and intrinsic alignments using joint cosmic shear and galaxy number density correlations. *Astronomy & Astrophysics*, 523:A1, November 2010. doi: 10.1051/0004-6361/200913657. (Cited at page 50)

B. Joachimi and P. Schneider. Controlling intrinsic alignments in weak lensing statistics: The nulling and boosting techniques. *ArXiv e-prints*, September 2010. (Cited at page 50)

E. Jullo, J.-P. Kneib, M. Limousin, Á. Elíasdóttir, P. J. Marshall, and T. Verdugo. A Bayesian approach to strong lensing modelling of galaxy clusters. *New Journal of Physics*, 9:447, December 2007. doi: 10.1088/1367-2630/9/12/447. (Cited at page 72)

Eric Jullo, Jean-Paul Kneib, Marceau Limousin, Ardis Eliasdottir, Phil Marshall, and Tomas Verdugo. A Bayesian approach to strong lensing modelling of galaxy clusters. *New J. Phys.*, 9:447, 2007. doi: 10.1088/1367-2630/9/12/447. (Cited at pages 108 e 133)

T. Kacprzak, D. Kirk, O. Friedrich, A. Amara, A. Refregier, L. Marian, J. P. Dietrich, E. Suchyta, J. Aleksić, D. Bacon, M. R. Becker, C. Bonnett, S. L. Bridle, C. Chang, T. F. Eifler, W. G. Hartley, E. M. Huff, E. Krause, N. MacCrann, P. Melchior, A. Nicola, S. Samuroff, E. Sheldon, M. A. Troxel, J. Weller, J. Zuntz, T. M. C. Abbott, F. B. Abdalla, R. Armstrong, A. Benoit-Lévy, G. M. Bernstein, R. A. Bernstein, E. Bertin, D. Brooks, D. L. Burke, A. Carnero Rosell, M. Carrasco Kind, J. Carretero, F. J. Castander, M. Crocce, C. B. D'Andrea, L. N. da Costa, S. Desai, H. T. Diehl, A. E. Evrard, A. F. Neto, B. Flaugher, P. Fosalba, J. Frieman, D. W. Gerdes, D. A. Goldstein, D. Gruen, R. A. Gruendl, G. Gutierrez, K. Honscheid, B. Jain, D. J. James, M. Jarvis, K. Kuehn, N. Kuropatkin, O. Lahav, M. Lima, M. March, J. L. Marshall, P. Martini, C. J. Miller, R. Miquel, J. J. Mohr, R. C. Nichol, B. Nord, A. A. Plazas, A. K. Romer, A. Roodman, E. S. Rykoff, E. Sanchez, V. Scarpine, M. Schubnell,

I. Sevilla-Noarbe, R. C. Smith, M. Soares-Santos, F. Sobreira, M. E. C. Swanson, G. Tarle, D. Thomas, V. Vikram, A. R. Walker, Y. Zhang, and DES Collaboration. Cosmology constraints from shear peak statistics in Dark Energy Survey Science Verification data. *Monthly Notices of the Royal Astronomical Society*, 463:3653–3673, December 2016a. doi: 10.1093/mnras/stw2070. (Cited at pages 62 e 71)

T. Kacprzak, D. Kirk, O. Friedrich, A. Amara, A. Refregier, L. Marian, J. P. Dietrich, E. Suchyta, J. Aleksić, D. Bacon, M. R. Becker, C. Bonnett, S. L. Bridle, C. Chang, T. F. Eifler, W. G. Hartley, E. M. Huff, E. Krause, N. MacCrann, P. Melchior, A. Nicola, S. Samuroff, E. Sheldon, M. A. Troxel, J. Weller, J. Zuntz, T. M. C. Abbott, F. B. Abdalla, R. Armstrong, A. Benoit-Lévy, G. M. Bernstein, R. A. Bernstein, E. Bertin, D. Brooks, D. L. Burke, A. Carnero Rosell, M. Carrasco Kind, J. Carretero, F. J. Castander, M. Crocce, C. B. D'Andrea, L. N. da Costa, S. Desai, H. T. Diehl, A. E. Evrard, A. F. Neto, B. Flaugher, P. Fosalba, J. Frieman, D. W. Gerdes, D. A. Goldstein, D. Gruen, R. A. Gruendl, G. Gutierrez, K. Honscheid, B. Jain, D. J. James, M. Jarvis, K. Kuehn, N. Kuropatkin, O. Lahav, M. Lima, M. March, J. L. Marshall, P. Martini, C. J. Miller, R. Miquel, J. J. Mohr, R. C. Nichol, B. Nord, A. A. Plazas, A. K. Romer, A. Roodman, E. S. Rykoff, E. Sanchez, V. Scarpine, M. Schubnell, I. Sevilla-Noarbe, R. C. Smith, M. Soares-Santos, F. Sobreira, M. E. C. Swanson, G. Tarle, D. Thomas, V. Vikram, A. R. Walker, Y. Zhang, and DES Collaboration. Cosmology constraints from shear peak statistics in Dark Energy Survey Science Verification data. *Monthly Notices of the Royal Astronomical Society*, 463:3653–3673, December 2016b. doi: 10.1093/mnras/stw2070. (Cited at page 72)

N. Kaiser and G. Squires. Mapping the dark matter with weak gravitational lensing. *The Astrophysical Journal*, 404:441–450, February 1993. doi: 10.1086/172297. (Cited at pages 53, 71, 75, 108 e 132)

M. Kerscher, J. Schmalzing, J. Retzlaff, S. Borgani, T. Buchert, S. Gottlöber, V. Müller, M. Plionis, and H. Wagner. Minkowski functionals of Abell/ACO clusters. *Monthly Notices of the Royal Astronomical Society*, 284:73–84, January 1997. doi: 10.1093/mnras/284.1.73. (Cited at page 63)

M. Kilbinger. Cosmology with cosmic shear observations: a review. *Reports on*

Progress in Physics, 78(8):086901, July 2015. doi: 10.1088/0034-4885/78/8/086901. (Cited at page 70)

M. Kilbinger, P. Schneider, and T. Eifler. E- and B-mode mixing from incomplete knowledge of the shear correlation. *Astronomy and Astrophysics*, 457:15–19, October 2006. doi: 10.1051/0004-6361:20065495. (Cited at page 70)

Martin Kilbinger. Cosmology with cosmic shear observations: a review. *Rept. Prog. Phys.*, 78:086901, 2015. doi: 10.1088/0034-4885/78/8/086901. (Cited at pages 40, 49 e 112)

J. Kim. How to make a clean separation between CMB E and B modes with proper foreground masking. *Astronomy and Astrophysics*, 531:A32, July 2011. doi: 10.1051/0004-6361/201116733. (Cited at pages 110, 113 e 133)

T. D. Kitching, A. F. Heavens, and L. Miller. 3D photometric cosmic shear. *Mon. Not. Roy. Astron. Soc.*, 413:2923–2934, June 2011. doi: 10.1111/j.1365-2966.2011.18369.x. (Cited at pages 49 e 177)

T. D. Kitching et al. 3D Cosmic Shear: Cosmology from CFHTLenS. *Mon. Not. Roy. Astron. Soc.*, 442(2):1326–1349, 2014. doi: 10.1093/mnras/stu934. (Cited at page 53)

E. Komatsu, K. M. Smith, J. Dunkley, C. L. Bennett, B. Gold, G. Hinshaw, N. Jarosik, D. Larson, M. R. Nolta, L. Page, D. N. Spergel, M. Halpern, R. S. Hill, A. Kogut, M. Limon, S. S. Meyer, N. Odegard, G. S. Tucker, J. L. Weiland, E. Wollack, and E. L. Wright. Seven-year Wilkinson Microwave Anisotropy Probe (WMAP) Observations: Cosmological Interpretation. *Astrophysical Journal Supplement*, 192:18, February 2011. doi: 10.1088/0067-0049/192/2/18. (Cited at page 25)

J. M. Kratochvil, Z. Haiman, and M. May. Probing cosmology with weak lensing peak counts. *Physical Review D*, 81(4):043519, February 2010. doi: 10.1103/PhysRevD.81.043519. (Cited at pages 71 e 85)

J. M. Kratochvil, E. A. Lim, S. Wang, Z. Haiman, M. May, and K. Huffenberger. Probing cosmology with weak lensing Minkowski functionals. *Physical Review D*, 85(10):103513, May 2012. doi: 10.1103/PhysRevD.85.103513. (Cited at page 74)

Guido Kruse and Peter Schneider. Statistics of dark matter haloes expected from weak lensing surveys. *Mon. Not. Roy. Astron. Soc.*, 302:821, 1999. doi: 10.1046/j.1365-8711.1999.02195.x. (Cited at page 84)

Guido Kruse and Peter Schneider. The nonGaussian tail of cosmic-shear statistics. *Mon. Not. Roy. Astron. Soc.*, 318:321, 2000. doi: 10.1046/j.1365-8711.2000.03389.x. (Cited at page 84)

F. Lanusse, J.-L. Starck, A. Leonard, and S. Pires. High resolution weak lensing mass mapping combining shear and flexion. 591:A2, June 2016. doi: 10.1051/0004-6361/201628278. (Cited at page 72)

R. Laureijs, J. Amiaux, S. Arduini, J. . Augueres, J. Brinchmann, R. Cole, M. Cropper, C. Dabin, L. Duvet, A. Ealet, and et al. Euclid Definition Study Report. *ArXiv e-prints*, October 2011. (Cited at pages 13, 17, 70, 73, 110, 119, 120 e 134)

B. Leistedt, J. D. McEwen, P. Vandergheynst, and Y. Wiaux. S2LET: A code to perform fast wavelet analysis on the sphere. *Astronomy & Astrophysics*, 558:A128, October 2013. doi: 10.1051/0004-6361/201220729. (Cited at page 67)

Boris Leistedt, Jason D. McEwen, Thomas D. Kitching, and Hiranya V. Peiris. 3D weak lensing with spin wavelets on the ball. *Phys. Rev.*, D92(12):123010, 2015. doi: 10.1103/PhysRevD.92.123010. (Cited at page 66)

Boris Leistedt, Jason D. McEwen, Martin Büttner, and Hiranya V. Peiris. Wavelet reconstruction of E and B modes for CMB polarization and cosmic shear analyses. *Mon. Not. Roy. Astron. Soc.*, 466(3):3728–3740, 2017. doi: 10.1093/mnras/stw3176. (Cited at pages 65, 109, 110, 113, 114, 115, 116, 117, 119, 129 e 133)

Pablo Lemos, Anthony Challinor, and George Efstathiou. The effect of Limber and flat-sky approximations on galaxy weak lensing. *JCAP*, 1705(05):014, 2017. doi: 10.1088/1475-7516/2017/05/014. (Cited at pages 49 e 177)

A. Leonard, F.-X. Dupé, and J.-L. Starck. A compressed sensing approach to 3D weak lensing. *Astronomy and Astrophysics*, 539:A85, March 2012. doi: 10.1051/0004-6361/201117642. (Cited at page 72)

A. Leonard, F. Lanusse, and J.-L. Starck. GLIMPSE: accurate 3D weak lensing reconstructions using sparsity. *Monthly Notices of the Royal Astronomical Society*, 440:1281–1294, May 2014. doi: 10.1093/mnras/stu273. (Cited at page 72)

Adrienne Leonard, François Lanusse, and Jean-Luc Starck. GLIMPSE: Accurate 3D weak lensing reconstructions using sparsity. *Mon. Not. Roy. Astron. Soc.*, 440(2): 1281–1294, 2014. doi: 10.1093/mnras/stu273. (Cited at pages 108 e 132)

Antony Lewis. Harmonic E/B decomposition for CMB polarization maps. *Phys. Rev.*, D68:083509, 2003. doi: 10.1103/PhysRevD.68.083509. (Cited at pages 109 e 133)

Antony Lewis, Anthony Challinor, and Neil Turok. Analysis of CMB polarization on an incomplete sky. *Phys. Rev.*, D65:023505, 2002. doi: 10.1103/PhysRevD.65.023505. (Cited at pages 109 e 133)

D. N. Limber. The Analysis of Counts of the Extragalactic Nebulae in Terms of a Fluctuating Density Field. *The Astrophysical Journal*, 117:134, January 1953. doi: 10.1086/145672. (Cited at pages 49 e 177)

C.-A. Lin and M. Kilbinger. A new model to predict weak-lensing peak counts. I. Comparison with N-body simulations. *Astronomy and Astrophysics*, 576:A24, April 2015a. doi: 10.1051/0004-6361/201425188. (Cited at pages 61, 62, 71 e 85)

C.-A. Lin and M. Kilbinger. A new model to predict weak-lensing peak counts. II. Parameter constraint strategies. *Astronomy and Astrophysics*, 583:A70, November 2015b. doi: 10.1051/0004-6361/201526659. (Cited at pages 62, 71 e 85)

Chieh-An Lin and Martin Kilbinger. A new model to predict weak-lensing peak counts I. Comparison with N-body Simulations. *Astron. Astrophys.*, 576:A24, 2015a. doi: 10.1051/0004-6361/201425188. (Cited at pages 108 e 132)

Chieh-An Lin and Martin Kilbinger. A new model to predict weak-lensing peak counts II. Parameter constraint strategies. *Astron. Astrophys.*, 583:A70, 2015b. doi: 10.1051/0004-6361/201526659. (Cited at pages 108 e 132)

Chieh-An Lin and Martin Kilbinger. Quantifying systematics from the shear inversion on weak-lensing peak counts. *Astron. Astrophys.*, 614:A36, 2018. doi: 10.1051/0004-6361/201730872. (Cited at pages 62 e 71)

Chieh-An Lin, Martin Kilbinger, and Sandrine Pires. A new model to predict weak-lensing peak counts III. Filtering technique comparisons. *Astron. Astrophys.*, 593: A88, 2016. doi: 10.1051/0004-6361/201628565. (Cited at page 85)

J. Liu and J. C. Hill. Cross-correlation of Planck CMB lensing and CFHTLenS galaxy weak lensing maps. *Physical Review D*, 92(6):063517, September 2015. doi: 10.1103/PhysRevD.92.063517. (Cited at page 74)

Marilena LoVerde and Niayesh Afshordi. Extended Limber Approximation. *Phys. Rev.*, D78:123506, 2008. doi: 10.1103/PhysRevD.78.123506. (Cited at pages 49, 51 e 177)

LSST Science Collaboration, P. A. Abell, J. Allison, S. F. Anderson, J. R. Andrew, J. R. P. Angel, L. Armus, D. Arnett, S. J. Asztalos, T. S. Axelrod, and et al. LSST Science Book, Version 2.0. *ArXiv e-prints*, December 2009. (Cited at pages 17, 70, 73, 110 e 134)

L. Marian, R. E. Smith, and G. M. Bernstein. The Cosmology Dependence of Weak Lensing Cluster Counts. *The Astrophysical Journal Letters*, 698:L33–L36, June 2009. doi: 10.1088/0004-637X/698/1/L33. (Cited at pages 62 e 71)

L. Marian, R. E. Smith, S. Hilbert, and P. Schneider. Optimized detection of shear peaks in weak lensing maps. *Monthly Notices of the Royal Astronomical Society*, 423: 1711–1725, June 2012. doi: 10.1111/j.1365-2966.2012.20992.x. (Cited at page 86)

G. A. Marques, C. P. Novaes, A. Bernui, and I. S. Ferreira. Isotropy analyses of the Planck convergence map. *Mon. Not. Roy. Astron. Soc.*, 473(1):165–172, 2018. doi: 10.1093/mnras/stx2240. (Cited at page 61)

R. Massey, J. Rhodes, R. Ellis, N. Scoville, A. Leauthaud, A. Finoguenov, P. Capak, D. Bacon, H. Aussel, J.-P. Kneib, A. Koekemoer, H. McCracken, B. Mobasher, S. Pires, A. Refregier, S. Sasaki, J.-L. Starck, Y. Taniguchi, A. Taylor, and J. Taylor. Dark matter maps reveal cosmic scaffolding. 445:286–290, January 2007. doi: 10.1038/nature05497. (Cited at page 72)

R. Massey, L. Williams, R. Smit, M. Swinbank, T. D. Kitching, D. Harvey, M. Jauzac, H. Israel, D. Clowe, A. Edge, M. Hilton, E. Jullo, A. Leonard, J. Liesenborgs, J. Merten, I. Mohammed, D. Nagai, J. Richard, A. Robertson, P. Saha, R. Santana, J. Stott, and E. Tittley. The behaviour of dark matter associated with four bright cluster galaxies in the 10 kpc core of Abell 3827. 449:3393–3406, June 2015. doi: 10.1093/mnras/stv467. (Cited at page 72)

Richard Massey et al. Weak lensing from space. 2. Dark matter mapping. *Astron. J.*, 127:3089, 2004. doi: 10.1086/420985. (Cited at page 72)

T. Matsubara and B. Jain. The Topology of Weak Lensing Fields. *The Astrophysical Journal Letters*, 552:L89–L92, May 2001. doi: 10.1086/320327. (Cited at pages 71 e 74)

Takahiko Matsubara. Statistics of smoothed cosmic fields in perturbation theory. i. formulation and useful formulae in second-order perturbation theory. *The Astrophysical Journal*, 584(1):1–33, feb 2003. doi: 10.1086/345521. URL https://doi.org/10.1086/345521. (Cited at page 138)

M. Maturi, C. Angrick, F. Pace, and M. Bartelmann. An analytic approach to number counts of weak-lensing peak detections. *Astronomy and Astrophysics*, 519:A23, September 2010. doi: 10.1051/0004-6361/200912866. (Cited at page 85)

J. D. McEwen and Y. Wiaux. A Novel Sampling Theorem on the Sphere. *IEEE Transactions on Signal Processing*, 59:5876–5887, December 2011a. doi: 10.1109/TSP.2011.2166394. (Cited at page 121)

J. D. McEwen and Y. Wiaux. A Novel Sampling Theorem on the Sphere. *IEEE Transactions on Signal Processing*, 59:5876–5887, December 2011b. doi: 10.1109/TSP.2011.2166394. (Cited at pages 64, 67, 72, 82, 89, 94 e 140)

J. D. McEwen, B. Leistedt, M. Büttner, H. V. Peiris, and Y. Wiaux. Directional spin wavelets on the sphere. *arXiv e-prints*, September 2015. (Cited at pages 65, 68, 116 e 121)

Jason D. McEwen, Claudio Durastanti, and Yves Wiaux. Localisation of directional scale-discretised wavelets on the sphere. *Applied and Computational Harmonic*

Analysis, 44(1):59 – 88, 2018. ISSN 1063-5203. doi: https://doi.org/10.1016/j.acha.2016.03.009. URL http://www.sciencedirect.com/science/article/pii/S1063520316000324. (Cited at pages 65 e 116)

K. R. Mecke, T. Buchert, and H. Wagner. Robust morphological measures for large scale structure in the universe. *Astron. Astrophys.*, 288:697–704, 1994a. (Cited at pages 61, 63, 71 e 74)

K. R. Mecke, T. Buchert, and H. Wagner. Robust morphological measures for large scale structure in the universe. *Astron. Astrophys.*, 288:697–704, 1994b. (Cited at pages 108 e 132)

D. Munshi, L. van Waerbeke, J. Smidt, and P. Coles. From weak lensing to non-Gaussianity via Minkowski functionals. *Monthly Notices of the Royal Astronomical Society*, 419:536–555, January 2012. doi: 10.1111/j.1365-2966.2011.19718.x. (Cited at pages 61, 63, 71, 74 e 87)

Toshiya Namikawa, Daisuke Yamauchi, and Atsushi Taruya. Full-sky lensing reconstruction of gradient and curl modes from CMB maps. *JCAP*, 1201:007, 2012. doi: 10.1088/1475-7516/2012/01/007. (Cited at pages 108, 109 e 132)

J. P. Ostriker and P. J. E. Peebles. A Numerical Study of the Stability of Flattened Galaxies: or, can Cold Galaxies Survive? *Astrophysical Journal*, 186:467–480, December 1973. doi: 10.1086/152513. (Cited at page 24)

J. P. Ostriker, P. J. E. Peebles, and A. Yahil. The size and mass of galaxies, and the mass of the universe. *Astrophysical Journal*, 193:L1–L4, October 1974. doi: 10.1086/181617. (Cited at page 24)

S. Paulin-Henriksson, A. Amara, L. Voigt, A. Refregier, and S. L. Bridle. Requirements on PSF Calibration for Dark Energy from Cosmic Shear. *Astron. Astrophys.*, 484:67, 2008. doi: 10.1051/0004-6361:20079150. (Cited at page 50)

R. Pearson and O. Zahn. Cosmology from cross correlation of CMB lensing and galaxy surveys. *Physical Review D*, 89(4):043516, February 2014. doi: 10.1103/PhysRevD.89.043516. (Cited at page 74)

P. J. E. Peebles. *Principles of Physical Cosmology*. 1993. (Cited at page 34)

A. Peel, C.-A. Lin, F. Lanusse, A. Leonard, J.-L. Starck, and M. Kilbinger. Cosmological constraints with weak-lensing peak counts and second-order statistics in a large-field survey. *Astronomy and Astrophysics*, 599:A79, March 2017. doi: 10.1051/0004-6361/201629928. (Cited at pages 62 e 71)

Ue-Li Pen, Ludovic van Waerbeke, and Yannick Mellier. Gravity and non-gravity modes in the virmos-descart weak lensing survey. *Astrophys. J.*, 567:31, 2002. doi: 10.1086/338576. (Cited at pages 109 e 133)

S. Perlmutter et al. Measurements of Omega and Lambda from 42 high redshift supernovae. *Astrophys. J.*, 517:565–586, 1999. doi: 10.1086/307221. (Cited at pages 24 e 26)

M. Persic, P. Salucci, and F. Stel. The universal rotation curve of spiral galaxies - I. The dark matter connection. *Monthly Notices of the Royal Astronomical Society*, 281: 27–47, July 1996. doi: 10.1093/mnras/281.1.27. (Cited at page 24)

A. Petri, Z. Haiman, L. Hui, M. May, and J. M. Kratochvil. Cosmology with Minkowski functionals and moments of the weak lensing convergence field. *Physical Review D*, 88(12):123002, December 2013. doi: 10.1103/PhysRevD.88.123002. (Cited at pages 62, 63, 64, 74 e 87)

J. Pielorz, J. Rödiger, I. Tereno, and P. Schneider. A fitting formula for the non-Gaussian contribution to the lensing power spectrum covariance. *Astronomy and Astrophysics*, 514:A79, May 2010a. doi: 10.1051/0004-6361/200912854. (Cited at pages 61, 108 e 132)

J. Pielorz, J. Rödiger, I. Tereno, and P. Schneider. A fitting formula for the non-Gaussian contribution to the lensing power spectrum covariance. *Astronomy and Astrophysics*, 514:A79, May 2010b. doi: 10.1051/0004-6361/200912854. (Cited at page 70)

S. Pires, J.-L. Starck, A. Amara, A. Réfrégier, and R. Teyssier. Cosmological model discrimination from weak lensing data. In J.-M. Alimi and A. Fuözfa, editors, *American Institute of Physics Conference Series*, volume 1241 of *American Institute of Physics Conference Series*, pages 1118–1127, June 2010a. doi: 10.1063/1.3462608. (Cited at pages 108 e 132)

S. Pires, J.-L. Starck, A. Amara, A. Réfrégier, and R. Teyssier. Cosmological model discrimination from weak lensing data. In J.-M. Alimi and A. Fuözfa, editors, *American Institute of Physics Conference Series*, volume 1241 of *American Institute of Physics Conference Series*, pages 1118–1127, June 2010b. doi: 10.1063/1.3462608. (Cited at page 71)

J. Prat et al. Cosmological lensing ratios with DES Y1, SPT and Planck. *Submitted to: Mon. Not. Roy. Astron. Soc.*, 2018. (Cited at page 136)

Matthew A. Price, Xiaohao Cai, Jason D. McEwen, and Thomas D. Kitching. Sparse Bayesian mass-mapping with uncertainties: peak statistics and feature locations. 2018a. (Cited at page 108)

Matthew A. Price, Xiaohao Cai, Jason D. McEwen, Marcelo Pereyra, and Thomas D. Kitching. Sparse Bayesian mass-mapping with uncertainties: local credible intervals. 2018b. (Cited at page 108)

Matthew A. Price, Jason D. McEwen, Xiaohao Cai, Thomas D. Kitching, and Christopher G. R. Wallis. Sparse Bayesian mass-mapping with uncertainties: hypothesis testing of structure. 2018c. (Cited at page 108)

Katrin Reblinsky, Guido Kruse, Bhuvnesh Jain, and Peter Schneider. Cosmic shear and halo abundances: analytical versus numerical results. *Astron. Astrophys.*, 351: 815–826, 1999. (Cited at page 84)

Alexandre Refregier. Weak gravitational lensing by large scale structure. *Ann. Rev. Astron. Astrophys.*, 41:645–668, 2003. doi: 10.1146/annurev.astro.41.111302.102207. (Cited at pages 108 e 132)

Adam G. Riess et al. Observational evidence from supernovae for an accelerating universe and a cosmological constant. *Astron. J.*, 116:1009–1038, 1998. doi: 10.1086/300499. (Cited at pages 24 e 26)

Leszek Roszkowski, Enrico Maria Sessolo, and Sebastian Trojanowski. WIMP dark matter candidates and searches—current status and future prospects. *Rept. Prog. Phys.*, 81(6):066201, 2018. doi: 10.1088/1361-6633/aab913. (Cited at page 24)

J. Sato, K. Umetsu, T. Futamase, and T. Yamada. The Topology of a Weak Lensing Field in the Neighborhood of MS 1054-03. *The Astrophysical Journal Letters*, 582: L67–L70, January 2003. doi: 10.1086/367717. (Cited at page 74)

J. Schmalzing and T. Buchert. Beyond Genus Statistics: A Unifying Approach to the Morphology of Cosmic Structure. *The Astrophysical Journal Letters*, 482:L1–L4, June 1997. doi: 10.1086/310680. (Cited at pages 63, 74 e 87)

Jens Schmalzing, Martin Kerscher, and Thomas Buchert. Minkowski functionals in cosmology. *Proc. Int. Sch. Phys. Fermi*, 132:281–291, 1996. doi: 10.3254/978-1-61499-217-2-281. (Cited at page 62)

P. Schneider. Detection of (dark) matter concentrations via weak gravitational lensing. *Monthly Notices of the Royal Astronomical Society*, 283:837–853, December 1996. doi: 10.1093/mnras/283.3.837. (Cited at page 86)

P. Schneider and C. Seitz. Steps towards nonlinear cluster inversion through gravitational distortions. 1: Basic considerations and circular clusters. *Astronomy & Astrophysics*, 294:411–431, February 1995. (Cited at page 45)

P. Schneider, T. Eifler, and E. Krause. COSEBIs: Extracting the full E-/B-mode information from cosmic shear correlation functions. *Astronomy and Astrophysics*, 520:A116, September 2010. doi: 10.1051/0004-6361/201014235. (Cited at pages 108, 109, 132 e 133)

N. Scoville, H. Aussel, M. Brusa, P. Capak, C. M. Carollo, M. Elvis, M. Giavalisco, L. Guzzo, G. Hasinger, C. Impey, J.-P. Kneib, O. LeFevre, S. J. Lilly, B. Mobasher, A. Renzini, R. M. Rich, D. B. Sanders, E. Schinnerer, D. Schminovich, P. Shopbell, Y. Taniguchi, and N. D. Tyson. The Cosmic Evolution Survey (COSMOS): Overview. 172:1–8, September 2007. doi: 10.1086/516585. (Cited at page 72)

M. Shirasaki. Statistical connection of peak counts to power spectrum and moments in weak-lensing field. *Monthly Notices of the Royal Astronomical Society*, 465:1974–1983, February 2017. doi: 10.1093/mnras/stw2950. (Cited at pages 62, 71, 85 e 86)

P. Simon. Improving three-dimensional mass mapping with weak gravitational lensing using galaxy clustering. *Astronomy and Astrophysics*, 560:A33, December 2013. doi: 10.1051/0004-6361/201219257. (Cited at page 72)

P. Simon, A. N. Taylor, and J. Hartlap. Unfolding the matter distribution using three-dimensional weak gravitational lensing. *Monthly Notices of the Royal Astronomical Society*, 399:48–68, October 2009. doi: 10.1111/j.1365-2966.2009.15246.x. (Cited at page 72)

Kendrick M. Smith. Pseudo-c(l) estimators which do not mix e and b modes. *Phys. Rev.*, D74:083002, 2006a. doi: 10.1103/PhysRevD.74.083002. (Cited at pages 109 e 133)

Kendrick M. Smith. Pure pseudo-C_l estimators for CMB B-modes. *New Astron. Rev.*, 50:1025–1029, 2006b. doi: 10.1016/j.newar.2006.09.015. (Cited at pages 110 e 133)

Kendrick M. Smith and Matias Zaldarriaga. A general solution to the E-B mixing problem. *Phys. Rev.*, D76:043001, 2007. doi: 10.1103/PhysRevD.76.043001. (Cited at pages 109 e 133)

G. F. Smoot, C. L. Bennett, A. Kogut, E. L. Wright, J. Aymon, N. W. Boggess, E. S. Cheng, G. de Amici, S. Gulkis, M. G. Hauser, G. Hinshaw, P. D. Jackson, M. Janssen, E. Kaita, T. Kelsall, P. Keegstra, C. Lineweaver, K. Loewenstein, P. Lubin, J. Mather, S. S. Meyer, S. H. Moseley, T. Murdock, L. Rokke, R. F. Silverberg, L. Tenorio, R. Weiss, and D. T. Wilkinson. Structure in the COBE differential microwave radiometer first-year maps. *Astrophysical Journal Letters*, 396:L1–L5, September 1992. doi: 10.1086/186504. (Cited at page 25)

D. Spergel, N. Gehrels, J. Breckinridge, M. Donahue, A. Dressler, B. S. Gaudi, T. Greene, O. Guyon, C. Hirata, J. Kalirai, N. J. Kasdin, W. Moos, S. Perlmutter, M. Postman, B. Rauscher, J. Rhodes, Y. Wang, D. Weinberg, J. Centrella, W. Traub, C. Baltay, J. Colbert, D. Bennett, A. Kiessling, B. Macintosh, J. Merten, M. Mortonson, M. Penny, E. Rozo, D. Savransky, K. Stapelfeldt, Y. Zu, C. Baker, E. Cheng, D. Content, J. Dooley, M. Foote, R. Goullioud, K. Grady, C. Jackson, J. Kruk, M. Levine, M. Melton, C. Peddie, J. Ruffa, and S. Shaklan. Wide-Field InfraRed

Survey Telescope-Astrophysics Focused Telescope Assets WFIRST-AFTA Final Report. *ArXiv e-prints*, May 2013. (Cited at pages 70, 110 e 134)

M. Takada and B. Jain. The impact of non-Gaussian errors on weak lensing surveys. *Monthly Notices of the Royal Astronomical Society*, 395:2065–2086, June 2009. doi: 10.1111/j.1365-2966.2009.14504.x. (Cited at page 70)

Masahiro Takada and Bhuvnesh Jain. The impact of non-gaussian errors on weak lensing surveys. *Monthly Notices of the Royal Astronomical Society*, 395(4):2065–2086, 2009a. ISSN 1365-2966. doi: 10.1111/j.1365-2966.2009.14504.x. URL http://dx.doi.org/10.1111/j.1365-2966.2009.14504.x. (Cited at page 61)

Masahiro Takada and Bhuvnesh Jain. The Impact of Non-Gaussian Errors on Weak Lensing Surveys. *Mon. Not. Roy. Astron. Soc.*, 395:2065–2086, 2009b. doi: 10.1111/j.1365-2966.2009.14504.x. (Cited at pages 108 e 132)

A. N. Taylor. Imaging the 3-d cosmological mass distribution with weak gravitational lensing. 2001. (Cited at page 108)

Andy N. Taylor, D. J. Bacon, M. E. Gray, C. Wolf, K. Meisenheimer, S. Dye, A. Borch, M. Kleinheinrich, Z. Kovacs, and L. Wisotzki. Mapping the 3-D dark matter with weak lensing in COMBO-17. *Mon. Not. Roy. Astron. Soc.*, 353:1176, 2004. doi: 10.1111/j.1365-2966.2004.08138.x. (Cited at pages 72, 108 e 132)

Peter L. Taylor, Thomas D. Kitching, Justing Alsing, Benjamin D. Wandelt, Stephen M. Feeney, and Jason D. McEwen. Cosmic Shear: Inference from Forward Models. 2019. (Cited at page 119)

The Dark Energy Survey Collaboration. The Dark Energy Survey. *ArXiv Astrophysics e-prints*, October 2005. (Cited at pages 70 e 73)

Hiroyuki Tomita. Curvature Invariants of Random Interface Generated by Gaussian Fields. *Progress of Theoretical Physics*, 76(4):952–955, 10 1986. ISSN 0033-068X. doi: 10.1143/PTP.76.952. URL https://dx.doi.org/10.1143/PTP.76.952. (Cited at page 139)

M. A. Troxel and Mustapha Ishak. The Intrinsic Alignment of Galaxies and its

Impact on Weak Gravitational Lensing in an Era of Precision Cosmology. *Phys. Rept.*, 558:1–59, 2014. doi: 10.1016/j.physrep.2014.11.001. (Cited at page 50)

M. A. Troxel, N. MacCrann, J. Zuntz, T. F. Eifler, E. Krause, S. Dodelson, D. Gruen, J. Blazek, O. Friedrich, S. Samuroff, J. Prat, L. F. Secco, C. Davis, A. Ferté, J. DeRose, A. Alarcon, A. Amara, E. Baxter, M. R. Becker, G. M. Bernstein, S. L. Bridle, R. Cawthon, C. Chang, A. Choi, J. De Vicente, A. Drlica-Wagner, J. Elvin-Poole, J. Frieman, M. Gatti, W. G. Hartley, K. Honscheid, B. Hoyle, E. M. Huff, D. Huterer, B. Jain, M. Jarvis, T. Kacprzak, D. Kirk, N. Kokron, C. Krawiec, O. Lahav, A. R. Liddle, J. Peacock, M. M. Rau, A. Refregier, R. P. Rollins, E. Rozo, E. S. Rykoff, C. Sánchez, I. Sevilla-Noarbe, E. Sheldon, A. Stebbins, T. N. Varga, P. Vielzeuf, M. Wang, R. H. Wechsler, B. Yanny, T. M. C. Abbott, F. B. Abdalla, S. Allam, J. Annis, K. Bechtol, A. Benoit-Lévy, E. Bertin, D. Brooks, E. Buckley-Geer, D. L. Burke, A. Carnero Rosell, M. Carrasco Kind, J. Carretero, F. J. Castander, M. Crocce, C. E. Cunha, C. B. D'Andrea, L. N. da Costa, D. L. DePoy, S. Desai, H. T. Diehl, J. P. Dietrich, P. Doel, E. Fernandez, B. Flaugher, P. Fosalba, J. García-Bellido, E. Gaztanaga, D. W. Gerdes, T. Giannantonio, D. A. Goldstein, R. A. Gruendl, J. Gschwend, G. Gutierrez, D. J. James, T. Jeltema, M. W. G. Johnson, M. D. Johnson, S. Kent, K. Kuehn, S. Kuhlmann, N. Kuropatkin, T. S. Li, M. Lima, H. Lin, M. A. G. Maia, M. March, J. L. Marshall, P. Martini, P. Melchior, F. Menanteau, R. Miquel, J. J. Mohr, E. Neilsen, R. C. Nichol, B. Nord, D. Petravick, A. A. Plazas, A. K. Romer, A. Roodman, M. Sako, E. Sanchez, V. Scarpine, R. Schindler, M. Schubnell, M. Smith, R. C. Smith, M. Soares-Santos, F. Sobreira, E. Suchyta, M. E. C. Swanson, G. Tarle, D. Thomas, D. L. Tucker, V. Vikram, A. R. Walker, J. Weller, and Y. Zhang. Dark energy survey year 1 results: Cosmological constraints from cosmic shear. *Phys. Rev. D*, 98:043528, Aug 2018. doi: 10.1103/PhysRevD.98.043528. URL https://link.aps.org/doi/10.1103/PhysRevD.98.043528. (Cited at page 136)

Shinji Tsujikawa. Introductory review of cosmic inflation. In *2nd Tah Poe School on Cosmology: Modern Cosmology Phitsanulok, Thailand, April 17-25, 2003*, 2003. (Cited at page 25)

Shinji Tsujikawa. Quintessence: A Review. *Class. Quant. Grav.*, 30:214003, 2013. doi: 10.1088/0264-9381/30/21/214003. (Cited at page 35)

Z. M. Vallis, C. G. R. Wallis, and T. D. Kitching. On the effect of projections on convergence peak counts and Minkowski functionals. *Astronomy and Computing*, 24:84–96, July 2018. doi: 10.1016/j.ascom.2018.06.004. (Cited at pages 110 e 134)

L. Van Waerbeke, J. Benjamin, T. Erben, C. Heymans, H. Hildebrandt, H. Hoekstra, T. D. Kitching, Y. Mellier, L. Miller, J. Coupon, J. Harnois-Déraps, L. Fu, M. Hudson, M. Kilbinger, K. Kuijken, B. Rowe, T. Schrabback, E. Semboloni, S. Vafaei, E. van Uitert, and M. Velander. CFHTLenS: mapping the large-scale structure with gravitational lensing. 433:3373–3388, August 2013. doi: 10.1093/mnras/stt971. (Cited at page 72)

Ludovic Van Waerbeke. Noise properties of gravitational lens mass reconstruction. *Mon. Not. Roy. Astron. Soc.*, 313:524–532, 2000. doi: 10.1046/j.1365-8711.2000.03259.x. (Cited at page 84)

Ludovic Van Waerbeke et al. CFHTLenS: Mapping the Large Scale Structure with Gravitational Lensing. *Mon. Not. Roy. Astron. Soc.*, 433:3373, 2013. doi: 10.1093/mnras/stt971. (Cited at page 110)

J. T. VanderPlas, A. J. Connolly, B. Jain, and M. Jarvis. Three-dimensional Reconstruction of the Density Field: An SVD Approach to Weak-lensing Tomography. *The Astrophysical Journal*, 727:118, February 2011. doi: 10.1088/0004-637X/727/2/118. (Cited at page 72)

V. Vikram, C. Chang, B. Jain, D. Bacon, A. Amara, M. R. Becker, G. Bernstein, C. Bonnett, S. Bridle, D. Brout, M. Busha, J. Frieman, E. Gaztanaga, W. Hartley, M. Jarvis, T. Kacprzak, A. Kovács, O. Lahav, B. Leistedt, H. Lin, P. Melchior, H. Peiris, E. Rozo, E. Rykoff, C. Sánchez, E. Sheldon, M. A. Troxel, R. Wechsler, J. Zuntz, T. Abbott, F. B. Abdalla, R. Armstrong, M. Banerji, A. H. Bauer, A. Benoit-Lévy, E. Bertin, D. Brooks, E. Buckley-Geer, D. L. Burke, D. Capozzi, A. Carnero Rosell, M. Carrasco Kind, F. J. Castander, M. Crocce, C. E. Cunha, C. B. D'Andrea, L. N. da Costa, D. L. DePoy, S. Desai, H. T. Diehl, J. P. Dietrich, J. Estrada, A. E. Evrard, A. Fausti Neto, E. Fernandez, B. Flaugher, P. Fosalba, D. Gerdes, D. Gruen, R. A. Gruendl, K. Honscheid, D. James, S. Kent, K. Kuehn, N. Kuropatkin, T. S. Li, M. A. G. Maia, M. Makler, M. March, J. Marshall, P. Martini, K. W. Merritt, C. J.

Miller, R. Miquel, E. Neilsen, R. C. Nichol, B. Nord, R. Ogando, A. A. Plazas, A. K. Romer, A. Roodman, E. Sanchez, V. Scarpine, I. Sevilla, R. C. Smith, M. Soares-Santos, F. Sobreira, E. Suchyta, M. E. C. Swanson, G. Tarle, J. Thaler, D. Thomas, A. R. Walker, and J. Weller. Wide-field lensing mass maps from Dark Energy Survey science verification data: Methodology and detailed analysis. *Physical Review D*, 92(2):022006, July 2015. doi: 10.1103/PhysRevD.92.022006. (Cited at pages 61, 71, 83 e 90)

V. Vikram et al. Wide-field lensing mass maps from Dark Energy Survey science verification data: Methodology and detailed analysis. *Phys. Rev.*, D92(2):022006, 2015. doi: 10.1103/PhysRevD.92.022006. (Cited at pages 91, 108, 110, 121, 132 e 141)

C. G. R. Wallis, J. D. McEwen, T. D. Kitching, B. Leistedt, and A. Plouviez. Mapping dark matter on the celestial sphere with weak gravitational lensing. *ArXiv e-prints*, March 2017. (Cited at pages 54, 72, 73, 75, 76 e 81)

Christopher G. R. Wallis, Jason D. McEwen, Thomas D. Kitching, Boris Leistedt, and Antoine Plouviez. Mapping dark matter on the celestial sphere with weak gravitational lensing. 2017. (Cited at pages 110, 121, 134 e 141)

B. D. Wandelt, E. Hivon, and K. M. Gorski. Topological Analysis of High-Resolution CMB Maps. *ArXiv Astrophysics e-prints*, March 1998. (Cited at page 64)

Y. Wiaux, J. D. McEwen, P. Vandergheynst, and O. Blanc. Exact reconstruction with directional wavelets on the sphere. *Mon. Not. Roy. Astron. Soc.*, 388:770, 2008. doi: 10.1111/j.1365-2966.2008.13448.x. (Cited at page 67)

J. Zuntz, M. Paterno, E. Jennings, D. Rudd, A. Manzotti, S. Dodelson, S. Bridle, S. Sehrish, and J. Kowalkowski. CosmoSIS: Modular cosmological parameter estimation. *Astronomy and Computing*, 12:45–59, September 2015. doi: 10.1016/j.ascom.2015.05.005. (Cited at pages 74, 89, 119 e 121)

J. Zuntz, E. Sheldon, S. Samuroff, M. A. Troxel, M. Jarvis, N. MacCrann, D. Gruen, J. Prat, C. Sánchez, A. Choi, S. L. Bridle, G. M. Bernstein, S. Dodelson, A. Drlica-Wagner, Y. Fang, R. A. Gruendl, B. Hoyle, E. M. Huff, B. Jain, D. Kirk, T. Kacprzak, C. Krawiec, A. A. Plazas, R. P. Rollins, E. S. Rykoff, I. Sevilla-Noarbe, B. Soergel,

T. N. Varga, T. M. C. Abbott, F. B. Abdalla, S. Allam, J. Annis, K. Bechtol, A. Benoit-Lévy, E. Bertin, E. Buckley-Geer, D. L. Burke, A. Carnero Rosell, M. Carrasco Kind, J. Carretero, F. J. Castander, M. Crocce, C. E. Cunha, C. B. D'Andrea, L. N. da Costa, C. Davis, S. Desai, H. T. Diehl, J. P. Dietrich, P. Doel, T. F. Eifler, J. Estrada, A. E. Evrard, A. F. Neto, E. Fernandez, B. Flaugher, P. Fosalba, J. Frieman, J. García-Bellido, E. Gaztanaga, D. W. Gerdes, T. Giannantonio, J. Gschwend, G. Gutierrez, W. G. Hartley, K. Honscheid, D. J. James, T. Jeltema, M. W. G. Johnson, M. D. Johnson, K. Kuehn, S. Kuhlmann, N. Kuropatkin, O. Lahav, T. S. Li, M. Lima, M. A. G. Maia, M. March, P. Martini, P. Melchior, F. Menanteau, C. J. Miller, R. Miquel, J. J. Mohr, E. Neilsen, R. C. Nichol, R. L. C. Ogando, N. Roe, A. K. Romer, A. Roodman, E. Sanchez, V. Scarpine, R. Schindler, M. Schubnell, M. Smith, R. C. Smith, M. Soares-Santos, F. Sobreira, E. Suchyta, M. E. C. Swanson, G. Tarle, D. Thomas, D. L. Tucker, V. Vikram, A. R. Walker, R. H. Wechsler, and Y. Zhang. Dark Energy Survey Year 1 results: weak lensing shape catalogues. *Monthly Notices of the Royal Astronomical Society*, 481:1149–1182, November 2018. doi: 10.1093/mnras/sty2219. (Cited at page 136)

F. Zwicky. Die Rotverschiebung von extragalaktischen Nebeln. *Helvetica Physica Acta*, 6:110–127, 1933. (Cited at page 24)